Development of Early Warning System for Volcanic Sector Collapse Tsunamis

(火山性山体崩壊による津波に対する即時警報システムの開発)

Doctoral Dissertation

Rinda Nita Ratnasari

Department of Natural History Science, Graduate School of Science,

Hokkaido University

March 2024

Abstract

Present tsunami warning systems have been focused on earthquake-generated tsunamis, but rapidly evaluating the tsunamis caused by volcanic eruptions and/or volcanic sector collapses remains a challenge. Various models are available to simulate landslides and tsunami generation from volcanic sector collapse. However, implementing such models for real-time forecasting is still challenging due to diverse and complex mechanisms in tsunami generation that make it difficult to immediately estimate the source model for the real-time forecasting simulation. The occurrence of volcanic sector collapse tsunamis is less frequent than that of earthquake-generated tsunamis, but potential catastrophe from volcanic tsunamis including sector collapse cannot be underestimated and should be considered as an important tsunami source in terms of hazards and disaster strategies.

A study focusing on the development of early warning system for the sector collapse case of Anak Krakatau volcano in Indonesia was presented in this study. The present study applied a numerical model to the 2018 Sunda Strait tsunami event, which was generated by the sector collapse of Anak Krakatau, investigated a tsunami prediction skill by the model, and developed a real-time forecasting method based on a pre-computed database for future tsunamis accompanied by such eruption of Anak Krakatau. The database stores spatiotemporal changes in water surface level and flux, which are simulated under various collapse scenarios, for confined areas in the vicinity of potential source. The areas also cover the locations of six observation stations that are virtually placed on uninhabited islands surrounding the source area. For real-time tsunami forecasting, the most suitable scenarios to reproduce the observed waveforms are searched quickly in the database

through waveform fitting procedures at observation stations. The pre-computed water surface level and flux distribution under the identified scenarios are further provided as input for rapid tsunami propagation simulation. Therefore, effective real-time forecasting can be conducted to densely populated coastal areas located at a considerable distance from the source, such as the coasts of Java and Sumatra. The forecasting performance was examined by applying the method for three hypothetical collapse scenarios assuming different volumes and sliding directions. The numerical experiments using hypothetical collapse scenario in this study indicated that the tsunamis along the coast of Java and Sumatra were successfully forecasted by applying our method. This study shows that the combination of a pre-computed database and the utilization of observation stations near the source area was able to produce appropriate tsunami forecasting for the coastal area of Java and Sumatra even in a volcanic tsunami event. Moreover, implementing our method allows us to estimate real-time tsunamis generated by volcanic activity of Anak Krakatau without considering the information on source mechanisms.

Further study towards the development of tsunami warning was conducted by simulating the sector collapse cases of Komagatake volcano located in Hokkaido, Japan. Preliminary modeling of landslide and tsunami from the 1640 Komagatake tsunami was first performed using a similar manner to the 2018 Sunda Strait event. Three different collapse volumes were employed in the numerical simulation. The initial collapse volume of 1.8-2.4 km^3 explained both tsunami deposit and tsunami height measurements, suggesting the volume estimation range is appropriate to simulate the 1640 Komagatake tsunami event. Further analysis on the tsunami characteristic was conducted by assuming three hypothetical scenarios. All three collapse scenarios using different volumes and directions resulted in similar tsunami height distribution patterns. The findings in this

study show that tsunami height distribution can be predicted by analyzing approximately 5 to 10 minutes waveforms observed at virtual observation stations. The variations in tsunami height can be identified by looking at amplitude differences from the observed waveforms at virtual stations. Rapid detection of tsunamis at the observation stations allows us to have warning time targeted the coastal area of Hokkaido.

The topic in this study mainly covers a study related to the development of tsunami warning system associated with volcanic sector collapses. Both studies on the volcanic sector collapse of Anak Krakatau and Komagatake volcanoes shows that the existence of observation stations in the vicinity of the volcano is essential towards the implementation of tsunami early warning. Considering the findings, this study concludes that a well-constructed tsunami forecasting method combined with the utilization of observation should be feasible for future tsunami warning systems even for volcanic tsunami cases.

Keywords: *Volcanic tsunamis, Anak Krakatau, Komagatake, Tsunami Warning System*

Table of Contents

General Introduction

Tsunamis associated with volcanic sector collapse are widely recognized worldwide. Although their occurrence is less-frequent than that of earthquake-generated tsunamis, the potential catastrophe the collapse of volcanic island cannot be underestimated and should be considered an important tsunami source in terms of hazards and disaster strategies (Yamanaka and Tanioka, 2017; Williams et al, 2019). Most of volcanic islands have complex morphology with weak substrata and unstable material due to rapid accumulation of edifice during eruption (Walter et al. 2019). Tsunamis generated by the collapse sector of volcano are frequently found in the area with the high density of volcanoes that located close to the sea (Paris, 2015). Historical volcanic tsunamis events such as the 1640 Komagatake and the 1741 Oshima-oshima tsunamis in Japan, also the 1856 Awu and the 1883 Krakatau tsunamis in Indonesia, show that those atypical tsunami sources from the volcano cannot be underestimated.

In 2018, a devastating tsunami occurred in Sunda Strait, Indonesia, which caused 437 casualties in the vicinity of Sunda Strait along the coast of Java and Sumatra. The 2018 Sunda Strait tsunami was generated by the sector collapse of Anak Krakatau volcano. The volcanic complex of Anak Krakatau has been known as the site of the 1883 Krakatau eruption, which is considered as one of the most destructive tsunami events in history (Deplus et al. 1995). Prior to the 2018 collapse, the Anak Krakatau had been in an intense eruption phase since June 2018. At that time Anak Krakatau had a top elevation about ~250 m above sea level before the sector collapse event. The tsunami hazard from flank collapse of Anak Krakatau volcano was highlighted by the study of Giachetti et al. (2012) years before the occurrence of the 2018 event. They identified that the southwestern area

of volcano was prone to failure due to partial destabilization and would bring potential danger for coastal area of Sunda Strait. Considering the highly populated area in the area of Sunda Strait, a monitoring combined with efficient tsunami warning system should be prepared for Anak Krakatau.

Tsunami generated by volcanic debris avalanches were widely recognized as a natural hazard. Several major events of tsunamis related to volcanic sector collapse have occurred in Japan. The collapse of Komagatake volcano in 1640, Oshima-Oshima volcano in 1761, the Unzen Mayuyama volcano in 1792, and the Sakurajima volcano in 1781 were recognized as historical tsunamis related to volcanic sector collapse (Siebert L, 1984; Furukawa et al. 2008). The 1640 Komagatake tsunami was one of the most notable events which caused approximately 700 casualties. The collapse of the mountaintop of Komagatake entered the sea and generated a tsunami along Uchiura Bay and further southern coast of Hokkaido. Komagatake volcano has many eruption records since 1640 such as those in 1856 and 1929 that were characterized by pyroclastic flow. In the present time, the mountain area of Komagatake in Hokkaido is known as a famous sightseeing spot. The development of the mountain foot area should take natural hazard such as pyroclastic and debris avalanche due to the collapse of mountaintop. Here, we present a study on tsunami generation by sector collapse of Komagatake volcano for future tsunami warning purposes. Numerical simulation considering various collapse scenarios of Komagatake were conducted to identify the characteristic of tsunami resulting from the sector collapse of Komagatake volcano.

The existing tsunami warning systems mainly focus on earthquake-generated tsunamis and rely on the observation systems to accurately detect tsunami potential from earthquakes (Tsushima et al. 2014; Maeda et al. 2015; Tanioka et al. 2020). Various types

of tsunami monitoring systems have been actively operated for early tsunami warning from small to gigantic tsunami scales. Present tsunami warning systems available worldwide are mainly focused on the earthquake-generated tsunamis and other tsunami sources especially from volcanic-tsunamis is not included in the system. In the case of volcanic tsunamis, mitigating tsunamis remains challenging because it requires deeper understanding of source mechanism of wave generation and monitoring techniques to be combined. In specific cases such as volcanic sector collapses, estimating the source mechanisms in real-time is challenging because of the diversity of waves generated by mass failure. The initiation volume of the sector collapses is also complex by broad variety of generation mechanisms, from small slides to large avalanches. Uncertainties in the exact source mechanism of the volcanic sector collapse leave major challenges to construct real-time tsunami forecasting (Grilli et al. 2019; Muhari et al. 2019).

Focusing on the development of tsunami early warning, here we conducted a study mainly to explore the forecasting method and improve the existing tsunami warning system to accommodate non-seismic tsunami sources including volcanic tsunamis. The content of this study is divided into five chapters. The first chapter mainly provides a review of the development of tsunami early warning systems for earthquakes and landslides. The second chapter gives a review related to the tsunami generation by volcanic sector collapse. The third chapter talks about the landslide and tsunami models applied in this study. In the fourth chapter, a tsunami warning system is proposed for the sector collapse case of Anak Krakatau volcano, and we discussed its effectiveness. In the last chapter, numerical simulation of landslides and tsunami from the debris avalanche of Komagatake volcano are performed to identify tsunami characteristics for future tsunami warning systems.

Chapter 1

Review on the Development of Tsunami Early Warning System

1.1 Earthquake-generated Tsunamis

The 2011 Tohoku-oki tsunami and 2004 Indian Ocean tsunami were denoted as examples of large tsunamis that severely damaged wide coastal communities (Mori and Takahashi, 2012; Fritz et al. 2006). Over the years after, early tsunami warning systems have been operated in many areas for anticipating future large tsunamis by improving the forecasting capabilities, establishing mitigation strategy, and educating the wider community (Kanoglu and Synolakis, 2015). Development of tsunami warning system is primarily to detect and alert coastal communities about potential tsunamis in advance. A comprehensive tsunami warning system becomes evident, particularly in the context of earthquake-generated tsunamis as response to the continuous seismic events that potentially bring tsunami threat. In tsunami early warning, rapidly and accurately forecasting the tsunami impact (i.e. tsunami inundation) is important for reducing the damage and casualties (Makinoshima et al. 2021). A significant challenge in addressing earthquake-generated tsunamis lies in the rapid and accurate prediction of the potential impact of tsunamis, as the complex seismic activity and subsequent wave generation poses a formidable obstacle for precise warning systems. Earthquake magnitude alone does not always characterize the size of impact because complex earthquake mechanism, coastal morphological features, etc., influence the tsunami behavior (Mori et al. 2022). Earthquakes vary in magnitude, depth, location, making it challenging to predict the exact characteristics of the resulting tsunamis (Hanka et al. 2010). The unique characteristics

of each earthquake contribute to the challenge of accurately forecasting the resulting tsunami.

The evolution of tsunami early warning systems cannot be separated from the improvement of tsunami monitoring systems over time. In present, advanced monitoring systems play a crucial role in rapidly detecting and assessing earthquake-generated tsunamis, enabling warning time and alerts for coastal areas (Aoi et al. 2021). Observation technology such as DART buoy as well as ocean bottom sensors are widely recognized as an effective monitoring system for the detection and tsunami measurements in the open ocean (Rabinovich et al. 2017). Reliable information for tsunami forecasting can be obtained by direct measurement through observation networks especially from offshore tsunami observation networks. The networks can monitor sea level changes, providing valuable data for forecasting. Moreover, offshore observation networks provide opportunities for tsunami measurement before inundated the coastal area (Tsushima and Ohta, 2014). Notable underwater cabled observatory systems are currently in operation throughout the world such as S-net (Seafloor Observation Network for Earthquakes and Tsunamis) in Japan and NEPTUNE (North-East Pacific Time-series Undersea Networked Experiments) in Canada. Continuous monitoring data should be beneficial, not only for operational of real-time tsunami forecasting but also for further tsunami research.

Tsunami forecasting methods have been proposed by utilizing the tsunami observation network (Tsushima et al. 2012; Maeda et al. 2015; Yamamoto et al. 2016; Takahashi et al. 2017). Wider exploration on the utilization of observation stations combined with designated methods provides more variation of tsunami forecasting methods such as forecasting based on the utilization of GNSS networks, radar data, machine learning, etc. (Mulia et al. 2020; Makinoshima et al. 2021; Hossen et al. 2021;

Mulia et al. 2022). Tsunami forecasting and modeling have progressed through the years which makes early warning systems for earthquake-generated tsunamis available now. Many tsunami warning system utilize the information received at observation stations and use it for further analysis of tsunami impact during real-time forecasting. A method based on the pre-computed tsunami database is widely used for tsunami early warning purposes (Gusman et al. 2014; Jimenez et al. 2018). A different method called tsunami data assimilation is also known as one of the promising forecasting methods. This method is worked by continuously assimilating the dense tsunami data received at observation networks into numerical simulation without considering the seismic source parameters (Maeda et al. 2015). Another method of tFISH/RAPiD was initiated to forecast the tsunami along the near-field coast by incorporated the initial sea surface elevation distribution by GNSS data into inversion of tsunami waveforms (Tsushima et al. 2014).

1.2 Landslide-generated Tsunamis

Tsunamis generated by landslides or other non-tectonic sources present potential hazards for coastal areas, demanding proactive measures for the safety of coastal communities. Constructing an effective tsunami warning system for landslide tsunamis is important for disaster mitigation. However, it comes with several challenges owing to the unique characteristics of each event. Landslides are varied in size, scale, and characteristics. Some events may be relatively small and localized, while others can be massive and have an extensive range of impact. Complicated dynamics involved in the landslide generation and its deformation make landslide-generated tsunamis remain one of the least studied (Watts and Borrero, 2009). In terms of tsunami warning, the application and exploration of real-time forecasting methods mainly concentrates on earthquake-generated tsunamis. Several reasons underlying the difficulties in

constructing tsunami early warning for landslide cases. One of the possible reasons is the lack of a well-established method for accurately estimating the landslide dynamics. Furthermore, the uncertainty of failure planes and complex behavior after the collapse contribute to the difficulties in the development of tsunami warning (Lovholt et al. 2020). The source mechanism of landslides is still difficult to estimate immediately after the occurrence of landslides due to its complexity.

Contribution of landslides to tsunami wave generation has been widely recognized and tsunami modeling has expanded to simulate wave generation and propagation from landslide source (Lovholt et al. 2015; Reid and Mooney, 2023). Several landslide models are available to model tsunami from both subaerial and submarine landslide including volcanic failure cases i.e. AVALANCHE code (Heinrich and Piatanesi, 2000), Non-Hydrostatic WAVE (NHWAVE) (Ma et al. 2012), Tsunami Squares (Xiao et al. 2015), VolcFlow (Kelfoun et al. 2010), etc. Those models have been used to study the landslide-generated tsunamis resulting from different collapse event cases around the world (Paris et. al 2021; Kirby et al. 2016; Yamanaka and Tanioka, 2017; Giachetti et al. 2012). Numerical modeling is available to simulate landslide-generated tsunamis, but employing those models for tsunami warning purposes is still challenging. It is mainly due to the difficulties in obtaining the initial landslide source as input for numerical modeling to forecast the tsunami impact in actual time. The uncertainty in the generation mechanism contributing to the difficulties for building tsunami warning and forecasting for landslide-generated tsunamis.

In 2002, a sector collapse of Sciara del Fuoco on the volcanic island of Stromboli, Italy, generated tsunami with maximum run-up of 10.9 m (Calabro et al. 2020). Since then, a monitoring system has been available to monitor the flank collapse of Stromboli

volcano in response to the potential tsunami. Two elastic beacon tsunami gauge system was deployed about 300 m offshore to the Northeast and Southwest of the Sciara del Fuoco. Each beacon was equipped with pressure sensors installed at 14 m and 46 m below the sea surface. Utilizing two elastic beacon placed offshore, a tsunami warning system is actively operated now at Stromboli island. The tsunami early warning method is mainly based on the ratio of short-term average (STA) and long-term average amplitude (LTA). Considering both calm and stormy conditions, the threshold ratio of STA/LTS was fixed at 20. Immediate tsunami warning will be issued when the ratio of STA/LTA threshold is larger than detected threshold (STA/LTA>20) for at least 90s at both observation stations. This system has detected three tsunamis since the deployment and has been actively monitoring Stromboli until now (UNESCO/IOC, 2024). In Indonesia, a sea level monitoring system called IDSL (Inexpensive Device for Sea Level Monitoring) was installed in 2019 after the devastating tsunamis of Anak Krakatau and Palu earthquake in 2018 to accommodate non-seismic tsunamis (Husrin et al. 2022). Currently, several stations are placed around the coast of Java and Sumatra including a station placed in the vicinity of Anak Krakatau for anticipating tsunami from the sector collapse of volcano. More observation stations including tiltmeter, seismic stations, and surveillance camera will be added to the network to anticipate the tsunami from sector collapse of Anak Krakatau.

Tsunami observation networks are known as a reliable tool to detect tsunami and many tsunami warning systems rely on the observation networks to forecast tsunamis including landslide-generated tsunamis. In present, the utilization of observation networks is still not optimal for tsunami early warning caused by landslides. It is mainly due to the lack of designated methods that make optimal use of observation networks for

tsunami forecasting. In present, very small numbers of tsunami warning system is available in operational for landslide tsunamis. Further exploration of the forecasting methods by utilizing the existing observation networks is needed to find the most effective forecasting methods for landslide-generated tsunamis and other non-tectonic tsunami sources.

Chapter 2

Review on the Volcanic Sector Collapse Tsunamis

The source of volcanic tsunamis is divided into several mechanisms such as volcano-tectonic earthquakes, flank collapse, pyroclastic flow, underwater explosion, shock wave, and caldera collapse (Paris, 2015). Among these mechanisms, volcanic flank collapse represents a low-frequency occurrence but poses high magnitude hazard (Paris et al. 2011). Apart from volcanoes, mass failure can occur in various areas such as fjords, rivers, lakes, reservoirs, and in the deep water (Paris et al. 2021). Here, we limit our focus study to the tsunami caused by sector collapse or flank collapse of volcano that is considered as major threats from the volcanic islands (Walter et al. 2019).

In general, volcanic sector collapse tsunamis are generated from the displacement of the water when the landslide enters the water bodies. Then, the generated waves travel to the distant shorelines when entering the open waters and bring potential damage to the coastal area. Flank collapse produced by volcanoes has a broad range of scales, from rockfalls to sector collapse with volumes of cubic meters to tens of cubic kilometers (Day S, 2015; Robbe-Saule, 2021). The mechanism of volcanic tsunamis is still not fully understood due to several factors such as lack of direct observation and complexity of the source characteristic (Day, 2015). A better understanding of the physical process of volcanic tsunamis may be obtained by numerical modeling (Paris et al. 2020). Moreover, laboratory experiments can help to understand landslide motion from the initial collapse until entered the water column.

Tsunamis caused by sector collapse of volcanoes occurred worldwide which have potential to cause major natural hazard for coastal population and infrastructure. Several

cases were categorized as historical flank failures, for example, the rockslide avalanche in Mount St. Helens that associated with earthquake (Voight et al. 1981), the collapse sector of Ritter Island which had run-up heights of more than 20 m (Ward and Day, 2003), the debris avalanche associated with intense eruption of the 1640 Komagatake volcano that caused about 700 casualties (Furukawa et al. 2008), and the recent unwarned tsunami of Anak Krakatau volcano in 2018 which caused large damage in Sunda Strait, Indonesia (Muhari et al. 2019). Many volcanic sector collapse cases are related to the slope instabilities caused by volcanic eruptions. However, the mass failure not always associated with eruptions as the structure of the volcano are originally unstable by its nature (Paris, 2015). Several factors such as structural origin, magmatic intrusion, edifice accumulation, hydrothermal processes, and climatic factor include rain have contributed to the source of instability and mass failure of volcanoes (Keating and McGuire, 2000; Paris, 2015; Gallotti et al. 2020). Volcanic instability was defined as the condition within which volcanic edifice has been destabilized to a degree sufficient to increase the likelihood of structural failure of all or part of edifice (McGuire, 1996). In general, the most important factors affecting the sector collapse tsunamis are volume, thickness, and velocity. In post collapse event, the initial collapse volume can be defined by collapse scar or deposit. The initial volume may contain important information about the initial amplitude of the impulse wave generated from landslide (Robbe-Saule et al. 2021). Then, the landslide most effectively generates tsunami when the thickness is comparable to the water depth. The velocity affects the energy transfer to the open water with faster velocity obviously have larger transfer energy (Day S, 2015).

The tsunamis generated by volcanic failure are different depending on their volume, origin (submarine or subaerial), and dynamics (Paris, 2015). Generated water by volcanic

collapse is generally characterized by an impulse wave which resulted from the entrance of mass to the water (Fritz et al. 2004; Paris, 2015). When the edifice of collapse enters the open ocean, then the displaced water mass rushes outward as a tsunami (Furukawa et al. 2008). Compared to the earthquake generated tsunamis, the tsunami wave from the sector collapse is characterized with shorter wavelength and stronger wave dispersion. Such kind of mechanism often resulted in the large wave amplitude locally and high run-up in the further coast (Ma et al. 2015; Gallotti et al. 2020). The tsunami genesis by a collapse is mainly controlled by the types of collapse (rockfalls, debris flow, lahars, etc). Moreover, the landslide volume and landslide dynamics (velocity, acceleration, etc.) also have an important role to the wave generations (Lovholt et al. 2020).

Chapter 3

Landslide and Tsunami Models in this Study

The study of sector collapse tsunamis is generally based on numerical models or physical experiments due to scarcity of the events records (Paris et al. 2021). Many studies have been conducted to gain a deeper understanding of tsunami generation mechanisms from volcanic sector collapse by both numerical simulations and laboratory experiments. Several numerical models are available to simulate the tsunami generation and propagation of sector collapse tsunamis. A model based on the depth-averaged approach was used by Kelfoun et al. (2010) to simulate the tsunamis generated by two potential landslides at Reunion Island using a modified VolcFlow model (Kelfoun and Druitt, 2005). Another model named NHWAVE was frequently used to estimate the surface displacement and velocity resulting from either submarine or subaerial landslide based on the three-dimensional non hydrostatic code (Ma et al. 2012; Kirby et al. 2016; Grilli et al. 2019). Then, a different model of AVALANCHE code was able to simulate both landslide and tsunami from the sector collapse considering one-phase grain-flow model (Savage and Hutter, 1989) and coulomb basal friction by solving the equations of conservation of mass and momentum (Heinrich et al. 2001b; Paris et al. 2019). Numerous laboratory experiments were also carried out to obtain a better knowledge on the source process and wave generation by landslides. Fritz et al. (2003) conducted a laboratory experimental using a case of Lituya Bay tsunami. Their experiment was based on the rockslide scenarios that impacted the assumed physical model of topography and bathymetry in Lituya Bay. Another laboratory experiment using a large wave tank was presented by Di Risio et al. (2009) to identify the landslide and tsunami generated from a

conical island shape. A small scale of laboratory experiment initiated by Robbe-Saule et al. (2021) was conducted by using different sets of landslide parameters and identified the influence of each parameter such as grain size, water depth, etc. Those models and laboratory experiments were just a few examples of many other models available for landslide tsunamis. Diverse studies allow us to gain better understanding of the involved process in the landslide tsunamis by numerical models and/or laboratory experiments. In the context of natural hazard and disaster mitigation, it is expected that the deeper knowledge of the source process of sector collapse tsunamis will lead to more relevant mitigation strategies. The real-time tsunami forecasting approach in this study was entirely based on numerical simulations without any physical laboratory experiments.

In the simulation of generation and propagation of tsunami associated with volcanic sector collapse, this study mainly uses two models of VolcFlow and Boussineq models. Volcflow numerical code is a model capable of simulating various kinds of mass flow such as pyroclastic flows and debris avalanche related to tsunamis (Ulvrova et al. 2016). VolcFlow model is a two-dimensional (2D) depth-average model that is capable to simulate landslide and water including volcanic sector collapse case (Kelfoun and Druit, 2005; Kelfoun et al. 2010; Giachetti et al. 2011). The model is capable of simulating the tsunami generation by two fluids (landslide and water), which interact at each time step by solving general non-linear shallow water equations of mass conservation and momentum balance (Kelfoun et al. 2010). Another complex second-order 3D effect and dissipation due to the wave breaking were not considered in VolcFlow model. The simulation neglected the mixing between the landslide and water. The landslide is simulated by the following set of equations of momentum balance (1-2) and mass conservation (3):

$$\frac{\partial}{\partial t}(h_a u_x) + \frac{\partial}{\partial x}(h_a u_x^2) + \frac{\partial}{\partial y}(h_a u_x u_y) = g h_a \sin\alpha_x - \frac{1}{2} k_{act/pass} \frac{\partial}{\partial x} \cdot (g h_a \cos\alpha) + \frac{T_x}{\rho}, \quad (1)$$

$$\frac{\partial}{\partial t}(h_a u_y) + \frac{\partial}{\partial y}(h_a u_y^2) + \frac{\partial}{\partial y}(h_a u_y u_x) = g h_a \sin\alpha_y - \frac{1}{2} k_{act/pass} \frac{\partial}{\partial y} \cdot (g h_a \cos\alpha) + \frac{T_y}{\rho}, \quad (2)$$

$$\frac{\partial h_a}{dt} + \frac{\partial}{\partial x}(h_a u_x) + \frac{\partial}{\partial y}(h_a u_y) = 0 \quad (3)$$

where the h_a is the landslide thickness, ρ is the relative density, u = (u_x,u_y) is the landslide velocity, $k_{act/pass}$ is the earth pressure coefficient (dimensionless), T is the total retarding stress, g is the gravity, and α is the ground slope angles. Then, the water is simulated using set of equations (4-6) which is similar to those of landslide:

$$\frac{\partial}{\partial t}(h_w v_x) + \frac{\partial}{\partial x}(h_w v_x^2) + \frac{\partial}{\partial y}(h_w v_x v_y) = g h_w \sin\beta_x - \frac{1}{2}\frac{\partial}{\partial x}(g h_w^2 \cos\beta) + \frac{R_x}{\rho_w} - 3\frac{\mu_w}{\rho_w h_w} v_x \quad (4)$$

$$\frac{\partial}{\partial t}(h_w v_y) + \frac{\partial}{\partial x}(h_w v_y^2) + \frac{\partial}{\partial y}(h_w v_y v_x) = g h_w \sin\beta_x - \frac{1}{2}\frac{\partial}{\partial y}(g h_w^2 \cos\beta) + \frac{R_y}{\rho_w} - 3\frac{\mu_w}{\rho_w h_w} v_y \quad (5)$$

$$\frac{\partial h_w}{dt} + \frac{\partial}{\partial x}(h_w v_x) + \frac{\partial}{\partial y}(h_w v_y) = 0 \quad (6)$$

The variable h_w is the water depth, β is the slope of ocean bottom, v = (v_x,v_y) is the water velocity, g is the gravity, μ_w is the water viscosity, R is stress exerted by landslide on the water, and ρ_w is the water density. More detail about governing equations can be found in Kelfoun et al. (2010). The two sets of equations (1-3) and (4-6) are calculated at same

time step. Numerical simulation by VolcFlow model was performed assuming a water density of 1000 kg m^{-3}. For landslides, we applied a density of 1500 kg m^{-3} referring to the main volcanic material composition (Sudrajat, 1982; Camus et al. 1987; Giachetti et al. 2012). Simulations of the landslide and tsunami generation by the volcanic sector collapse in this study are mainly conducted using VolcFlow model.

Tsunamis generated by most landslides tend to display dispersive behavior at least in some directions (Glimsdal et al. 2013). The variation of landslide thickness in the generation mechanism of tsunamis may contribute to dispersion (Ward, 2001; Glimsdal et al. 2013; Grilli et al. 2017). The short-wave components resulting from rapid acceleration or deceleration from landslide affect the tsunami propagation by its frequency dispersion (Harbitz et al. 2006; Paris, 2015; Grilli et al. 2019). The characteristics of the landslide itself influence the dispersion to the generated waves by its acceleration and velocity (Salmanidou et al. 2017). In the case of a tsunami associated with volcanic sector collapse, a model that include the dispersion effect has been widely applied and suggested to simulate a tsunami that was caused by mass failure (Tappin et al. 2014; Grilli et al. 2017; Paris et al. 2019). Several previous studies employed a model considering dispersive effect to simulate the propagation of tsunami from the 2018 Anak Krakatau event (Grilli et al. 2019; Mulia et al. 2020; Paris et al. 2020). The VolcFlow model is capable of simulating both the behavior of collapsed materials and the propagation of tsunamis, but the speed of tsunami propagation is limited to that of the long waves. The study conducted by Paris et al. (2020) highlighted the dispersive effects in the generated tsunami waves from the numerical simulation of the 2018 Sunda Strait tsunami. Comparing the numerical simulations using shallow water and Boussinesq model, also estimating the dispersion effect by calculating the dispersion parameters of

Glimsdal et al. (2013), their result indicates that dispersive effects in the Sunda Strait appear to be significant mainly for the first waves. To account for dispersive characteristics of tsunami, this study employs a non-linear dispersive theory (Boussinesq model) (Yamanaka and Tanioka, 2017) to simulate the tsunami propagation from the tsunami wave field first estimated by VolcFlow model. The manning roughness coefficient of 0.025 $m^{-1/3}$ was assumed for the bottom friction terms in the Boussinesq model. The details of Boussinesq model used in this study are fully described in Yamanaka and Tanioka (2017). A couple of VolcFlow and Boussinesq models are mainly used to simulate the landslide and tsunami propagation from the volcanic sector collapse cases in this study.

Chapter 4

Development of Early Warning System for Tsunamis Accompanied by Collapse Sector of Anak Krakatau Volcano, Indonesia

4.1 Preliminary Modeling of the 2018 Sunda Strait Tsunami

4.1.1 Anak Krakatau Volcano

Anak Krakatau (*'Child of Krakatau in Indonesian'*) is a relatively young active volcano located in the middle of Sunda Strait between main islands of Java and Sumatra, Indonesia (Fig. 4.1). The volcanic island complex of Anak Krakatau is well known as the site of one of the most powerful eruptions of Krakatau volcano in 1883. The Krakatau eruption in 1883 was recognized as one of the most powerful eruptions recorded in history. The eruption occurred on 26th – 28th August 1883 with Plinian eruption type of Krakatau volcano. The massive eruption in 1883 generated a devastating tsunami with run-up height reached about 15 m to 40 m heights (Nomanbhoy and Satake 1995), caused more than 35000 casualties (Simkin and Fiske, 1983; Giachetti et al. 2012). The nearby islands and the vicinity of Sunda Strait were devastated by the 1883 Krakatau eruption.

After the powerful eruption in 1883, the Krakatau island almost completely disappeared leaving only half cone of Rakata and only small rocks remains above sea level (Deplus et al. 1995). A large flat bottom submarine caldera basin with depth of ~200 m and 7 km wide was formed following the Krakatau eruption in 1883, and it completely changed the morphology of Krakatau complex (Paris et al. 2020). The volcanic activity continued after 1883, producing Anak Krakatau volcano which is known as the child of Krakatau. In the present day, this volcanic island complex consists of Anak Krakatau volcano and three uninhabited islands of Sertung, Rakata, and Panjang (Fig. 4.1b). The

water depth around Krakatau complex is relatively shallow with water depth not exceeding 200 m compared to the west part Krakatau complex that has deeper water depth (Paris et al. 2020). The Anak Krakatau volcano was built in the northeast steep edge of Krakatau caldera that is aligned with the feeder vent of the 1883 Krakatau eruption (Williams et al. 2019; Grilli et al. 2019; Paris et al. 2020). After the 1883 eruption, Anak Krakatau was grown from a submarine volcano to a subaerial volcano which first emerged to the surface in 1928 (Deplus et al. 1995). With gradual volcanic activity, the tuff-ring of Anak Krakatau volcano reached a high of ~150 m above mean sea level by 1959 (Walter et al. 2019). Early activity at Anak Krakatau was dominated by phreatomagmatic explosions with first lava flows erupted between 1960 and 1963 as the vent become subaerial (Grilli et al. 2019). Since then, numerous subsequent eruptions have contributed to the growth and expansion of Anak Krakatau. Continuous intense eruption of Anak Krakatau is occurring until present with strombolian to vulcanian style characterized by small explosive eruptions with columns reaching several kilometers in height (Camus et al. 1987; Deplus et al. 1995).

Located at the steep edge wall of the 1883 caldera, the instability of Anak Krakatau has become a concern due to the lack buttressing support of the volcanic edifice (Deplus et al. 1995; Walter et al. 2019; Ye et al. 2020). Flank collapse may become one of the main hazards emerging from Anak Krakatau as the volcano is partly built on the edge of the 1883 caldera wall (Giachetti et al. 2012). In October 1981, a small tsunami of ~2m high was recorded on Rakata Island resulting from the subaerial eruption accompanied with flank collapse of Anak Krakatau (Camus et al. 1987). The potential hazard from the instability edifice of Anak Krakatau has been noted in numerous studies including Camus et al. (1987) and Deplus et al. (1995). Prior to the collapse sector in

2018, Giachetti et al. (2012) has identified the potential danger of the collapse of Anak Krakatau towards southwest area of volcano. In their study, they mentioned that the edifice on the edge of 1883 Krakatau caldera is quite unstable and prone to collapse due to the location of Anak Krakatau that partially build on the steep caldera wall. Accumulation of volcanic material during the eruptive phase will continue from time to time, making Anak Krakatau volcano keep evolving. Recurrence of sector collapse in the future should be considered as one possible hazard resulting from the high volcanic activity of Anak Krakatau. With naturally unstable environment and high volcanic activity of Anak Krakatau, this condition may lead to tsunami hazard related to the sector collapse and possess a threat to the coastal population of Java and Sumatra (Hochfeld et al. 2022).

4.1.2 The 2018 Sunda Strait Tsunami

On December 22, 2018, a devastating tsunami occurred in the Sunda Strait, Indonesia, causing hundreds of death toll and thousands of injured people. The 2018 tsunami case was generated as a result of a large volume of volcanic material from Anak Krakatau volcano that collapsed into the sea (Grilli et al. 2019; Heidarzadeh et al. 2020). At that time, no associate earthquake event was recorded, and the source mechanism could not be determined immediately (Ye et al. 2020). Prior to the collapse, the intense new eruptive phase was initiated at Anak Krakatau in June 2018 and continue for several months until December 22nd, 2018, when the activity evolved into a sector collapse (Walter et al. 2019). The tsunami wave from the flank collapse of Anak Krakatau significantly affected the adjacent coast of Sunda Strait. Immediate post-tsunami field survey was conducted 4 days after the 2018 tsunami by Muhari et al. (2019) along the coast of Sumatra and Java. At the surrounding islands of Anak Krakatau, the impact of tsunami was clearly seen from the outcrop and vegetation damage that observed from the

airborne survey. From the post-survey measurement, a maximum tsunami runup height and inundation distance of 13.5 m and 330 m, respectively, were measured at Tanjung Lesung area located in the western coast of Java (Muhari et al. 2019). The Sunda Strait has been identified as an area prone to volcanic tsunamis due to the intense volcanic activity of Anak Krakatau volcano. In 1883, a devastating tsunami occurred at the same volcanic complex caused by the eruption of Krakatau volcano. The 2018 and 1883 tsunami events made it evident that tsunami sources resulting from volcanic eruption, especially those related to the sector collapse of volcanic islands, were able to cause a significant natural hazard (Hunt et al. 2021). Therefore, it is necessary to develop a real-time tsunami forecasting method for Anak Krakatau and other area prone to volcanic tsunamis in Indonesia. The Sunda Strait area is categorized as a highly populated area where the big cities, ports, and industries are located. This area also considered as a tsunami prone from both tectonic and volcanic sources. Concerning and focusing on the future sector collapse of Anak Krakatau volcano, we aimed to develop a real-time forecasting method designated for Anak Krakatau.

4.1.3 Various Study on the Sector Collapse of Anak Krakatau

The underlying processes of a tsunami associated with mass failure are commonly investigated through physical experiments and/or numerical simulations. Years before the occurrence of the 2018 collapse event, tsunami hazard from the collapse of Anak Krakatau has been highlighted by Giachetti et al. (2012). Their study used a collapse plane located at southwest side of Anak Krakatau considering the steep slope that prone to collapse. Further numerical simulation was conducted to investigate the tsunami impact on the coastal area using a hypothetical 0.28 km^3 volume of flank collapse. Their result emphasized the impact on the local scale around Sunda Strait and suggested that rapid

detection of the collapse by observation system coupled with reliable tsunami early warning system should be available to prevent the event from being deadly (Giachetti et al. 2012). After the 2018 tsunami event, various studies have been conducted on the 2018 Anak Krakatau event to gain deeper insights into the generation of volcanic tsunamis. A study on the collapse and tsunami of Anak Krakatau by Zengaffinen et al (2020) comparing the instantaneous and gradual collapse of the 2018 Anak Krakatau event. Based on the comparison with observed tsunami at two tide gauge stations on Java island, their study showed that sector collapse of Anak Krakatau in 2018 most likely took place as instantaneous collapse rather than a gradual failure. Several studies also performed investigation by using common numerical models adopting 2D depth-averaged coupled models to understand the dynamics of tsunami caused by sector collapse. Based on the satellite images interpretation, the collapse sector of Anak Krakatau reduced the subaerial area of the volcano by 49 % (Grilli et al. 2019). Numerical simulations employing three different collapse volume scenarios of 0.22 km^3, 0.27 km^3, and 0.30 km^3 were tested for simulating the tsunami generation and propagation by coupled of NHWAVE (Ma et al. 2012) and FUNWAVE (Shi et al. 2012) models. Compared with tsunami measurement data, the general estimation on the collapse geometry resulted in an appropriate landslide volume range from 0.22 – 0.30 km^3 (Grilli et al. 2019). In terms of tsunami hazard, there is possibility of future collapse to the southwest of Anak Krakatau as volcano continues to grow (Grilli et al. 2019). Preliminary modeling on the 2018 landslide and tsunami of Anak Krakatau was also performed by Paris et al. (2020) using a couple of AVALANCHE (Heinrich et al. 2001b) and Boussinesq model (Lovholt et al. 2008). The numerical simulation was conducted using 0.15 km^3 collapse volume and tsunami propagation was simulated by using both shallow water model and Boussinesq models. Their analysis

highlighted the dispersive effects that appeared to be significant from the tsunami generated by the collapse of Anak Krakatau. Therefore, the use of Boussinesq models should be relevant for the Anak Krakatau case (Paris et al. 2020). Further study to investigate the appropriate source mechanisms of the 2018 tsunami event considering two mechanisms from the eruption and landslide was conducted by Ren et al. (2020). The generation of tsunami was simulated using a two-layer model (Kawamata et al. 2005) and tsunami propagation model was performed based on non-linear shallow water equations (LeVeque et al. 2011). The partial collapse volume ranges from 0.20-0.30 km^3 was used for the simulation, and their calculated leading tsunami waves matched well with the tide gauge records at Kota Agung, Marina Jambu, and Ciwandan. Similar with previous studies (Grilli et al. 2019; Paris et al. 2020), the recording waves at Panjang station could not explained well by the simulated waveforms from the study of Ren et al. (2020). For anticipating future events, assessment of the potential landslide from the volcano was suggested as an important point for tsunami hazard mitigation (Ren et al. 2020). Another study by Heidarzadeh et al. (2020) combined the physical experiment and numerical modeling to estimate the appropriate source for the 2018 Anak Krakatau case. Both numerical modeling and physical experiments should be useful to understand the underlying process of tsunami associated with volcanic sector collapse for the improvement of future tsunami warning. The potential collapse of Anak Krakatau in the future has been mentioned by many studies that conducted the numerical simulation of landslide in Anak Krakatau. Lack of study and knowledge on the sector collapse of Anak Krakatau may lead to insufficient disaster preparedness. Therefore, studies focusing on tsunami warning and forecasting for Anak Krakatau and Sunda Strait area should be carried out more.

4.1.4 Data and Method

Tsunami waveforms from the 2018 Sunda Strait tsunami event were recorded at four tide gauge stations located in Kota Agung, Panjang, Ciwandan, and Marina Jambu with 1-min temporal resolution (Fig. 4.1). The original recorded tide gauge data are available from the Geospatial Information Agency of Indonesia (http://tides.big.go.id). A polynomial approximation method similar to that used by Mulia et al. (2020) was applied to the data to extract tsunami waveforms from tide gauge records. Then, set of topography and bathymetry data obtained from the same agency as the tide gauge data (https://tanahair.indonesia.go.id/demnas/#/) were used for the numerical simulation. The topography data has spatial resolution of 0.27 arc-sec and bathymetry data has 6 arc-sec resolution. For tsunami numerical simulation of the 2018 event, a single computational domain with a 3 arc-sec resolution was constructed by integrating the Indonesian topography and bathymetry data with spatial resolution of a 0.27 arc-sec and 6 arc-sec and resampled it. We also utilize the measurement data from the two different post-tsunami surveys conducted by Muhari et al. (2019) and Heidarzadeh et al. (2020). How many locations of surveys, time of surveys. Post-tsunami measurement by Muhari et al. (2019) conducted several days after the tsunami. We used measured tsunami run-up height data at 12 locations along the coast of Java from the post-survey of Muhari et al. (2019). Additionally, we utilized the field survey data from Heidarzadeh et al. (2020) that was conducted in the period of 4-11 January 2020, approximately one year after the event. We used the tsunami run-up data with total of 25 locations along the western coast of Java from the tsunami post-survey of Haidarzadeh et al. (2020).

The realiability of the selected models (VolcFlow and Boussinesq models) were assessed by applying them to the 2018 Anak Krakatau tsunami event. The details of

VolcFlow and Boussinesq models were explained in Chapter 3 of this study. The initial collapse for the preliminary modeling of the 2018 tsunami event is situated in the southwestern part of Anak Krakatau, with a total collapse volume of 0.24 km^3. This collapse source was obtained from Mulia et al. (2020), who estimated the potential source volume by comparing ALOS-2 satellite images of Anak Krakatau volcano from before and after the sector collapse. For the numerical simulation, we are assumed the origin time of tsunami at 13:56 UTC or 20:56 local time (Ye et al. 2020; Mulia et. al 2020). In the computation, VolcFlow and Boussinesq models are sequentially applied for estimating the tsunami generation and propagation. Using the same initial conditions as those used by Mulia et al. (2020), we simulated the behavior of collapsed materials as well as the tsunami generation and propagation based on VolcFlow to extract the spatiotemporal distributions of the simulated water surface level and water fluxes during the event. Subsequently, we switched to the Boussinesq model at a certain time (t_0) after the occurrence of collapse to simulate only tsunami propagation, using the spatiotemporal distribution of the water surface level and water fluxes from the VolcFlow simulation as inputs. We tried the variation of switching time (t_0) and assessed the best switching time by looking at the waveform's comparison at tide gauge stations. We set t_0 to 2 min based on a trial-and-error method and used it as the switching time to the Boussinesq model. The simulation of the 2018 Sunda Strait tsunami was performed by using VolcFlow model for 2-min simulation of tsunami generation and propagation then switched to the Boussinesq model to estimate only tsunami propagation for 100-min simulation.

4.1.5 Numerical Simulation of the 2018 Sunda Strait Tsunami

Numerical simulation of landslide and tsunami of the 2018 Anak Krakatau event have been conducted by several studies applying various models. Grilli et al. (2019)

simulated the flank collapse of Anak Krakatau by interpreting the geometrical failure plane from satellite images. Their study applied three different collapse volumes of 0.22 km^3, 0.27 km^3, and 0.30 km^3 by considering two rheology (granular material and dense viscous fluid) were used for simulation. Another study by Paris et al (2020) applied a different collapse volume of 0.15 km^3 which is smaller compared to the collapse volume in the study of Grilli et al. (2019). In the numerical simulation of landslide and tsunami, estimating the exact initial collapse volume is difficult and still challenging. In the case of subaerial volcano such as Anak Krakatau, the geometrical of landslide plane can be more complicated as the volcano partially submerged in the water.

In the present study, the numerical simulation of collapse and tsunami of Anak Krakatau in 2018 was conducted using combination of VolcFlow and Boussinesq models. At the early stage of computation, the simulation of landslide and tsunami in the first 2 min were simulated using VolcFlow model (Fig. 4.2). The initial collapse with 0.24 km^3 volume indicates in Fig. 4.2a is used as a collapse source for the simulation of the 2018 Sunda Strait tsunami. Based on the simulation, the landslide mass is mainly distributed to the south and southwest part of Anak Krakatau then deposited over the caldera floor (Fig. 4.2b). In the first 2 min, the initial collapse debris interacting with water and triggers extreme wave with height of more than 30 m to the south-westward of the landslide scar (Fig. 4.2c). Computation beyond 2 min was handled by Boussinesq model by continuously simulating the tsunami propagation. The snapshots of tsunami propagation simulation performed by Boussinesq model at 10 min, 20 min, 30 min, and 90 min are shown in Fig. 4.3. The result indicates that tsunami waves are attenuated rapidly as they are traveling towards the coasts of Java and Sumatra. Large leading waves are seen propagating in all directions, with significant tsunami waves mainly towards east,

southeast, south, and southwest part of Anak Krakatau (Fig. 4.3a). After 10 min, the initial tsunami height propagated out of the source with tsunami waves exceeding 10 m, then continued propagating further in all directions towards the coastal of Java and Sumatra. Based on the simulation, tsunami reached the west coast of Java in the area of Tanjung Lesung and Marina Jambu within 30-33 minutes after the initial collapse (Fig. 4.3c). Our simulation is consistent with the tide gauge data at Marina Jambu station which recorded the first tsunami arrival of 33 min after the assumed origin time of 13:56 UTC (Fig. 4.4d). In less than 90 min from the initial collapse, tsunami have completely inundated the western coast of Java and southeastern coast of Sumatra.

Assessing the model performance, we compared the observed tsunami waveform at all four tide gauges stations with our simulated waveforms (Fig. 4.4). At Ciwandan, the simulation shows that tsunami arrived at this station at 38 minutes with first wave amplitude of 30 cm and it is consistent with the observed waveform at this station (Fig. 4.4c). Another tide gauge stations in Sumatra recorded the tsunami from the 2018 event at two locations of Kota Agung and Panjang. The result from our simulation shows that the tsunami arrived at the Kota Agung station in about 41 min which is slightly later than the observed waveform (Fig. 4.4a). The first tsunami wave in Kota Agung with 30 cm height is resulted from our simulation. At Panjang station, numerical simulation shows that tsunami waveform underestimates the observed waveform with late arrival compared to the recorded waveform (Fig. 4.4b). In general, the waveforms observed at Kota Agung, Ciwandan, and Marina Jambu have a reasonable fit with the simulated waveforms. However, a noticeable discrepancy between the simulated and observed tsunami waveforms was found at Panjang station (Fig. 4.4b). A similar discrepancy for Panjang station was found in other studies such as those by Grilli et al. (2019), Mulia et al. (2020)

and Paris et al. (2020). The discrepancy in tsunami amplitude and arrival time were possibly influenced by the effect of shallow water and energy dissipation, as complex interactions occurred in a coastal area of the Panjang station. Moreover, limited grid resolution in this simulation might contribute to the discrepancy of the tsunami simulated at Panjang station (Mulia et al. 2020; Zengaffinen et al. 2020).

Further analyses on the performance of the models, we compared the simulation to the measured run-up height along the coast of java from two different field surveys of Muhari et al. (2019) and Heidarzadeh et. al. (2020). First, we compare our simulations with measured run-up height at 12 locations along the western coast of Java from the measurement of Muhari et al. (2019). The comparison between run-up height measurement and computation is shown in Fig. 4.5 and Table 4.1. Tsunami run-up height comparison using Muhari et al. (2019) data mostly indicates an underestimation, with simulated run-up height about half of the observed ones (Fig. 4.5). Then, for further assessment we compare our simulation with tsunami measurements from Haidarzadeh et al. (2020). We compare our simulation with measured tsunami at 25 locations from the survey of Haidarzadeh et al. (2020) (Fig. 4.6 and Table 4.2). The comparison between measured and calculated tsunami height shows a better fit although there are still discrepancies between measured and simulated runup heights (Fig. 4.6). The resolution of the bathymetry and topography data we used in the simulation may be responsible for the discrepancies in the runup height comparison for the 2018 tsunami simulation. The inundation simulation result can be improved by implementing higher resolution of bathymetry and topography data for modeling. Analysis on the maximum surface water elevations computed in Sunda Strait for the 2018 tsunami is shown in Fig. 4.7. The result shows that tsunami waves propagated in all direction with remarkable large tsunami wave

propagating towards Java island. This result is consistent with the post tsunami field survey by Muhari et al. (2019) where a maximum runup height of 13.5 m was measured in the area around Tanjung Lesung located in the southeast part of Sunda Strait.

Examining the general performance, we consider that the observed tsunami from waveforms recorded at tide gauge stations and post-survey measurement of the 2018 Sunda Strait tsunami event were reasonably explained by our numerical simulation. Thus, the selected models were appropriate for simulating the generation and propagation of tsunamis triggered by the sector collapse of Anak Krakatau. After assessing the reliability of the models through preliminary modeling, we used the combination of the selected models (VolcFlow and Boussinesq models) to construct the pre-computed database of sector collapse for Anak Krakatau volcano as a part of our forecasting strategy.

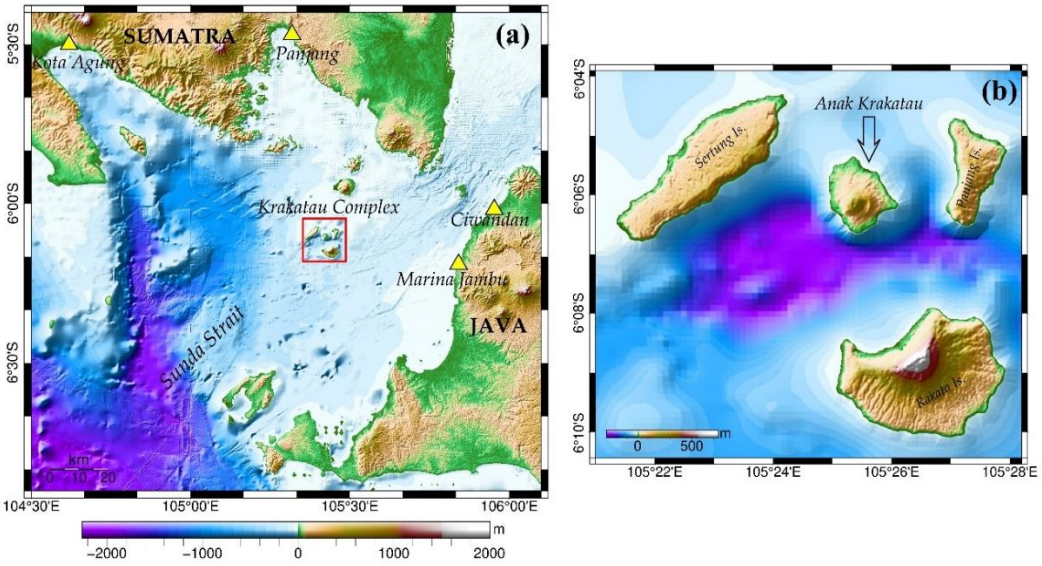

Figure 4.1 (a) Sunda Strait area with four tide gauges located at Kota Agung, Panjang, Ciwandan, and Marina Jambu recorded the 2018 tsunami are indicated by yellow triangles. **(b)** Anak Krakatau volcanic complex is indicated by the red rectangle in (a).

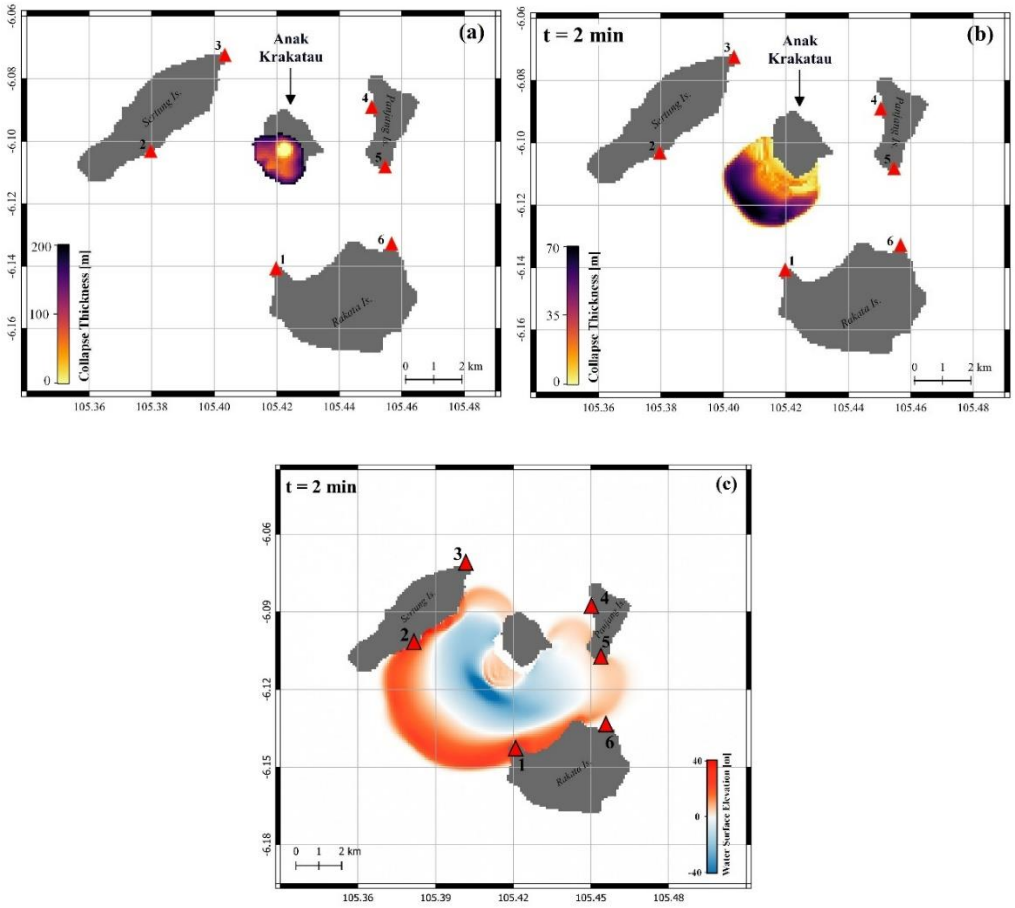

Figure 4.2. The landslide and tsunami generation at 2 min using VolcFlow model. **(a)** Initial collapse with 0.24 km^3 volume. **(b)** Collapse thickness at 2 min after the initial collapse. **(c)** Tsunami propagation simulation at 2 min.

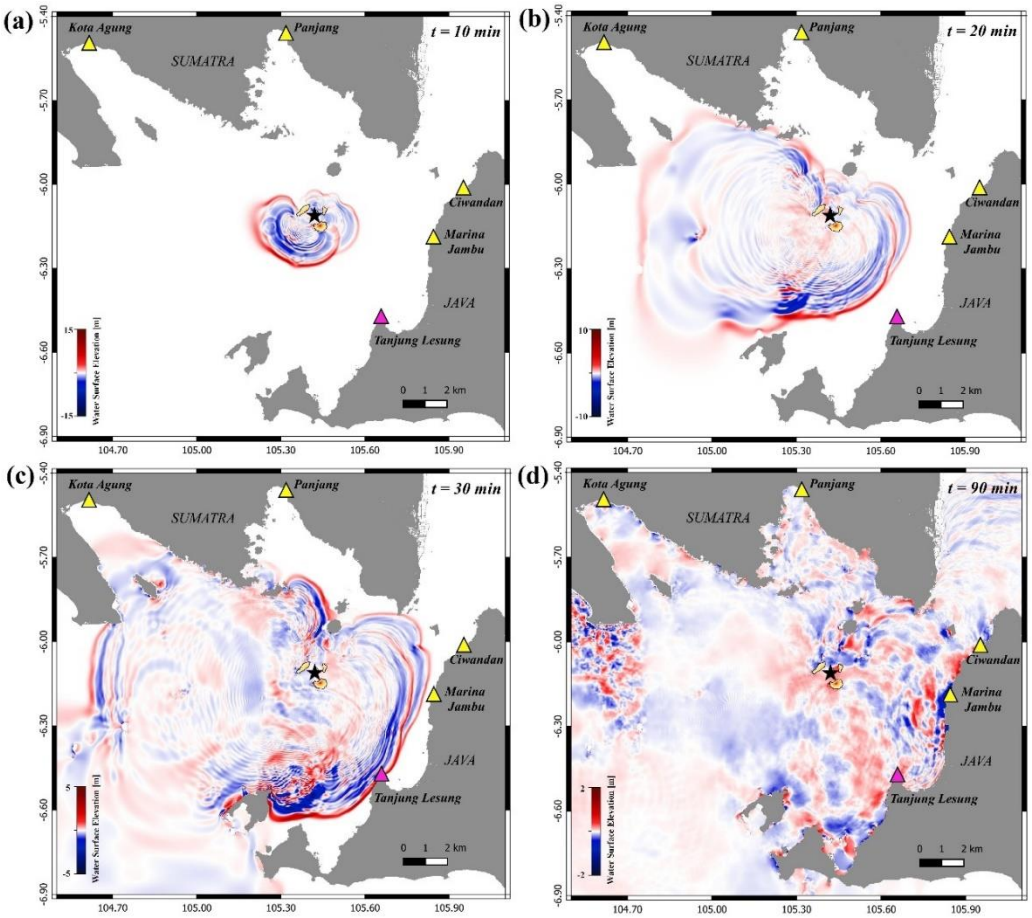

Figure 4.3. Snapshots of tsunami propagation simulation of the 2018 Sunda Strait tsunami at 10 min, 20 min, 30 min, and 90 min (a-d), respectively. Black star indicates the location of Anak Krakatau volcano. Yellow and magenta triangles indicate the real and synthetic tide gauge stations around Sunda Strait, respectively.

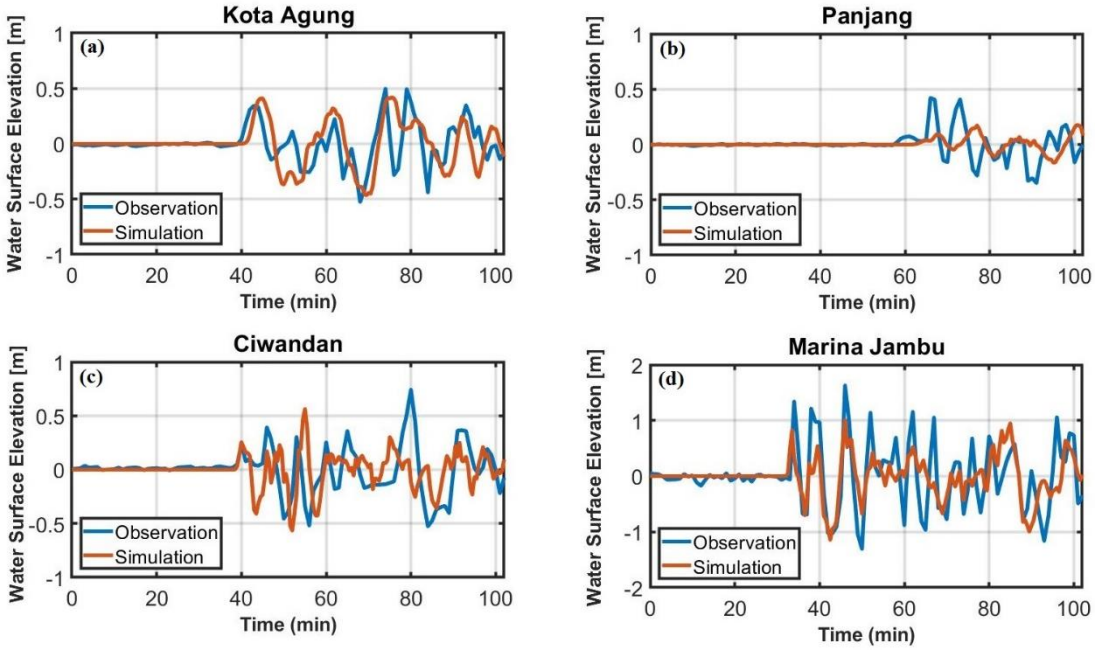

Figure 4.4. Comparison between observed (blue) and simulated (red) tsunami waveforms from 2018 Anak Krakatau event at four tide gauge stations: **(a)** Kota Agung, **(b)** Panjang, **(c)** Ciwandan, and **(d)** Marina Jambu.

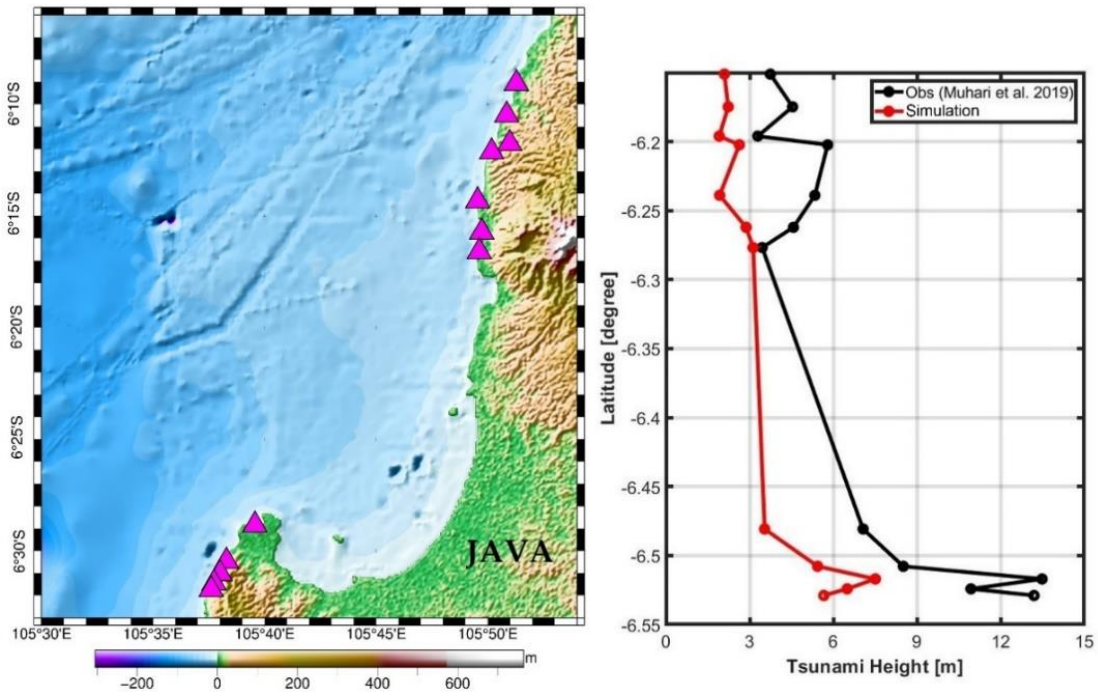

Figure 4.5. Runup height comparison between simulation (red) and observation (black) from the 2018 event along the coast of Java. The triangles in magenta color indicate the surveyed locations by Muhari et al. (2019).

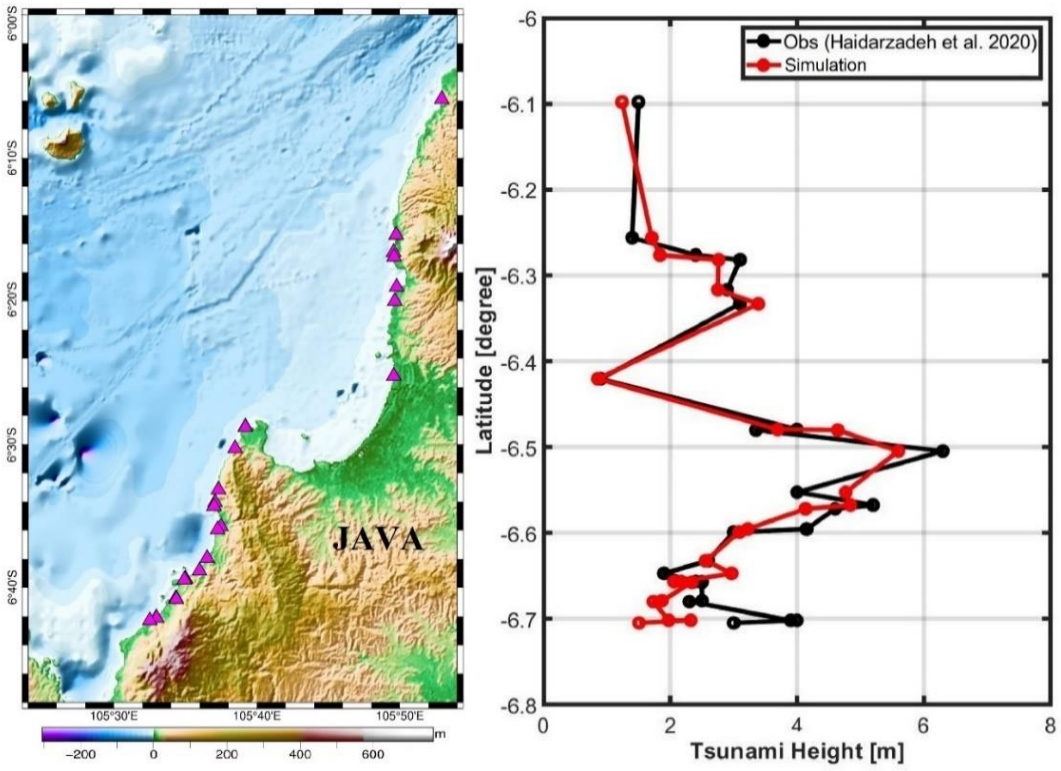

Figure 4.6. Runup height comparison between simulation (red) and observation (black) from the 2018 event along the coast of Java. The triangles in magenta color indicate the surveyed locations by Haidarzadeh et al. (2020).

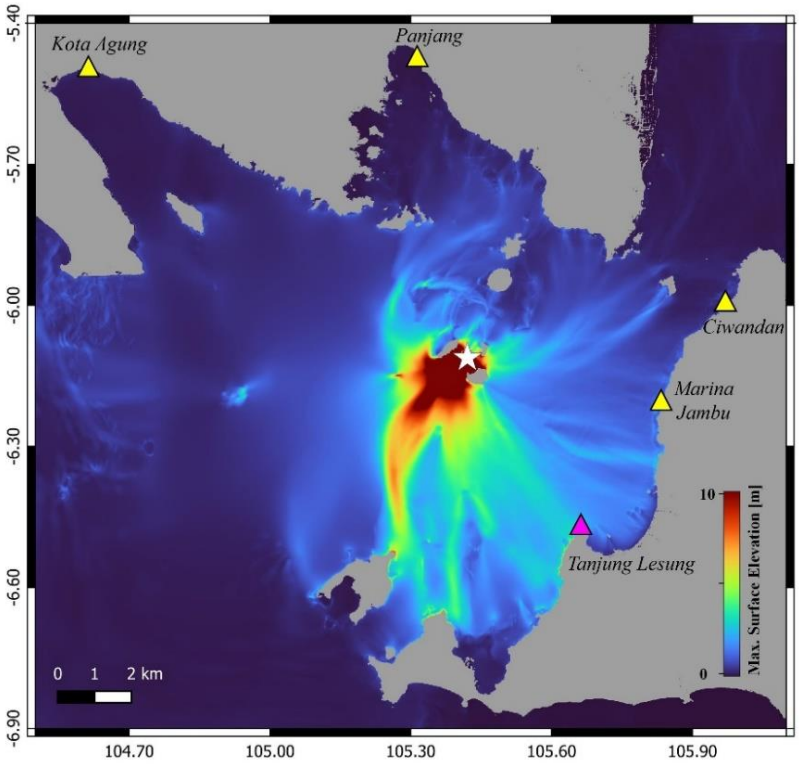

Figure 4.7. Maximum surface elevation from the simulation of the 2018 Sunda Strait tsunami event with the white star indicates the location of Anak Krakatau volcano.

Table 4.1 Comparison of the computed and measured tsunami from the post-tsunami survey of Muhari et al. (2019).

No	Long	Lat	Tsunami Height (m)	
			Measurement	Simulation
1	105.8547	-6.1511	3.74	2.09
2	105.8475	-6.17476	4.54	2.23
3	105.8497	-6.19602	3.29	1.91
4	105.8362	-6.20232	5.8	2.63
5	105.8258	-6.23888	5.34	1.92
6	105.8289	-6.2621	4.57	2.87
7	105.8270	-6.27677	3.45	3.13
8	105.6594	-6.48078	7.07	3.54
9	105.6382	-6.50781	8.51	5.44
10	105.6334	-6.51699	13.49	7.51
11	105.6289	-6.52415	10.94	6.50
12	105.6267	-6.52896	13.2	5.66

Table 4.2 Comparison of the computed and measured tsunami from the post-tsunami survey of Haidarzadeh et al. (2020).

No	Site	Long	Lat	Tsunami Height (m)	
				Measurement	Simulation
1	Sambolo-1	105.8821	-6.0983	1.5	1.24
2	Cilurah	105.8289	-6.2563	1.4	1.71
3	Pondok Paula	105.8260	-6.2764	2.4	1.84
4	Stefani Villa	105.8265	-6.282	3.1	2.76
5	Carita-1	105.8295	-6.3168	2.9	2.75
6	Carita-2	105.8273	-6.3333	3.1	3.39
7	Labuan-2	105.8261	-6.4205	0.9	0.85
8	Tanjung Lesung-1	105.6532	-6.4795	4.0	3.69
9	Tanjung Lesung-23	105.6531	-6.4802	3.4	4.64
10	Kasavana Resort	105.6412	-6.5047	6.3	5.60
11	Joglo Beach House	105.6218	-6.5527	4.0	4.77
12	Banyuasih-1	105.6179	-6.5675	5.2	4.84
13	Banyuasih School	105.6166	-6.5719	4.6	4.13
14	Banyuasih-23	105.6248	-6.5955	4.2	3.22
15	Banyuasih-4	105.6208	-6.5991	3.0	3.09
16	Banyuasih-5	105.6086	-6.6324	2.6	2.56
17	Cisiih Beach	105.5997	-6.6471	1.9	2.97
18	Sumur-1	105.5833	-6.6564	2.4	2.17
19	Sumur-2	105.5833	-6.6568	2.5	2.06
20	Sumur-3	105.5821	-6.6575	2.5	2.34
21	Sumur-4	105.5723	-6.6789	2.5	1.87
22	Sumur-5	105.5726	-6.68	2.3	1.74
23	Ciputih Resort-1	105.5491	-6.7018	3.9	1.97
24	Ciputih Resort-2	105.5497	-6.7018	4.0	2.32
25	Sumur-6	105.5418	-6.7048	3.0	1.51

4.2 Tsunami Forecasting Strategy

4.2.1 Tsunami Characteristic from Anak Krakatau

Development of tsunami warning systems with effective tsunami observation network have become a priority for tsunami prone areas (Mulia et al. 2017). A well-designed tsunami observing network should be carefully constructed for reliable tsunami forecasting (Wang et al. 2020). In present, numerous tsunami monitoring networks are available and deployed in the tsunamigenic area such Japan, New Zealand, Canada, etc. A remarkable tsunami monitoring network called S-net is actively operating for tsunami warning in Japan with 150 ocean bottom pressure sensors (Mochizuki et al. 2016). In the case of the 2022 Tonga eruption, tsunamis were observed by 106 ocean bottom pressure sensors of S-net in Japan (Tanioka et al. 2022). Thus, the existence of tsunami monitoring system is likely to be beneficial for the operation of tsunami forecasting not only for earthquake generated tsunamis but also for non-tectonic tsunamis. In this study, we try to propose a design of tsunami observation network for Anak Krakatau volcano that can be used for real-time tsunami forecasting purposes.

Anak Krakatau volcano is identified as one of the most active volcanoes with continuous intense volcanic activity in Indonesia. As mentioned before, the site of Anak Krakatau volcano and Sunda Strait has been known as tsunami prone zone proven by historical records of tsunamis. Even though it is known as a tsunami-prone area, the tsunami monitoring network is still not fully available in that area. Focusing on the development of tsunami forecasting for volcanic sector collapse, we propose a design for tsunami monitoring network at Anak Krakatau. The Anak Krakatau volcano is surrounded by three uninhabited islands: Sertung, Rakata, and Panjang. In this volcanic island complex, tsunamis generated during the collapse sector of Anak Krakatau propagated

towards the three pathways out between the uninhabited islands before traveling further to the coastal area of Java and Sumatra. Considering these characteristics, we placed six virtual observation stations in the vicinity of volcano to surround the Anak Krakatau and divided the complex of Anak Krakatau into three regions A, B, and C (Fig. 4.8), as monitoring and early tsunami detection. We placed the observation stations on the three islands surrounding Anak Krakatau where each island has two observation stations located on the edge of island. We placed the observation systems in locations that are suitable for the installation of observation stations considering the coastal morphology of the three surrounding islands. Moreover, rapid detection of tsunami was also considered in the placement of observation stations. Currently, tsunami observation stations are not available in the actual locations. Therefore, we addressed our six observation stations here as virtual observation stations. We should note that the six observations here are the minimum requirements number for the application of our tsunami forecasting methods for Anak Krakatau.

4.2.2 Construction of Pre-computed Database

The construction of pre-computed database is conducted by simulating various sector collapse scenarios using topography and bathymetry data around the Anak Krakatau. A topography data with spatial resolution of 0.27 arc-sec was used to create various landslide planes. Then, bathymetry data with 3-arcsec resolution was also used for the numerical simulation. The topography and bathymetry data were obtained from the Geospatial Information Agency of Indonesia and its available for free access (https://tanahair.indonesia.go.id/demnas/). Here, we should note that the topography data of Anak Krakatau used to build the database was data from pre-collapse state of the 2018 collapse and tsunami event. The top elevation of Anak Krakatau volcano from the

topography data has a maximum height of about 250 m above sea level. The cross section showing the elevation of Anak Krakatau volcano from the pre-collapse state is indicated in Fig. 4.9.

The collapse scenarios in this study were created one by one by setting several geometric parameters such as collapse thickness, dip, and strike angle. By varying the geometric parameters, we obtained multiple collapse scenarios of Anak Krakatau with different collapse volumes and directions. The numerical simulation of each collapse scenario was conducted using the combination of VolcFlow and Boussinesq models for a total of 3 min simulations. In each created scenario, the behavior of collapsed material and the generation and propagation of tsunamis of up to 1 min were simulated using VolcFlow model, then switched to the Boussinesq model for estimating only tsunami propagation up to 2 min. The simulation tsunami generation and propagation for the pre-computed database were performed in a similar manner to the analysis of the 2018 tsunami event presented in section 4.1.

The concept of a pre-computed database for tsunami forecasting has been applied in many studies (Tanioka et al. 2014; Gusman et al. 2014; Tanioka and Gusman, 2018). In earthquake studies, the pre-computed tsunami database method has been recognized for its robustness and commonly used for the operation of early tsunami warning system. The pre-computed database for earthquakes usually contains a pre-calculated set of data such as fault models, tsunami waveforms, tsunami inundation, etc. The real-time forecasting process for great earthquakes will be less time consuming by computing the pre-calculated data from various earthquake scenarios (Gusman and Tanioka, 2014). Attributing to the robustness of method, we adopt the concept of pre-computed tsunami database for tsunamis generated by volcanic sector collapse.

In the present study, we constructed a pre-computed tsunami database focusing on the volcanic sector collapse of Anak Krakatau. Our database includes 16 sector collapse scenarios (SC's) with various volumes, locations and sliding directions. Multiple collapse scenarios of Anak Krakatau were created from the topography data and we named all the 16 scenarios in our database as SC1 to SC16 (Fig. 4.10). From those 16 collapse scenarios, we have variations of landslide direction mainly towards the southwest, southeast, north, and west of Anak Krakatau. The range of collapse volume in our database also varied by the variation of the collapse thickness with the largest collapse volume of 0.25 km^3 and smallest collapse volume of 0.04 km^3. The detailed collapse geometry in each scenario and the illustration on the application of collapse thickness variations in our collapse scenario are shown in Table 4.3. and Fig. 4.11. As mentioned before, the early generation and propagation of tsunamis of up to 1 min were simulated using VolcFlow model, then switched to the Boussinesq model for estimating only tsunami propagation in total of 3 min simulation for each scenario. The determination of the switching time here is based on the VolcFlow simulation results, which shows that the significant tsunami generation process under the assumed collapse scenarios is likely to end within 1 min after the occurrence of collapse. Based on our trial simulations, the total elapsed time of 3 min after the collapse was long enough for tsunamis to be generated and propagated through the sea areas between uninhabited islands of Sertung, Rakata, and Panjang. Therefore, we decided to use a total of 3 min numerical simulation for each created collapse scenario in our database. The example of a 3-minutes collapse and tsunami simulation from one of our scenarios is shown in Fig. 4.12. The panel (b-c) in Fig. 4.12 indicates the landslide and corresponding tsunami for 1 minute simulation using VolcFlow model, and Fig. 4.12d

shows the subsequent tsunami propagation simulation up to 3 min by Boussinesq model. The same simulation was conducted for all 16 collapse scenarios that were created before.

The tsunami generation and simulation from our database are computed by total of 3 min simulations. As mentioned before, the main reason is that the total elapsed time of 3 min after the collapse was long enough for tsunamis to be generated, captured by the virtual observation stations, and propagated through the sea areas between uninhabited islands (Fig. 4.12d). At the time of 3 min after the collapse, significant components of the tsunami were located within each region as shown in Fig. 4.13, and similar results were obtained in any assumed scenario. Towards the next step, we stored a set of important data from the 3 min tsunami generation and propagation simulation in each scenario into the database. There are three important pieces of data that must be stored in the database for each collapse scenario: synthetic waveforms at virtual stations (Fig. 4.13b-g), surface water elevation (Fig. 4.13h-j), and flux distribution (Fig. 4.13k-p). Here, we stored the synthetic waveform from the simulation with sampling interval of 2-s for the virtual observation stations. Implementing the region division, we also stored the synthetic waveforms and the spatiotemporal changes in the water surface level and flux distribution for each regions A, B, C, into the database (Fig. 4.13).

4.2.3 Real-time Tsunami Forecasting

As briefly mentioned in the previous section, we consider that tsunami propagated from the Anak Krakatau volcano consisting of three separate elements: tsunami waveforms propagating through region A, B, and C, where each region covers a different pair of two observation stations. Considering this characteristic, we propose a real-time tsunami forecasting strategy by determining the best collapse scenario representing tsunamis in each region (A, B, C). Then, used the pre-computed surface water elevation

and flux distribution from the best scenarios at each region A, B, C, as initial condition for the real-time simulation.

In the implementation of tsunami forecasting, the best scenario for each input A, B, C is required as an initial condition for real-time simulation. The selection process of the best scenario depends on the observed waveforms at six tsunami monitoring stations surrounding Anak Krakatau. In our tsunami forecasting strategy, the scenario in the database that has the most reasonable waveforms to the observed waveforms is firstly determined as the best scenario. For region A, the best scenario is searched by comparing the observed and pre-computed waveforms at the two virtual stations 1 and 2 located at the end of region A. The changes in the water surface level and flux at the 3 min in region A can therefore be determined based on the best scenario, because they have been computed and stored in the database. For region B, the best scenario with considerable pre-computed water surface and flux distribution is obtained by comparing the observed and pre-computed waveforms at stations 5 and 6. Lastly, for region C, waveforms comparison at stations 3 and 4 will result in the best scenario with considerable pre-computed water surface and flux distribution. Three collapse scenarios are determined as the best scenario, and these can be identical or combination of different scenarios. By spatially integrating the spatial distributions of water surface level and flux in regions A, B, and C under the identified scenarios at 3 min after the collapse, they can be inputs to a single large-scale tsunami propagation simulation for Sunda Strait area. Real-time tsunami estimation for the coasts of Java and Sumatra can be conducted based on this propagation simulation. The important point of this method is that this method allows us to conduct real-time tsunami estimation without considering any source in the actual tsunami event associated with a volcanic eruption of Anak Krakatau. In our study,

generally we applied two types of numerical simulations. First, a numerical simulation uses a combination of the VolcFlow and Boussinesq models for simulating the sector collapse and tsunami propagation to construct the pre-computed database that explained in previous section. Second, we used only the Boussinesq model to forecast the tsunami without any estimation on collapse source for the demonstration of our real-time forecasting simulation.

In the real-time application, the most suitable scenarios for each region A, B, and C are identified based on a result from waveform comparison at observation stations. For the comparison, a waveform fitting procedure between pre-computed and observed waveforms at six observation stations with a time window of 100 s is conducted by Root Mean Square Error (RMSE) analyses. The initial collapse time between the actual and pre-computed scenarios might be different due to the different initiation of collapse. Then, a direct comparison between observed and pre-computed waveforms at observation stations may result in large misfits caused by different tsunami waveform phases (Gusman et al. 2014). To avoid this problem, we applied a time shift procedure by shifting the pre-computed waveforms to the observed waveforms every 2-s while calculating the RMSE values. Thus, the best scenario with the corresponding optimal pre-computed waveforms was obtained by minimizing the RMSE between the observed and pre-computed waveforms. The RMSE values are calculated using simple formula that can be written as:

$$\mathrm{RMSE} = \sqrt{\frac{\sum_{i=1}^{n}(S_i - O_i)^2}{n}} \qquad (7)$$

where n is the number of data points, Si and Oi are the time series of simulated data and actual observed data, respectively. Using this simple RMSE calculation, it allows us to determine the best scenario without any complicated procedure and less time consuming. In order to obtain the best tsunami wave field to explain the six observed tsunami waveforms, the timing of three scenarios to put in the second type tsunami computation is defined by the time shifts procedure. This time-shifting process involves comparing pairs of waveforms, resulting in a calculated RMSE value in each region A, B, and C. An example of time shift procedure is shown in Figure 4.14. In region A, we compared the pre-computed and observed waveforms at sites 1 and 2 which resulted in an identical optimal time shifting value (τ_a) (Fig. 4.14a-c). For region B, comparison of pre-computed and observed waveforms at sites 5 and 6 will result in optimal time shift value (τ_b) (Fig. 4.14d-f). Lastly in region C, comparison of waveforms at sites 3 and 4 will result in optimal time shift value (τ_c) (Fig. 4.14g-i). Therefore, the most suitable initial collapse scenarios to respectively reproduce the observed waveforms in three regions can be identified through this procedure. Using the identified best scenarios and optimal shifting values, we synthesized corresponding spatial distributions of water surface level and flux at 3 min after the collapse by integrating those in three regions A, B, and C. Then, use it as input/initial conditions for single large tsunami numerical simulation using Boussinesq model.

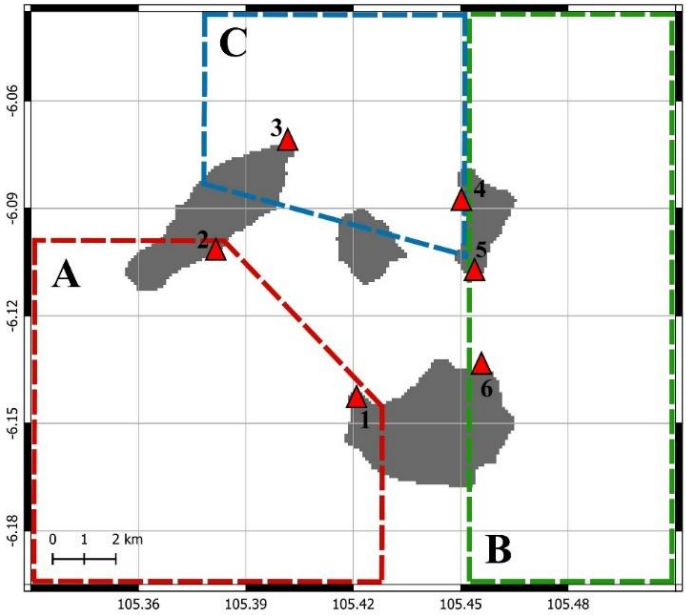

Figure 4.8. Anak Krakatau complex divided into three regions A, B, and C for tsunami forecasting purposes (red, green, and blue dashed line). Each region A, B, and C is covered by a pair of virtual observation stations indicated by red triangles. Region A covers pair of stations 1 and 2, region B covers pair of stations 5 and 6, lastly region C covers pair of stations 3 and 4.

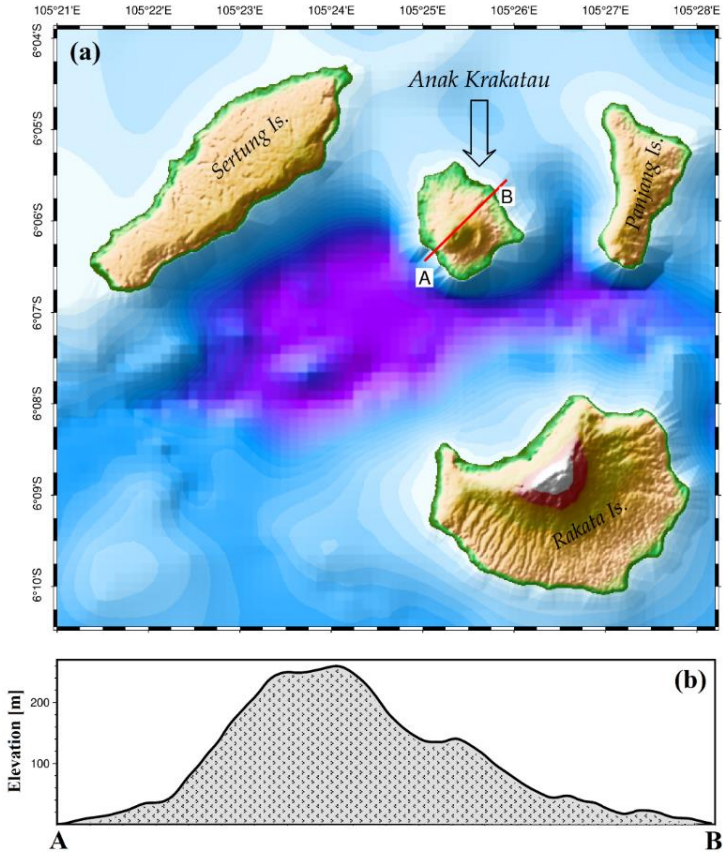

Figure 4.9. (a) Topography data of Anak Krakatau from the pre-collapse state in 2018. **(b)** Pre-collapse elevation of Anak Krakatau from the cross-section A-B indicated in (a).

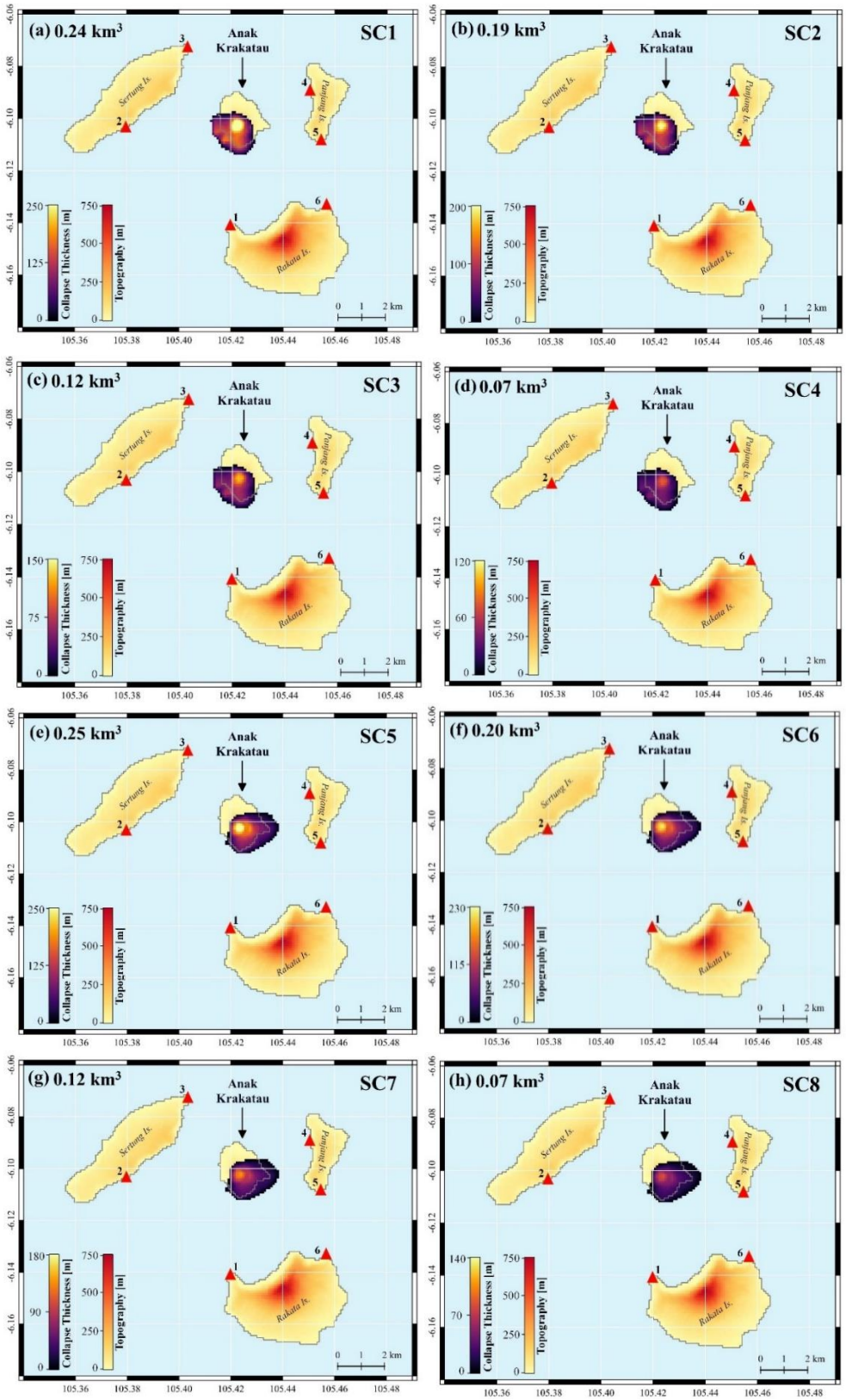
(a) 0.24 km³
SC1
(b) 0.19 km³
SC2
(c) 0.12 km³
SC3
(d) 0.07 km³
SC4
(e) 0.25 km³
SC5
(f) 0.20 km³
SC6
(g) 0.12 km³
SC7
(h) 0.07 km³
SC8
Anak Krakatau
Sertung Is.
Panjang Is.
Rakata Is.
Collapse Thickness [m]
Topography [m]
0 1 2 km
105.36 105.38 105.40 105.42 105.44 105.46 105.48
-6.06 -6.08 -6.10 -6.12 -6.14 -6.16

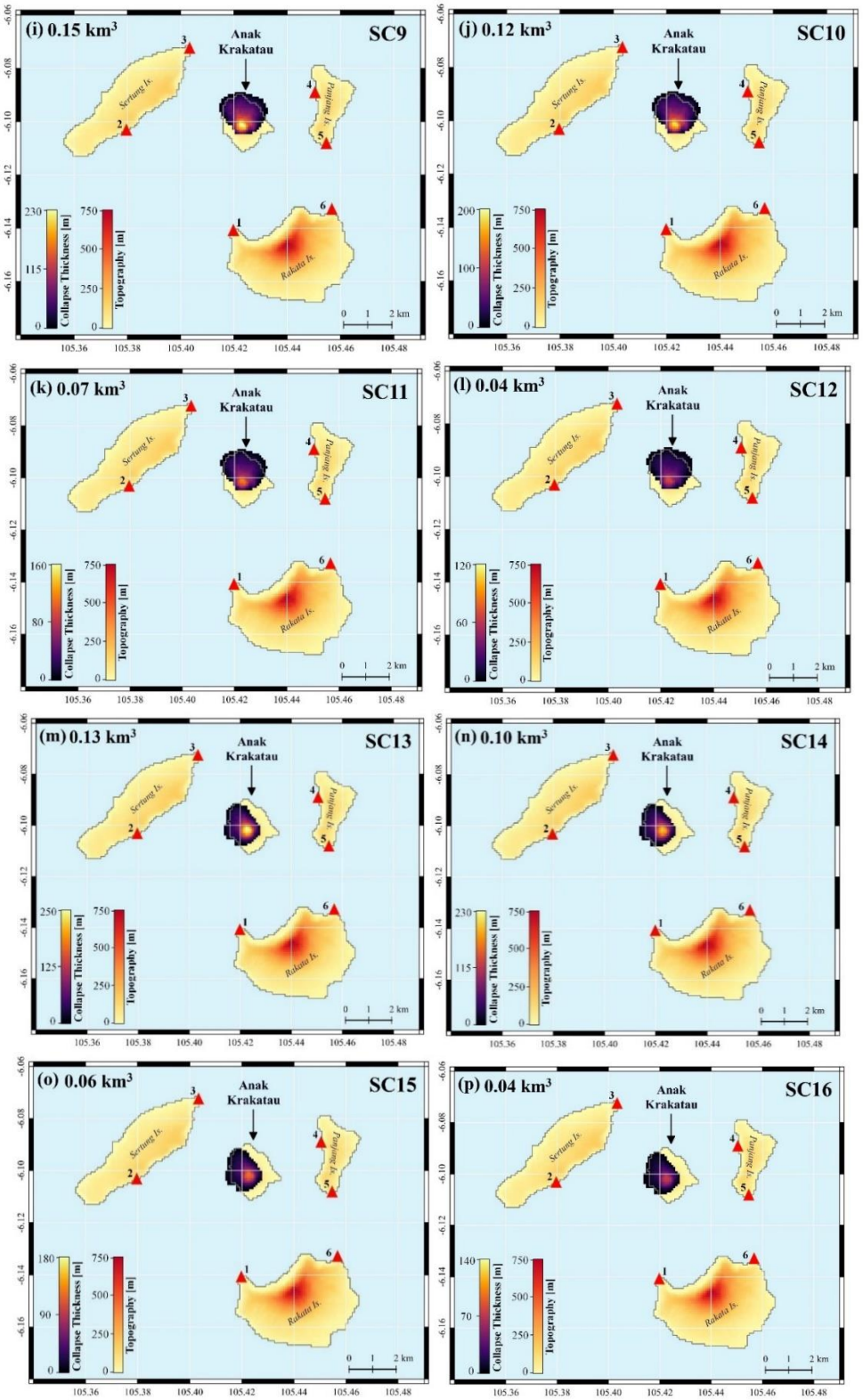

Figure 4.10. Various collapse area and volumes from 16 scenarios named SC1 to SC16 inside the database (a-p).

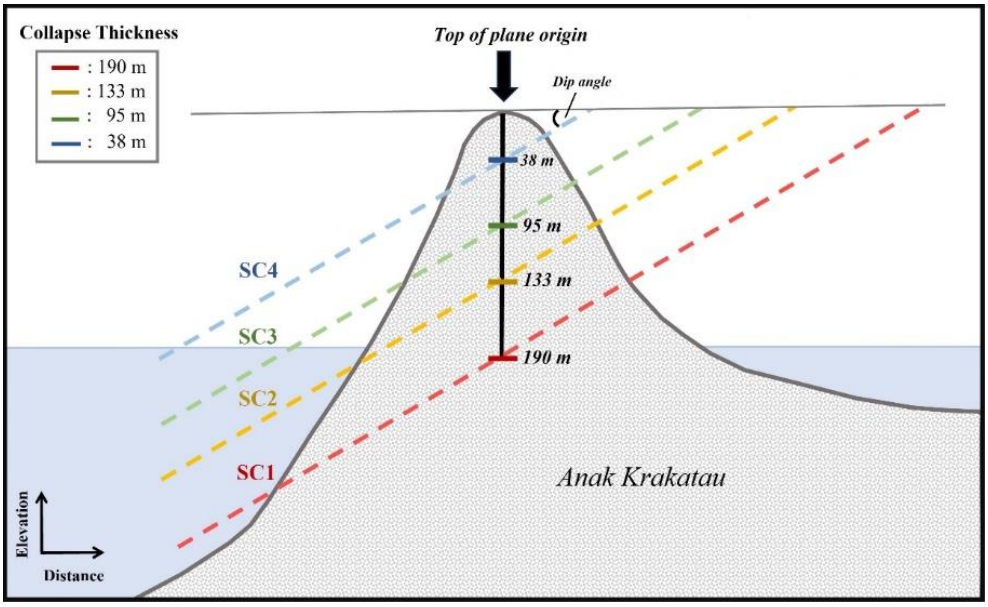

Figure 4.11. Illustration on collapse thickness variations in scenario 1-4 (SC1-SC4) based on the Table. 4.3. The dashed lines show the landslide plane, and the thick-colored lines indicate the collapse thickness from the top of plane in SC1-SC4, respectively.

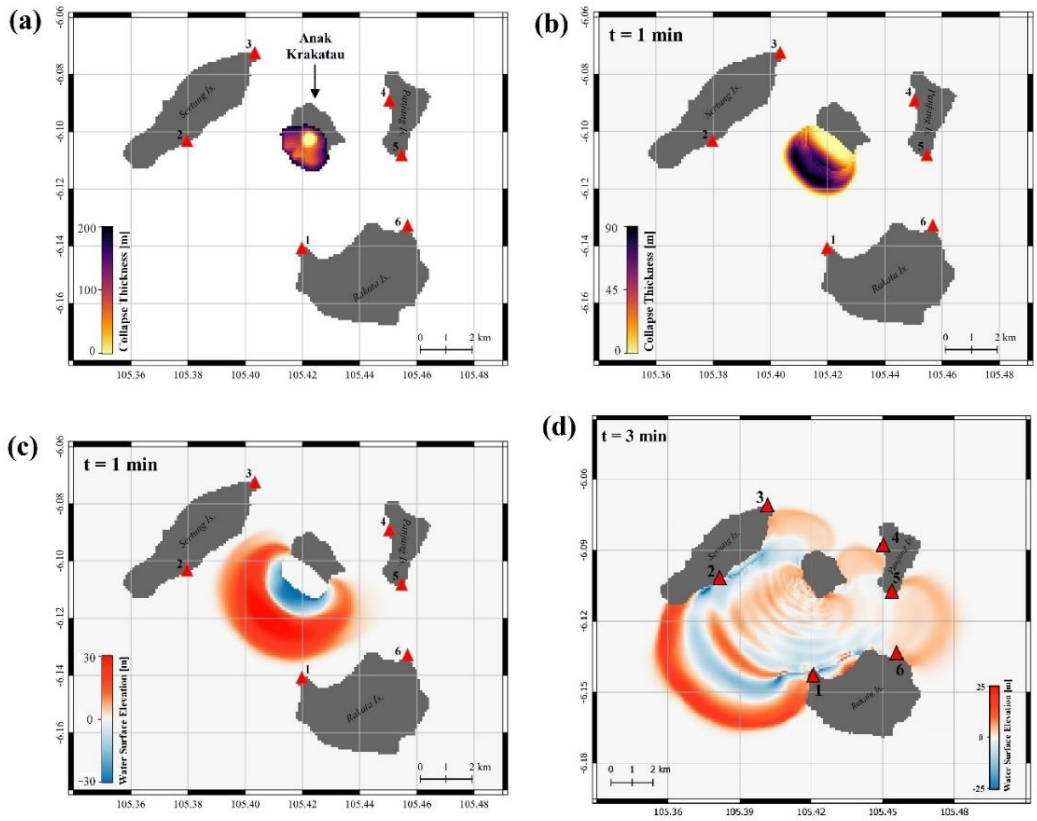

Figure 4.12. Example of a 3-min simulation for pre-computed database. **(a)** Collapse thickness scenario. **(b-c)** Landslide and corresponding tsunami propagation for 1 minute simulation using VolcFlow model. **(d)** Subsequent tsunami propagation simulation up to 3 min by Boussinesq model.

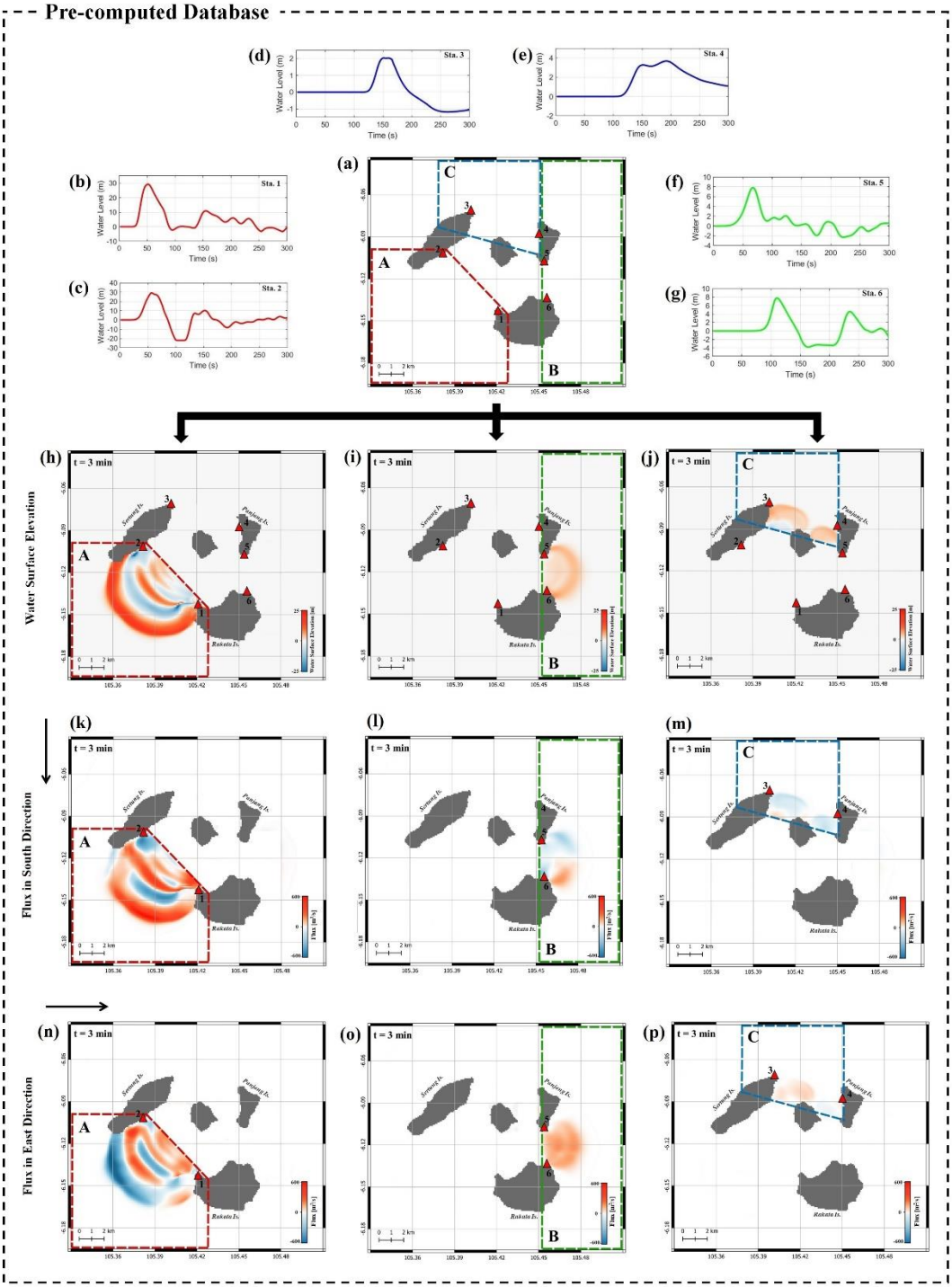

Figure 4.13. Data for the pre-computed database. **(a)** Three regions A (red-dashed line), B (green-dashed line), and C (blue-dashed line). **(b-g)** Synthetic waveforms at six virtual observation stations. **(h-j)** Surface elevation distribution in three regions A, B, C. **(k-m)** Flux distributions in south direction, and **(n-p)** east direction, in regions A, B, C.

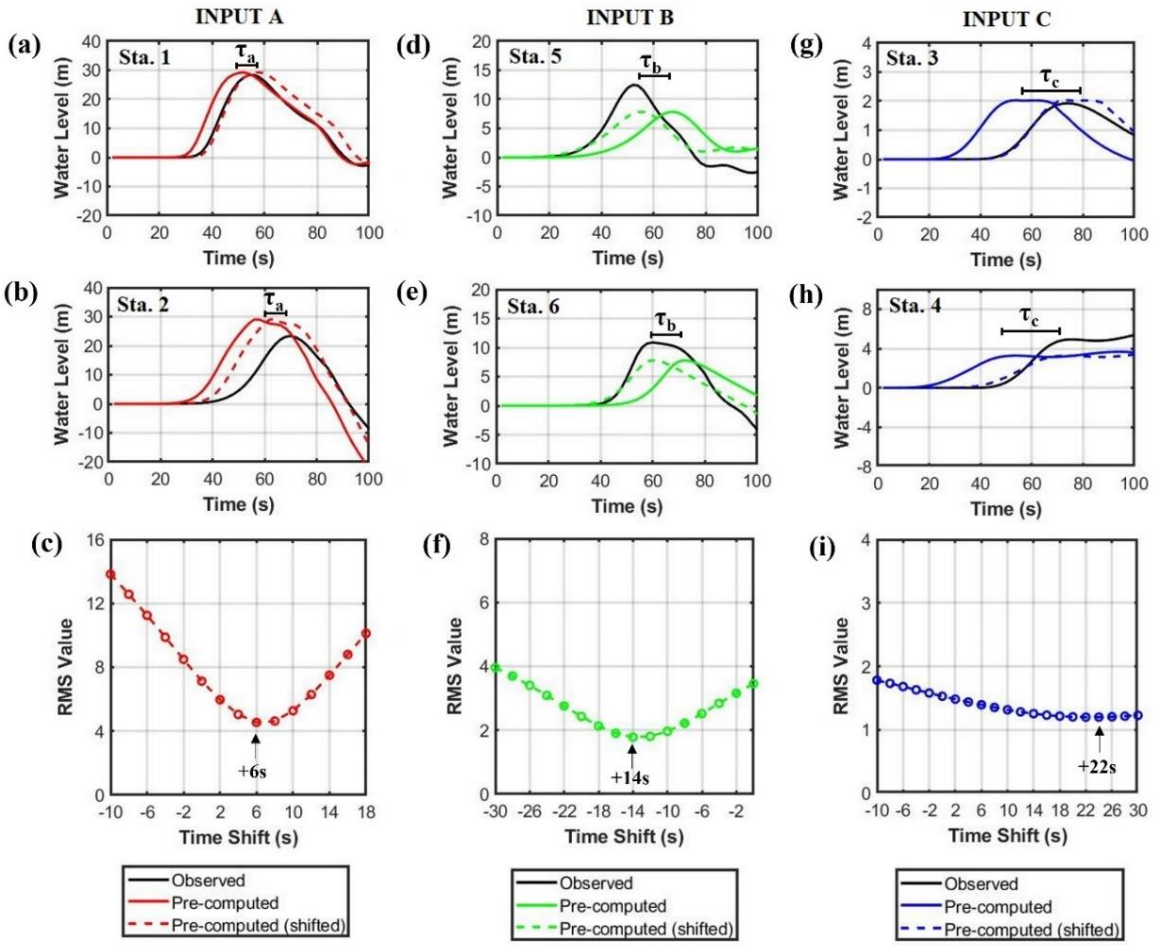

Figure 4.14. Example of waveform fitting procedure to obtain best combination scenario by RMSE calculation and time-shifting for inputs A, B, and C using each pair of stations**.** Black arrows indicate the smallest RMSE misfit (best scenario) with considerable optimal time shifts.

Table 4.3. Geometry parameter of each collapse scenario in the database

ID	Dip (°)	Strike (°)	Thickness (m)	Volume (km^3)
SC1	9	120	190	0.24
SC2	9	120	133	0.19
SC3	9	120	95	0.12
SC4	9	120	38	0.07
SC5	8	50	200	0.25
SC6	8	50	140	0.20
SC7	8	50	100	0.12
SC8	8	50	40	0.07
SC9	5	270	118	0.15
SC10	5	270	83	0.12
SC11	5	270	59	0.07
SC12	5	270	24	0.04
SC13	7	190	200	0.13
SC14	7	190	140	0.10
SC15	7	190	100	0.06
SC16	7	190	40	0.04

4.3 Numerical Experiments of Tsunami Forecasting

4.3.1 Test Case 1

Krakatau complex has relatively deep water in the southern part of the Anak Krakatau volcano, where the 1883 post-eruption caldera is situated. The location of Anak Krakatau, which is partially built on the steep edge of the caldera, makes it more unstable and prone to volcanic collapse (Deplus et al. 1995; Giachetti et al. 2012). As consequences of the position, the slope in the south-southwest side of Anak Krakatau is steeper than the slope in the west side (Stehn et al. 1929; Giachetti et al. 2012). With the steep slope and continuous growing of volcano towards southwest, the flank collapse on the south-southwest part of Anak Krakatau cannot be excluded (Deplus et al. 1995). Considering the instability of the structure, we created a possible collapse scenario for Test Case 1. The first test case involved a hypothetical collapse scenario of 0.25 km^3 total collapse volume with the main collapse area located in the southern part of the Anak Krakatau volcano. The collapse area and thickness for this first scenario is shown in Fig. 4.15. Here, we should note that the hypothetical collapse scenario of Test Case 1 is not included in our pre-computed collapse database and designated only for this numerical experiment. Furthermore, the hypothetical collapse scenario of Test Case 1 was simulated by two different numerical simulations. For the first type, tsunami numerical simulation is conducted by simulating the collapse and tsunami using combination of VolcFlow and Boussinesq models as assumption of the future collapse event. For the second type, we applied the forecasting method and simulated the tsunami using only Boussinesq model to test and demonstrate our real-time forecasting method. We named the result of the first and second type of numerical simulation as synthetic and forecasted, respectively. The

performance of forecasting will be assessed by comparing the waveforms from those two different computations at five locations around Sunda Strait.

In the demonstration of tsunami forecasting, first we compare the synthetic waveforms at virtual observation stations computed by first type numerical simulation mentioned before. Then, compare it with the pre-computed waveforms from our database. Applying the procedure for real-time forecasting, we compared the synthetic and pre-computed waveforms at the six virtual observation stations. Waveform fitting analyses by RMSE misfit calculation was then performed to obtain the initial condition for the regions A, B, and C. Waveform fitting together with time shift procedure at sta. 1 and 2 resulted in the RMSE value variations to search for the best scenario in region A (Fig. 4.16a-d). Then, applying the procedure for sta. 5 and 6 resulted in the RMSE value for the best scenario in region B (Fig. 4.16e-h). Lastly, the best scenario for region C was obtained by finding the smallest RMSE resulted from the waveform fitting procedure on sta. 3 and sta. 4 (Fig. 4.16i-l). Based on the waveform fitting result, we obtain the best combination scenario for inputs A, B and C, that is, SC2 (0.19 km^3), SC7 (0.12 km^3), and SC8 (0.07 km^3), with optimal time shifts of +4, +4, and +22 s, respectively (Fig. 4.16). The surface elevation and flux distributions at the time of 3 min in those three best scenarios inside the database were then used as the initial conditions for the large-scale tsunami propagation simulation by the Boussinesq model. We integrate those three scenarios as initial condition while considering the time shift value for each input.

Tsunami propagation at 3.5 min is shown in Fig. 4.17. The forecasted waveforms were compared to the synthetic waveforms (i.e., observation in the real case) from the first type numerical simulation at five locations around Java and Sumatra island (Fig. 4.18). The comparison showed that the first tsunami peak and maximum amplitude

generally matched well with the observations at the five locations. From this hypothetical scenario, the significant tsunami height was forecasted at Tanjung Lesung, Marina Jambu, and Ciwandan stations with maximum amplitudes of 3.8, 1.2, and 0.5 m, while smaller maximum amplitude of 0.3 and 0.2 m were forecasted at Kota Agung and Panjang stations, respectively.

4.3.2 Test Case 2

Volcanic edifices are naturally unstable because of the continuous change and accumulation rates of volcanic deposits (Paris, 2015). Therefore, mass failures can occur in different parts of the volcano with various scales. Considering the potential collapse variety, we assumed a different hypothetical scenario for Test Case 2 to further assess the performance of our method. In this case, we created a sector collapse scenario with a total collapse volume of 0.21 km^3, with the collapse area concentrated in the eastern part of the volcano (Fig. 4.19). The collapse volume for Test Case 2 is smaller than the collapse volume used for Test Case 1 before. The forecasting performance and the impact of tsunami to the coastal area of Java and Sumatra will be assessed using the variation of collapse volume and direction. The hypothetical collapse scenario for Test Case 2 is not included in our database and newly created for the forecasting assessment. The numerical simulation of tsunami was conducted through the same process as the previous test case with two types of computation. The performance of the forecasting is assessed by comparing synthetic and forecasted tsunami waveforms at five locations around Sunda Strait.

The waveform fitting results indicated a combination of SC8 (0.07 km^3), SC8 (0.07 km^3), and SC5 (0.25 km^3) as the most suitable inputs A, B, and C, respectively (Fig. 4.20). The surface elevation and flux distribution at 3 min provided by the best

combination of scenarios with optimal time shift of +14 s, -6 s, and -14 s were used as the initial conditions for the large-scale simulation. The tsunami propagation at 3.5 min can be seen in Fig. 4.21. For validation, we compared the synthetic and forecasted waveforms at five locations. The synthetic waveforms are resulted from the numerical simulation of tsunami using collapse source. The forecasted waveforms are resulted from the forecasting simulation method that used integrated water surface level and flux distribution from our database. The comparison of synthetic and forecasted waveforms is shown in Fig. 4.22. The comparison showed that the first tsunami peak and maximum amplitude generally matched well with the simulated waveforms at the five locations. At the location of Tanjung Lesung and Marina Jambu, tsunami arrivals are about 30 min and 33 min with first tsunami wave height of about 1 m. The initial collapse sector is situated at the east part of Anak Krakatau volcano, then the directivity of the landslide may become the reason of the significant tsunami height at area of Tanjung Lesung and Marina Jambu as tsunami leading wave propagating towards the coast of Java. At the other locations of Kota Agung and Panjang, the forecasted waveforms were slightly ahead of the arrival time compared with the synthetic waveforms. In this second case, although there were small discrepancies in the tsunami arrival time, we considered that the forecasted waveforms were generally acceptable for real-time tsunami warnings.

4.3.3 Test Case 3

Considering a collapse scenario with various directions and volumes, we initiated the last hypothetical collapse scenario to evaluate the accuracy of our tsunami forecasting method throughout same process with two previous cases. This last hypothetical scenario involved a volcanic collapse volume of 0.20 km^3 with the main collapse situated in the northwest part of Anak Krakatau volcano. Here, Test Case 3 involved the smallest

collapse volume compared with the other previous test cases. The collapse thickness of the hypothetical scenario of Test Case 3 is shown in Fig. 4.23. Anak Krakatau is built on the steep wall of 1883 Krakatau caldera, and it is mainly active on its southwest side (Giachetti et al. 2012). The collapse situated at the other area is also possible due to the unstable edifice that accumulated from the eruption phase. Due to the complex topography and the existence of Krakatau caldera, the water depth at the south part of Anak Krakatau is much deeper than the other parts. Therefore, we assumed that collapse volume in the south and southwest of Anak Krakatau can be much higher than collapse at the other area.

Waveform fitting and RMSE misfit analyses suggested a combination scenario of SC16 (0.03 km^3), SC16 (0.03 km^3), and SC13 (0.13 km^3), with optimal time shift of 0, +14, and 0 s, respectively, as initial condition (Fig. 4.24). The large-scale tsunami simulation was conducted using surface elevation and flux distribution from the combination of the best scenarios as initial conditions. Fig. 4.25 shows the tsunami propagation at 3.5 min. A comparison between the synthetic (i.e., observation in the real case) and forecasted waveforms at the five locations for Test Case 3 is shown in Fig. 4.26. The results indicated that the tsunami arrival time was explained well by the forecasted waveforms. However, the forecasted tsunami waveforms from our simulation were slightly underestimated at the five tide gauge locations. This was possibly caused by lack of scenario variations in the database, so that the initial condition in the final simulation is not at optimum combination.

Numerical experiments using three different hypothetical collapse scenarios in this study show that this method can produce appropriate tsunami forecast even for collapse scenarios that are not included in the database. These findings indicate the

robustness of the forecasting method proposed in this study. Taking general analysis, the numerical experiments using three different hypothetical collapse scenarios resulted in reliable forecasting performance targeted the coastal of Java and Sumatra.

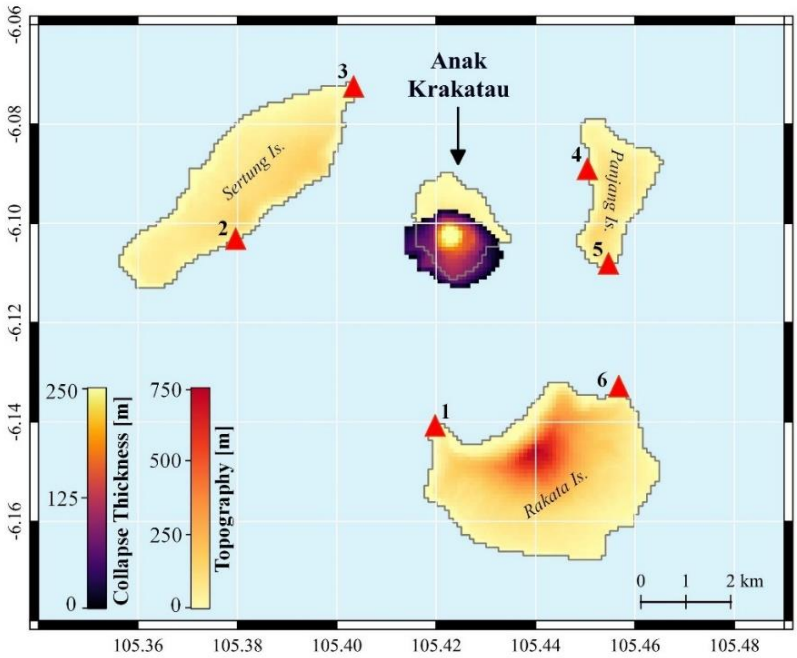

Figure 4.15 Hypothetical collapse scenario with total collapse volume of 0.25 km^3 for Test Case 1.

INPUT A

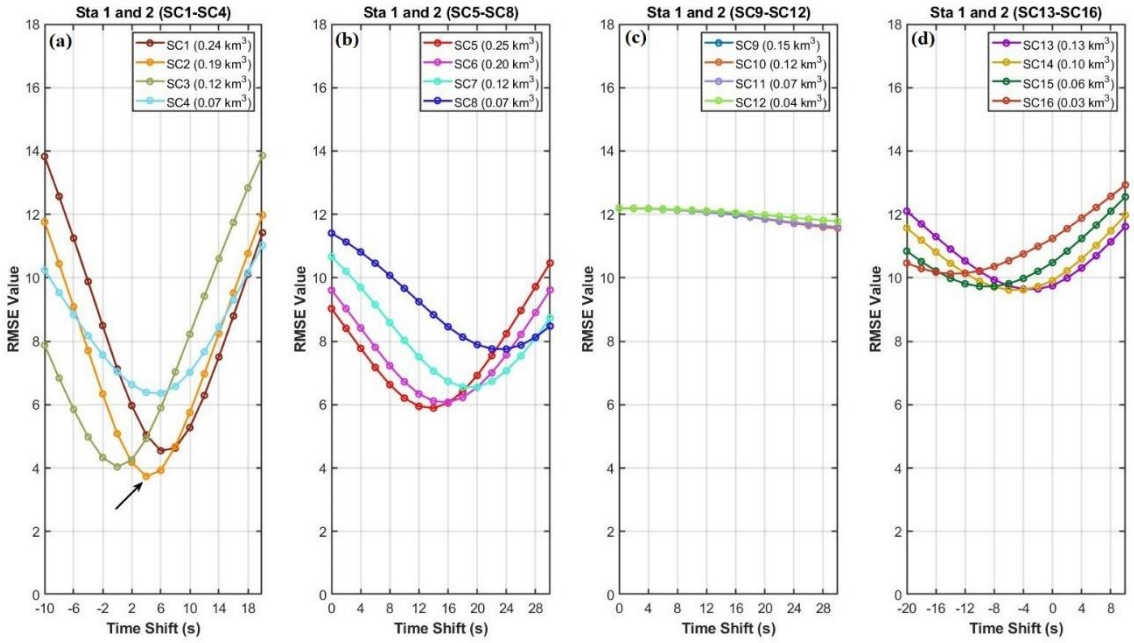

INPUT B

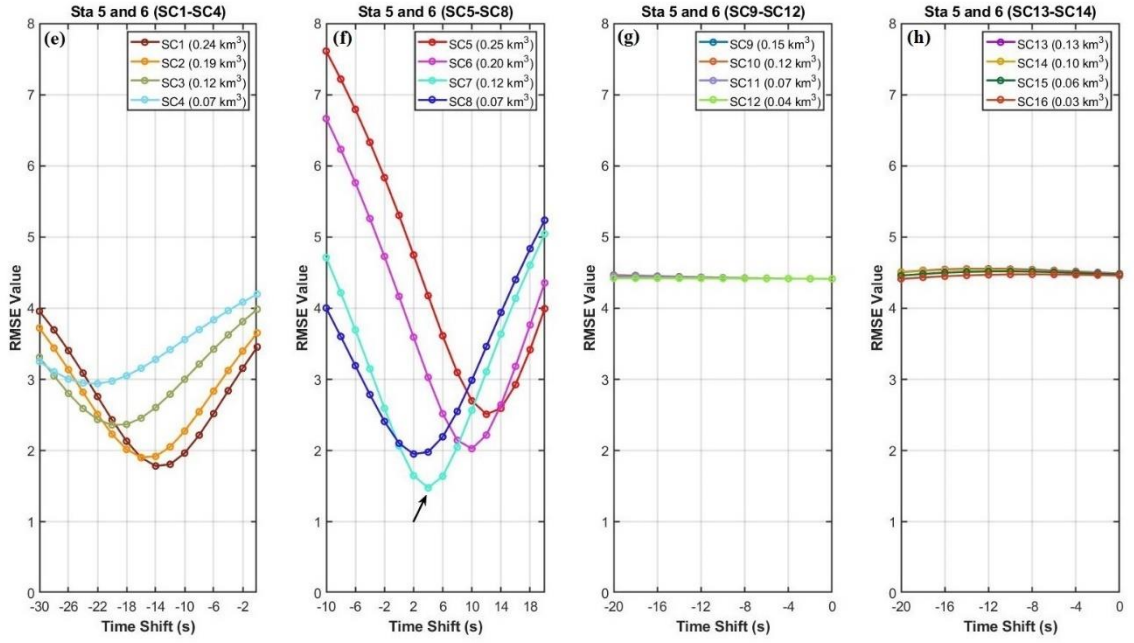

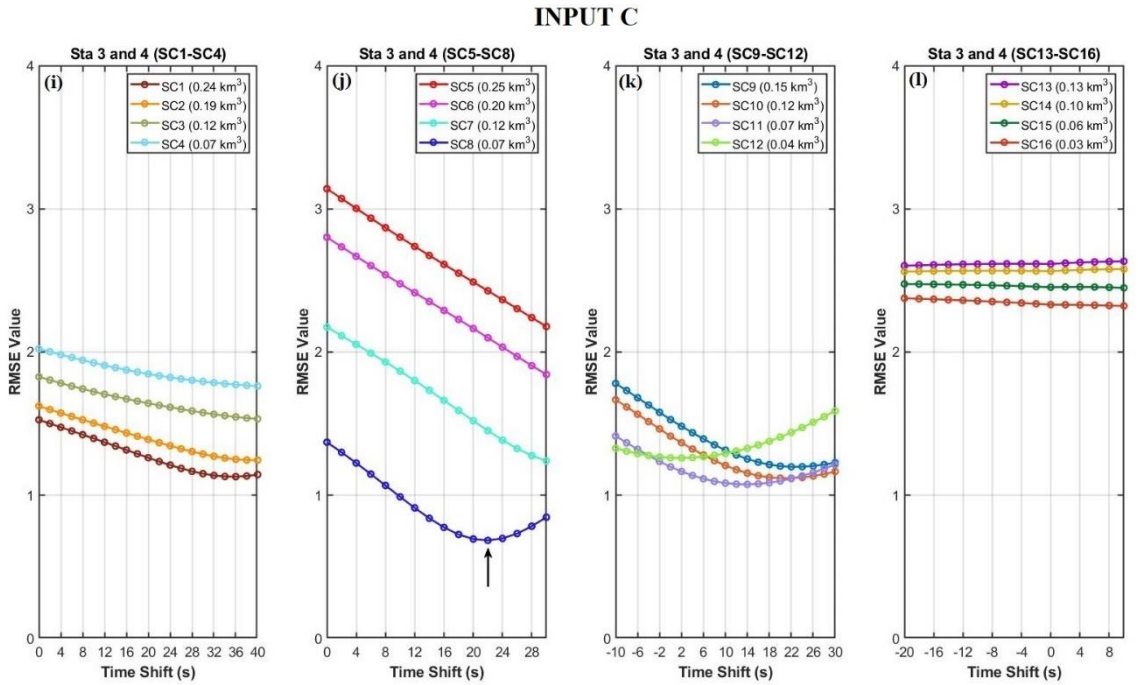

Figure 4.16 RMSE value and considerable optimal time shift for selecting initial conditions in region A, B, and C of Test Case 1. The RMSE values were calculated for all scenarios in database (SC1-SC16) at pair of station 1 & 2 for Input A **(a-d)**, station 5 & 6 for Input B **(e-h)**, and station 3 & 4 for Input C **(i-l)**. Black arrows indicate the best scenario with smallest RMS misfit and optimal time shift.

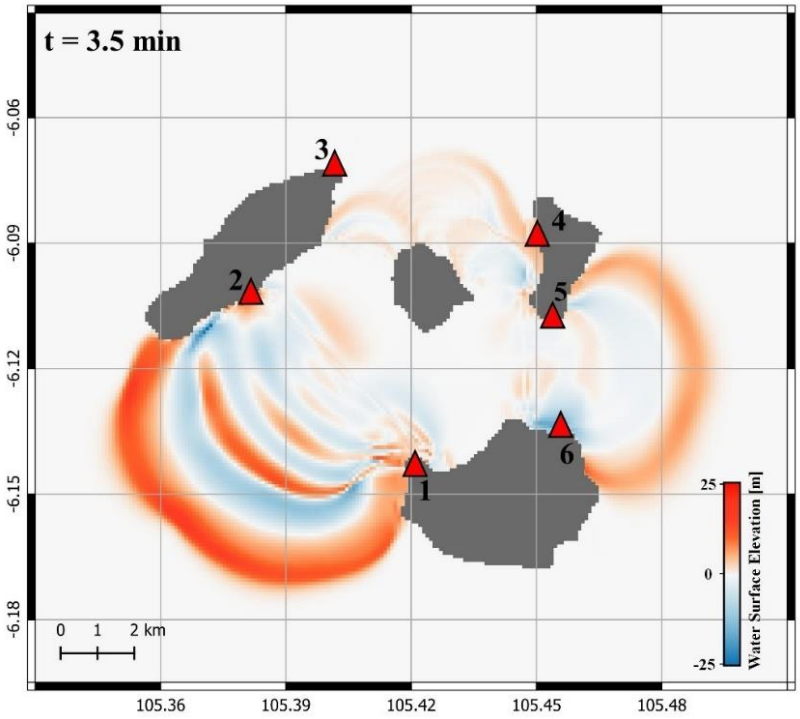

Figure 4.17 Tsunami propagation simulation at 3.5 min using the initial condition from the best combination scenarios from the database for Test Case 1.

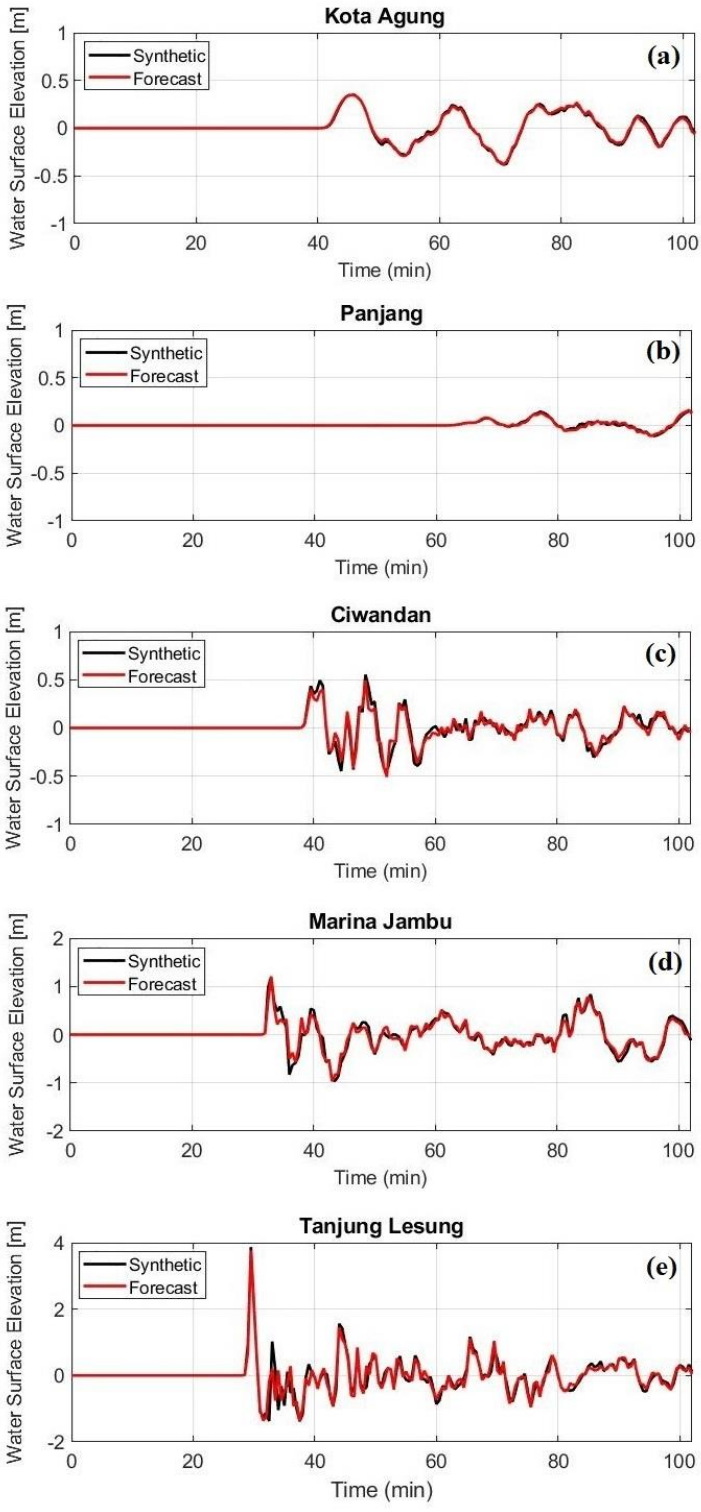

Figure 4.18 Comparison between synthetic (black) and forecasted (red) waveforms from Test Case 1 at five locations: **(a)** Kota Agung, **(b)** Panjang, **(c)** Ciwandan, **(d)** Marina Jambu, and **(e)** Tanjung Lesung.

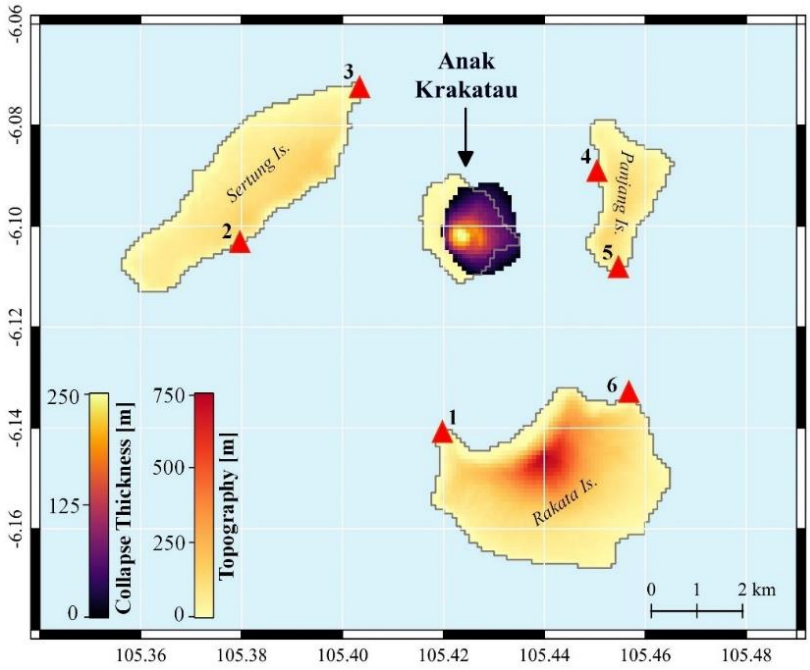

Figure 4.19 Hypothetical collapse scenario with total collapse volume of 0.21 km^3 for Test Case 2.

INPUT A

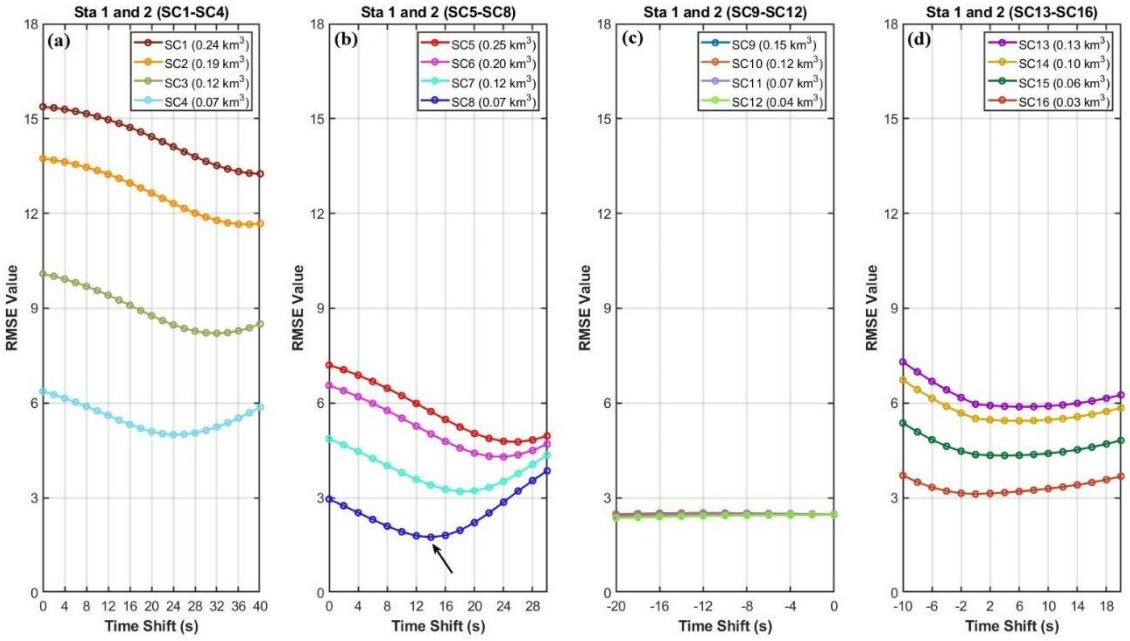

INPUT B

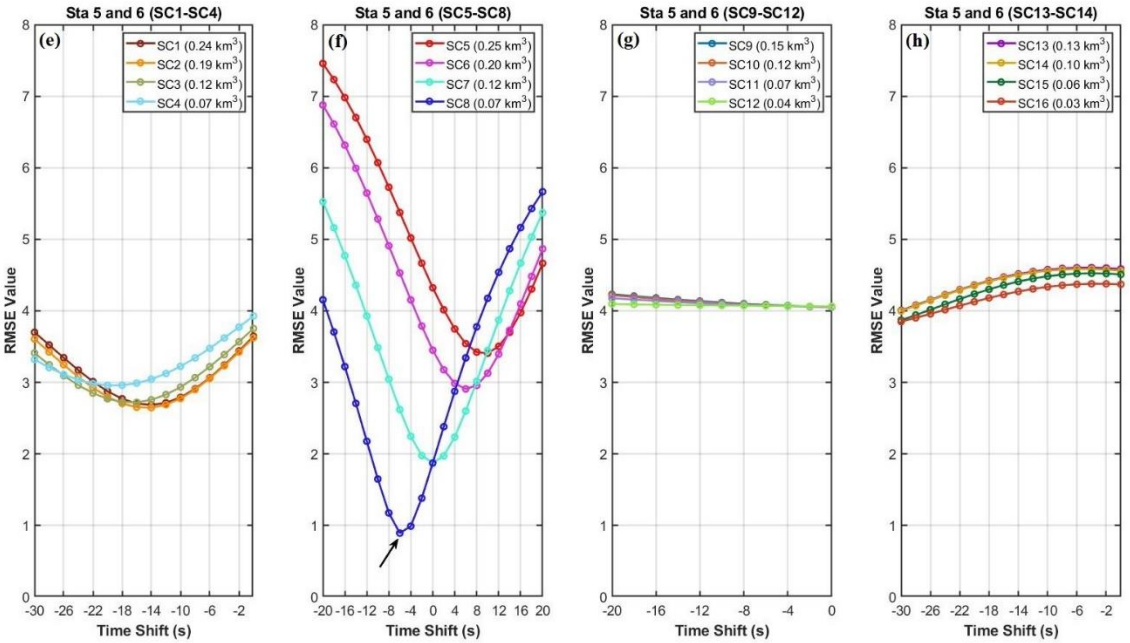

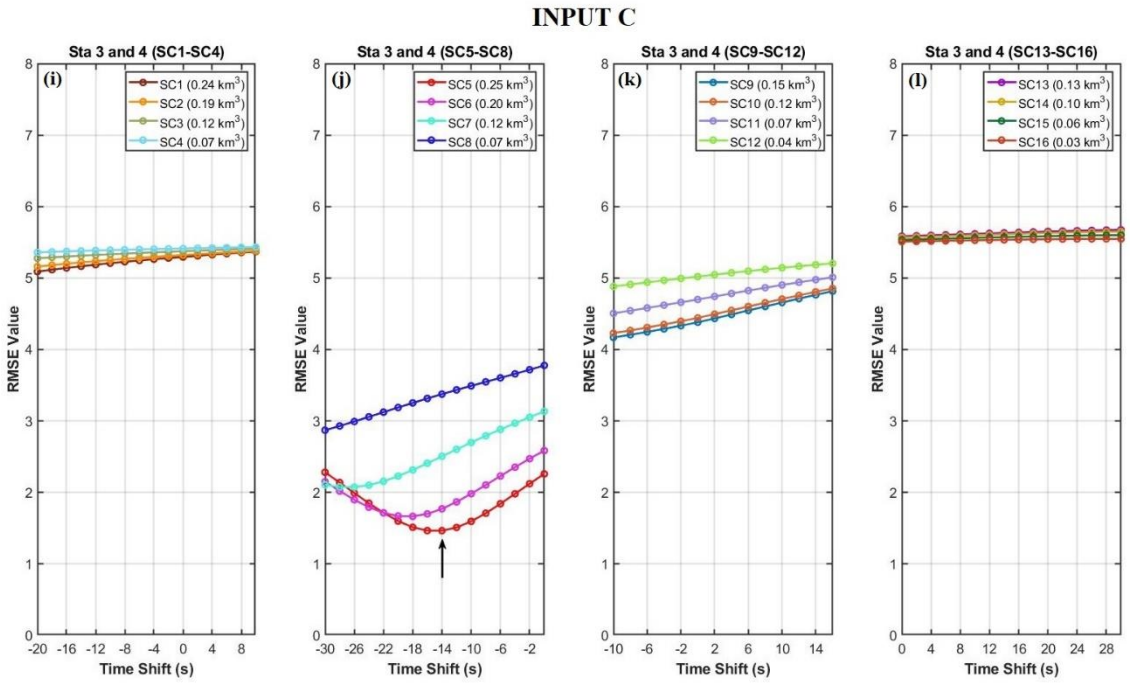

Figure 4.20 RMSE value and considerable optimal time shift for selecting initial conditions in region A, B, and C of Test Case 2. The RMSE values were calculated for all scenarios in database (SC1-SC16) at pair of station 1 & 2 for Input A **(a-d)**, station 5 & 6 for Input B **(e-h)**, and station 3 & 4 for Input C **(i-l)**. Black arrow indicates the best scenario with optimal time shift and smallest RMS misfit.

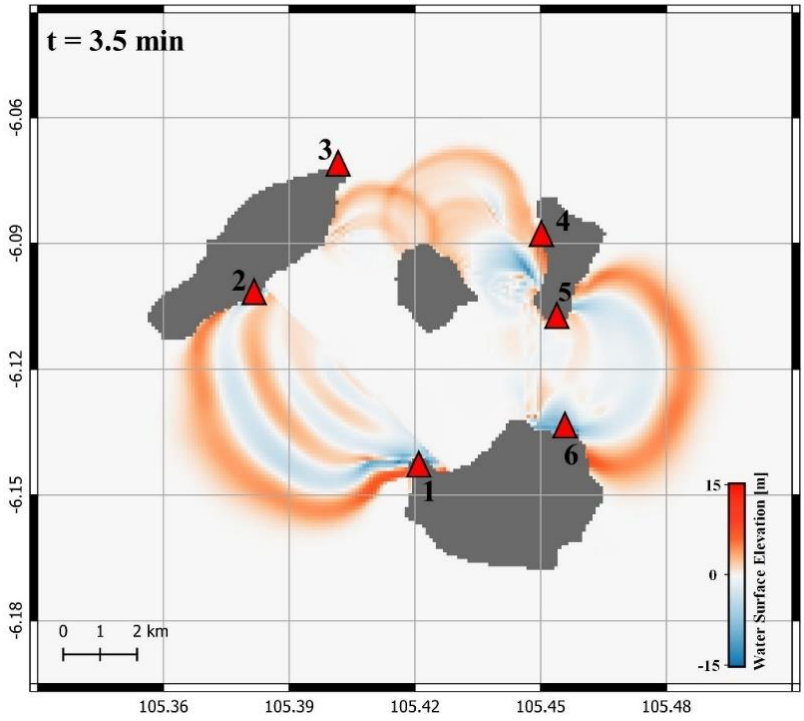

Figure 4.21 Tsunami propagation at 3.5 min using the initial condition from the best combination scenarios from the database for Test Case 2.

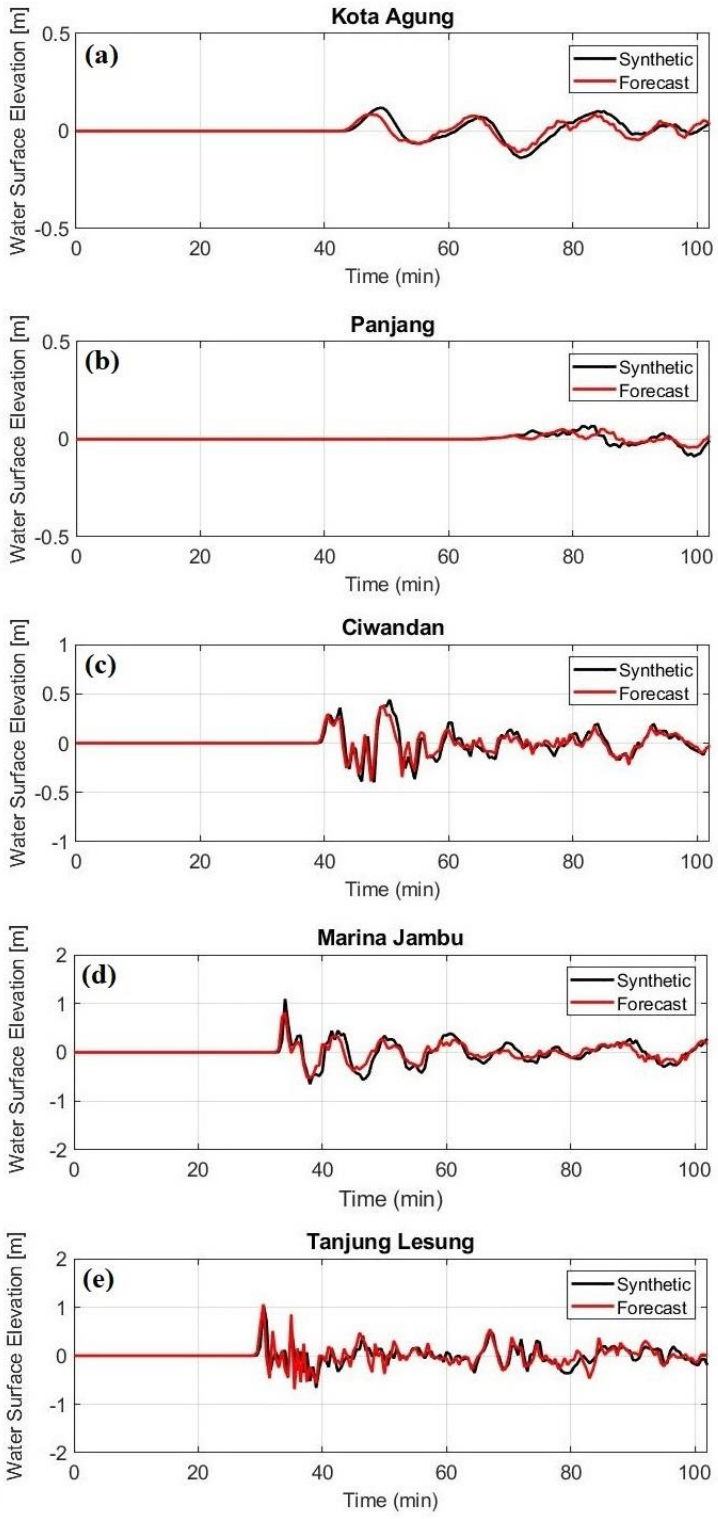

Figure 4.22 Comparison between synthetic (black) and forecasted (red) waveforms from Test Case 2 at five tide gauge locations: **(a)** Kota Agung, **(b)** Panjang, **(c)** Ciwandan, **(d)** Marina Jambu, and **(e)** Tanjung Lesung.

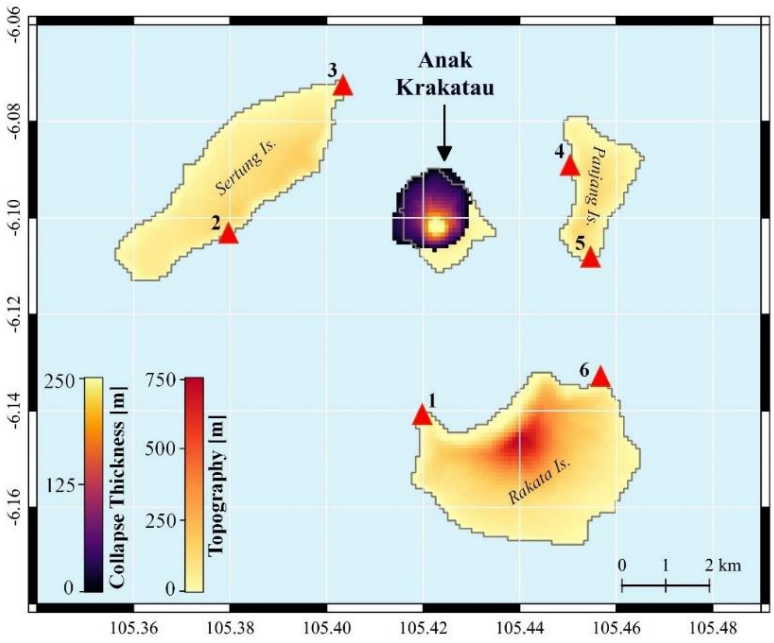

Figure 4.23. Hypothetical collapse scenario with total collapse volume of 0.20 km^3 for Test Case 3.

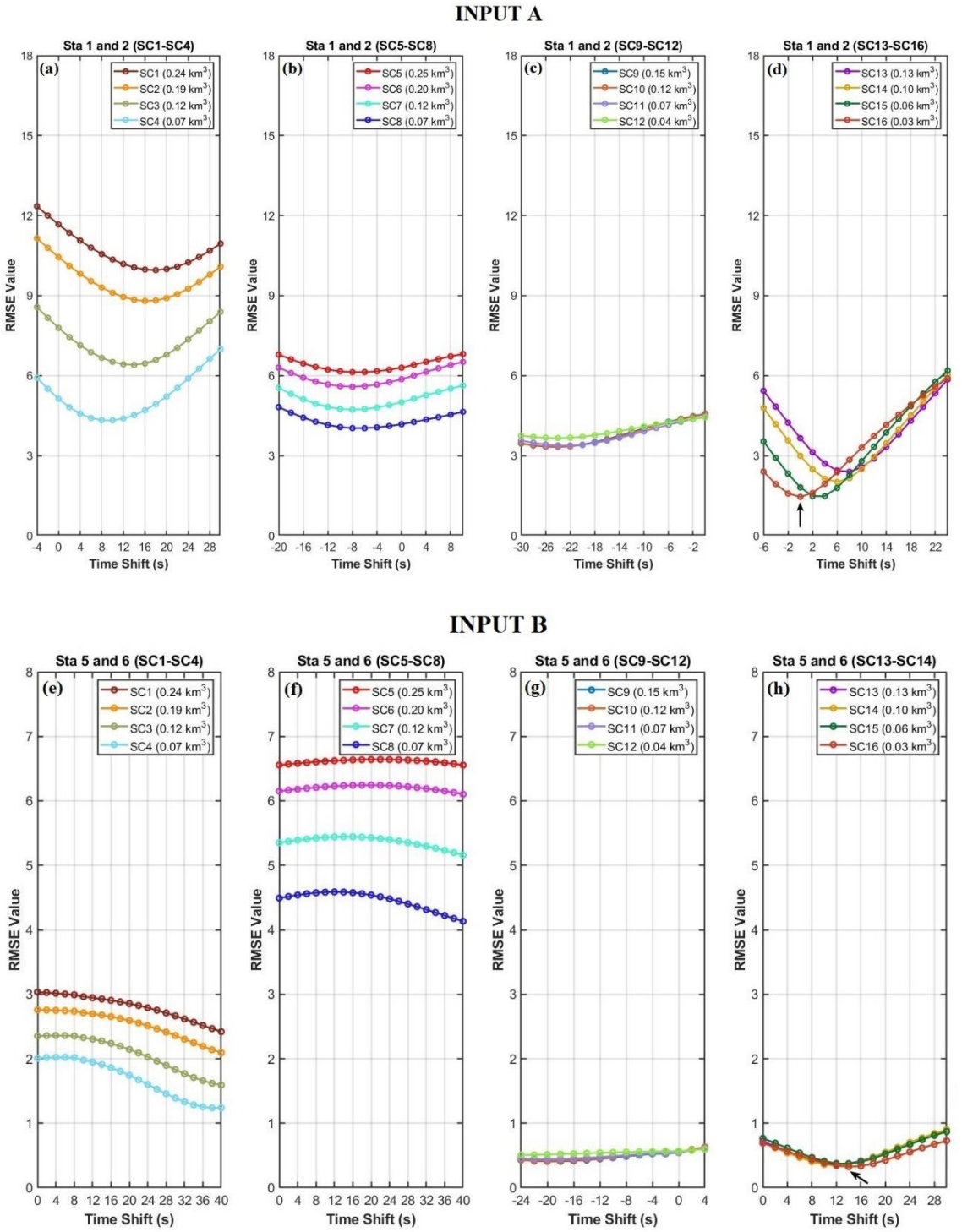
INPUT A
Sta 1 and 2 (SC1-SC4)
(a)
SC1 (0.24 km3)
SC2 (0.19 km3)
SC3 (0.12 km3)
SC4 (0.07 km3)
Sta 1 and 2 (SC5-SC8)
(b)
SC5 (0.25 km3)
SC6 (0.20 km3)
SC7 (0.12 km3)
SC8 (0.07 km3)
Sta 1 and 2 (SC9-SC12)
(c)
SC9 (0.15 km3)
SC10 (0.12 km3)
SC11 (0.07 km3)
SC12 (0.04 km3)
Sta 1 and 2 (SC13-SC16)
(d)
SC13 (0.13 km3)
SC14 (0.10 km3)
SC15 (0.06 km3)
SC16 (0.03 km3)
RMSE Value
Time Shift (s)
INPUT B
Sta 5 and 6 (SC1-SC4)
(e)
SC1 (0.24 km3)
SC2 (0.19 km3)
SC3 (0.12 km3)
SC4 (0.07 km3)
Sta 5 and 6 (SC5-SC8)
(f)
SC5 (0.25 km3)
SC6 (0.20 km3)
SC7 (0.12 km3)
SC8 (0.07 km3)
Sta 5 and 6 (SC9-SC12)
(g)
SC9 (0.15 km3)
SC10 (0.12 km3)
SC11 (0.07 km3)
SC12 (0.04 km3)
Sta 5 and 6 (SC13-SC14)
(h)
SC13 (0.13 km3)
SC14 (0.10 km3)
SC15 (0.06 km3)
SC16 (0.03 km3)
RMSE Value
Time Shift (s)

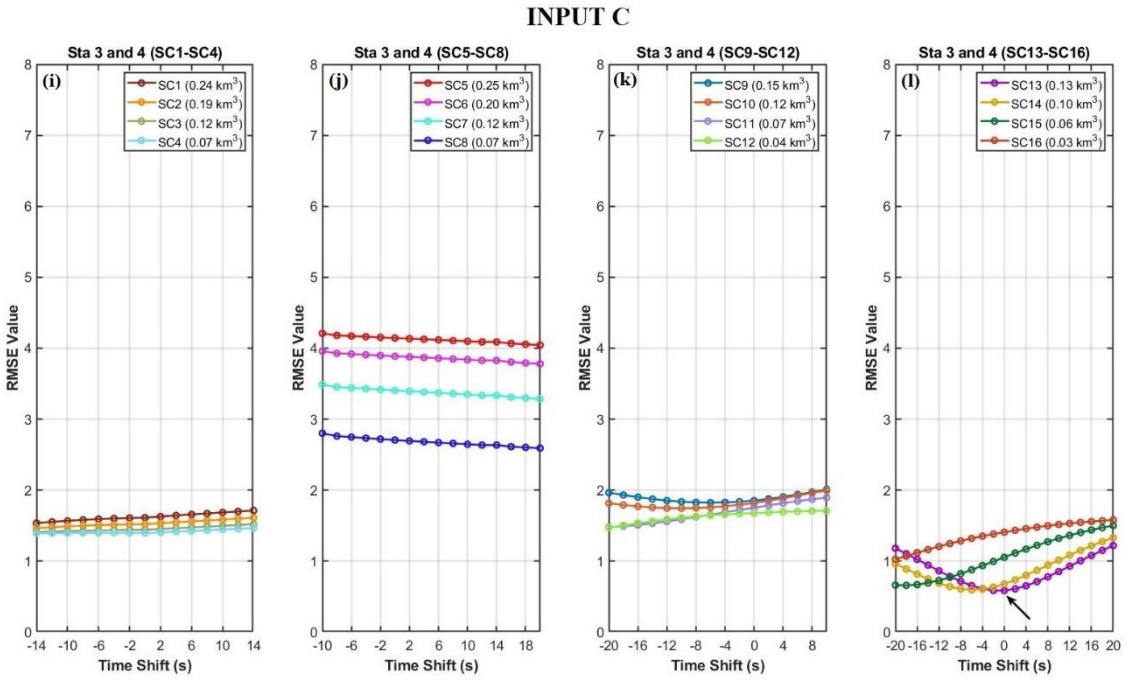

Figure 4.24 RMSE value and considerable optimal time shift for selecting initial conditions in region A, B, and C of Test Case 3. The RMSE values were calculated for all scenarios in database (SC1-SC16) at pair of station 1 & 2 for Input A **(a-d)**, station 5 & 6 for Input B **(e-h)**, and station 3 & 4 for Input C **(i-l)**. Black arrow indicates the best scenario with optimal time shift and smallest RMS misfit.

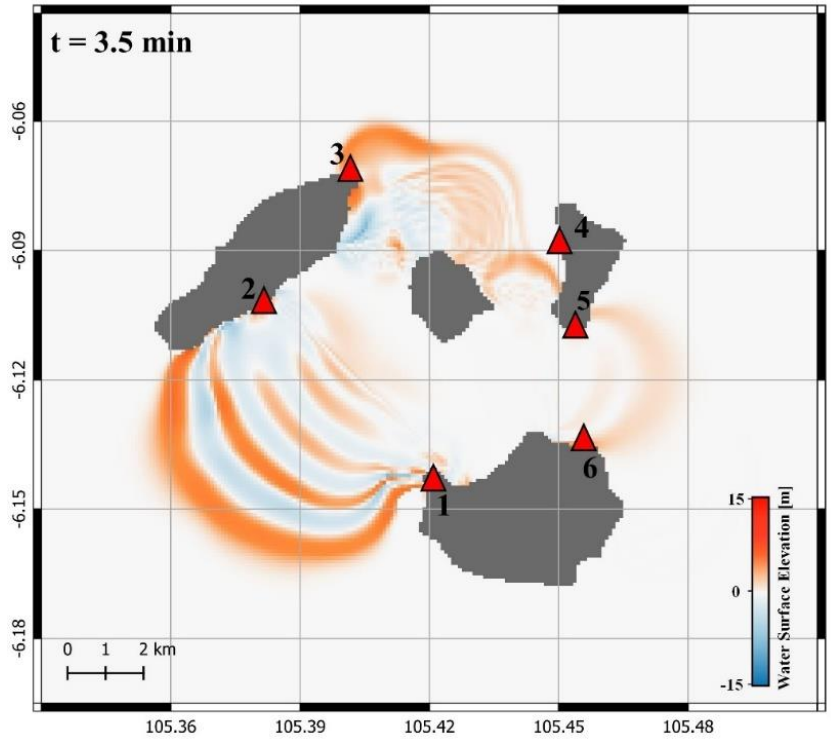

Figure 4.25 Tsunami propagation at 3.5 min using the initial condition from the best combination scenarios from the database for Test Case 3.

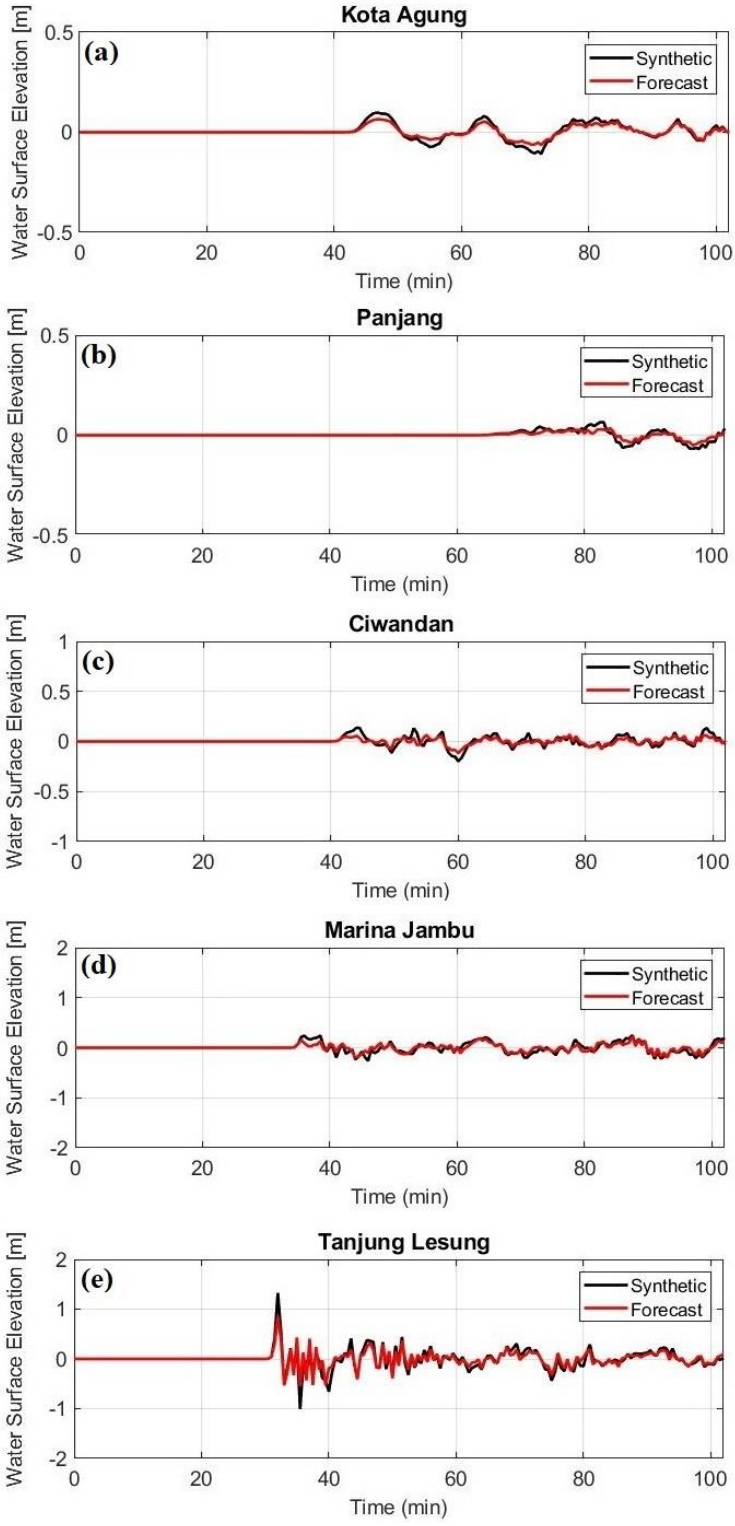

Figure 4.26 Comparison between synthetic (black) and forecasted (red) waveforms from Test Case 3 at five tide gauge locations: **(a)** Kota Agung, **(b)** Panjang, **(c)** Ciwandan, **(d)** Marina Jambu, and **(e)** Tanjung Lesung.

4.4 Discussion

We demonstrated our forecasting method through a numerical experiment using three test cases for Anak Krakatau sector collapse. In our method, we divided the Anak Krakatau complex into three regions A, B, and C, then, determined the best scenario for each region as initial conditions. As shown in the test cases, we obtained appropriate tsunami forecasts along the coast even though the collapse scenarios for the test cases were not inside the database. This method allows us to forecast the tsunami without knowing the detailed information of the collapse source.

The Sunda Strait tsunami on December 22nd, 2018, swept the nearby coastline of Java and Sumatra without any warning from either earthquake or alert system (Ye et al. 2020). Inadequate tsunami monitoring system has become one of the factors that contribute to the absence of tsunami warning in the 2018 events. Without the tsunami monitoring system, early tsunami detection and considerable tsunami forecasting will be difficult to implement. The existence of observation stations has become important as they are useful for tsunami forecasting and rapid tsunami detection. A study to investigate the forecasting performance by assimilating offshore observation data and high-frequency radar in the case of Tonga eruption was conducted by Wang et al. (2023). They tested the method that resulted in high forecast accuracy for tsunami warning. Here, we proposed a real-time forecasting method based on a pre-computed database and utilization of observation stations near the source for Anak Krakatau volcano. Our method required at least 100s of observed waveforms at six observation stations to conduct waveform fitting. A suitable observation station should then be considered in the application of our methods. Various observation networks designated for small to extremely high tsunamis are available and actively operated in Japan. Pressure sensors to

observe huge tsunamis were installed along the Japanese coasts (Tsuruoka et al. 2015). Time series of water surface level at the site where the sensor was installed can be estimated from observed pressure data. In 2011, the sensors observed the pressure changes due to the 2011 Tohoku tsunami. The corresponding water surface level changes were successfully estimated at each station although the observations were lacked in some time periods (Japan Meteorological Agency, 2012). A waveform of the tsunami with a peak height of ~ 10 m was also observed at a coastal station (Soma station). Applying this, the output value from the pressure sensor can be sent via a dedicated cable to the tide gauge converter that is placed separately in higher elevation area. Finally, the output data is transmitted via satellite to the monitoring center (Tsuruoka et al. 2015). Adopted such a pressure sensor, essential information such as initial tsunami waveforms that are needed in our method can be provided. The technical issues could be solved by identifying the best observation system that is suitable for monitoring the Anak Krakatau. In present, about two tide gauge stations are placed in the area of Anak Krakatau complex for continuously monitoring the water elevation changes. However, it is still insufficient for the implementation of real-time tsunami forecasting. More observation stations with a well-designed tsunami forecasting method should be combined to upgrade the tsunami warning system in Indonesia. The availability of tsunami observation network will be useful to detect and monitor either tsunami generated from tectonic or volcanic activity in the Anak Krakatau and Sunda Strait area.

After the 2018 tsunami event, Anak Krakatau volcano continuously showed intense volcanic activity. Considering the high volcanic activity, the topography of Anak Krakatau has changed over time. Using satellite imagery and aerial footage can be used to monitor the structural change in the Anak Krakatau. Since Anak Krakatau is

categorized as one of the most active volcanoes in Indonesia, the edifice material from the eruptive process will continue accumulating and change the morphology of Anak Krakatau from time to time. In this study, we built a pre-computed database using topography from the pre-collapse state of the 2018 Anak Krakatau tsunami to demonstrate our tsunami forecasting methods. The structure and topography of Anak Krakatau will change due to the dynamic processes such as erosion and accumulation of volcanic material. Therefore, we suggest that it is necessary to update the topography data and collapse scenario database in the implementation of this method. The frequency of updating is hard to determine since the structural change of Anak Krakatau depends on the dynamic volcanic activity over time. The quality of the topography data possibly affects the accuracy of tsunami forecasting. Recent topography data with good resolution should be obtained before implementing the forecasting method in our study. Moreover, a good quality of bathymetry data around Sunda Strait should be available for the numerical simulation. According to our analysis from the numerical simulation of the 2018 Sunda Strait tsunami, discrepancies and inaccuracy of numerical simulation may arise due to insufficient topography and bathymetry data. Therefore, reliable topographic and bathymetric data from the surface mapping or more detailed geophysical imaging are necessary to conduct. The number of scenarios in the database should be considered as another important factor. In the present study, we created 16 collapse scenarios with various volumes and collapse areas for the demonstration of our real-time forecasting method. A higher accuracy of tsunami forecasting can be achieved by increasing the number of collapse scenarios in the database. However, large numbers of scenarios may consume more time in the selection process of initial conditions for the real-time simulation. In the implementation of this method, it is important to find the optimal

number of collapse scenarios in the database as the Anak Krakatau volcano grows rapidly over time.

The tsunami generation and propagation models in this study were carefully tested by performing a numerical simulation of the 2018 Anak Krakatau tsunami and were validated with observed waveforms at four tide gauge stations and tsunami measurements from the field survey. For future disaster mitigation strategies, we propose a real-time tsunami forecasting method based on the pre-computed database for the Anak Krakatau volcanic tsunamis in Indonesia. Numerical experiments for the three test cases showed that our method could efficiently produce appropriate tsunami forecasts in the vicinity of the Sunda Strait. Moreover, by implementing our method, we can estimate real-time tsunamis generated by volcanic activity of Anak Krakatau without information on complex source mechanisms.

Systematic tsunami warning and forecasting method for sector collapse of Anak Krakatau have been proposed in this study. However, further improvements should be made to the application of this tsunami warning system. Volcanic eruptions may induce pyroclastic flows, explosion, subaerial collapse, and submarine landslides, which all could give contribution to the tsunami generation. The current forecasting method proposed in this study was based on the pre-computed database that constructed considering sector collapse scenario only. Inadequate variation of source mechanisms in the database can cause less accuracy of forecasting tsunamis. Therefore, a pre-computed database considering various source mechanisms should be considered as future improvements of this study. Our forecasting method requires time to obtain initial conditions for real-time tsunami forecasting. With a larger number of scenarios in database, it may consume more time to obtain the best combination of scenarios as input

for simulation. A designed system should be created to speed up the process of searching for the best scenario. In actual implementation, warning time should be one of the most important component of tsunami warning and forecasting. Our method requires real-time simulation to provide information about tsunami impact to the coastal area. Advanced devices should be prepared to perform faster simulation to forecast the tsunami. Higher resolution of topography and bathymetry data is also required to provide more accurate tsunami forecast to the targeted area.

Chapter 5

Study on the Tsunami Generation by Sector Collapse of Komagatake Volcano for Future Tsunami Warning System

5.1 The 1640 Komagatake Tsunami

On July 31st, 1640, the summit of Mt. Komagatake collapsed due to volcanic activity and caused a large tsunami known as Komagatake tsunami. Part of the avalanche collapsed to the eastward from the summit of Komagatake and then entered the sea causing a large tsunami (Nishimura et al. 1999). Tsunami generated by collapse of Komagatake volcano in 1640 washed over the coast of Uchiura bay and killing about 700 people (Katsui and Yamamoto, 1981; Furukawa et al. 2008; Nakanishi and Okamura, 2019). Komagatake is a conical stratovolcano located in the southwest part of Hokkaido, Japan (Fig. 5.1). The summit of Komagatake has a horseshoe-shaped crater with approximately 2 km diameter. The tsunami traces from the 1640 event were confirmed by tsunami deposits data consisting of gravel to sand layer covered with Komagatake d (Ko-d) tephra from the 1640 eruption in several locations along Uchiura Bay (Nishimura and Miyaji, 1998). Survey conducted by Yoshimoto et al. (2003) using side scan sonar shows that debris avalanche from the 1640 eruption was deposited 80 m deep seafloor and deposited to the eastward and northeast of volcano. Total collapse volume with range of 0.92 to 1.20 km^3 was estimated by extrapolating the pre-collapse topography from the surrounding area (Yoshimoto et al. 2003). Moreover, information about the tsunami height from the 1640 Komagatake tsunami was also available from the measurement along the southern coast of Iburi to Uchiura Bay, maximum run up heights of 2.9 m, 8.5 m, 7.3 m, 4.5 m, and 5.8 m were recorded at Shadai, Zenko-ji, Arutori, Kogane, and

Washinoki, respectively (Nishimura and Miyaji, 1995; Nishimura et al. 1998). Also, the information about the tsunami deposit from the 1640 Komagatake tsunami is available from several studies including Nakanishi and Okamura, (2019). After the 1640 eruption, several noticeable eruptions occurred in the years 1694, 1856, and 1929 with Plinian eruption style. At this moment, the activity of Komagatake is continuously monitored by the authorities including Japan Meteorological Agency.

5.2 Numerical Simulation of the 1640 Komagatake Tsunami

In this study, a preliminary modeling of the 1640 Komagatake tsunamis is conducted to test the reliability of landslide and tsunami models. The numerical simulation of landslide and tsunami of Komagatake is mainly performed using the coupled models of VolcFlow (Kelfoun and Druitt, 2005; Kelfoun et. al. 2011) and Boussinesq models (Yamanaka and Tanioka, 2017). The generation and propagation of tsunami from the landslide is modeled using combination of those two models in a similar manner with the preliminary modeling of the 2018 Sunda Strait tsunami event. Slightly different from previous simulation of Anak Krakatau, the initial generation of landslide and tsunami is performed for 3-min using VolcFlow model then later computation will take over by only Boussinesq model for another 120-min simulation. Considering the larger collapse volume of Komagatake, the early stage of simulation by VolcFlow model was set to 3 minutes to anticipate the prolonged landslide-water simulation. In this computation, a set of topography and bathymetry data with resolution of 150 m was applied for the entire computation domain. The simulation results from preliminary modeling of the 1640 Komagatake tsunami will be compared with available historical tsunami data including run-up height and tsunami deposit.

In the numerical simulation of the 1640 Komagatake tsunami, an initial collapse volume of 1.2 km^3 based on the study of Yamanaka and Tanioka (2017) was employed as an initial condition for the simulation. The initial collapse and the elevation profile from before and after the 1640 collapse is indicated in Fig. 5.2 and the collapse thickness from first 3 minutes simulation is shown in Fig. 5.3. Based on the simulation, in 3 min the center of the mass collapsed from towards the eastern part of Komagatake volcano. The deposit was scattered in a large area underwater mainly to the eastern part of volcano. Further result of tsunami propagation simulation is shown in Fig. 5.4. In the first 3 min, the collapse generated tsunami with initial height more than 35 m then propagating towards all directions (Fig. 5.4a). Approximately 20 min after the initial collapse, the tsunami arrived at the location across the volcano in loc D (Kogane) (Fig. 5.4b). Then after 100 min, the tsunami completely inundated the large coastal area along Uchiura Bay in the southern part of Iburi coast (Fig. 5.4d). Furthermore, the simulation was evaluated by comparing the simulated tsunami with the available tsunami data of maximum run-up heights (Nishimura and Miyaji, 1998) and tsunami deposit data (Nakanishi and Okamura, 2019). The inundation simulation from this study was compared with the distribution of tsunami deposits data of the 1640 Komagatake found at seven places along Hokkaido coast (Fig. 5.5). Then, a comparison between measured and simulated tsunami run-up heights at five locations is presented in Fig. 5.6. Based on comparison, the tsunami deposits distribution at seven places were generally well-explained by our numerical simulations (Fig. 5.5). However, the comparison with measured run-up height at five places shows that there are discrepancies between the observed and simulated tsunami height indicated by overestimation and underestimations (Fig. 5.6). The underestimations were found especially at the location of B (Zenko-ji), C (Arutori), E (Washinoki), that

located along Uchiura Bay. Similar discrepancies between measured and simulated tsunami height at five locations were also found in the study of Yamanaka and Tanioka (2017) who performed the numerical simulation using different landslide model. Further investigation into the discrepancies in the simulation especially at the locations along Uchiura Bay (location B, C, E) was conducted by employing larger collapse volume from the initial collapse volume we used before. Two larger collapse volumes of 1.8 km^3 and 2.4 km^3 were created by increasing the collapse thickness by 1.5 times and 2.0 times ratio from 1.2 km^3 initial volume, respectively. Landslide and tsunami simulation were computed again using two larger collapse volumes. The comparison of measured and simulated run-up heights using variation of collapse volumes is presented in Fig. 5.7. Snapshots of tsunami propagation resulted from increased volume variations of 1.8 km^3 and 2.4 km^3 were shown in Fig. 5.8 and 5.9 respectively. Comparing the results, the measured run-up height at location C (Arutori) and E (Washinoki) were explained better using two increased volume variations (Fig. 5.7). However, the measured run-up height at location B (Zenko-ji) still could not explained well by the collapse volume variations. The inundation simulation comparison in the locations of B (Zenkoji) and Arutori (C) from three different collapse volumes of 1.2 km^3, 1.8 km^3, and 2.4 km^3 is presented in Fig. 5.10. As result, the increased volumes resulted in larger inundation at Zenkoji (B), but the measured tsunami still could not explain well by those collapse volume variations. It is possibly due to the coarse resolution of topography and bathymetry data used in the simulation. The collapse deposits from the 1640 Komagatake tsunami were distributed to the northeast and east parts of Komagatake based on the study of Yoshimoto et al. (2003). The collapse thickness of the landslide from three different volumes of 1.2 km^3, 1.8 km^3, and 2.4 km^3 were compared to the collapse depositional area from the survey by

Yoshimoto et al. (2003) (Fig. 5.11). The comparison shows that initial volume of 1.8 km^3 and 2.4 km^3 explained well both the observed tsunami heights (Nishimura and Miyaji, 1998) and the depositional area from the field survey of Yoshimoto et al. (2003).

5.3 Tsunami Characteristics and Hazard Assessment

Further study on the tsunami characteristic and hazard assessment from the sector collapse of Komagatake volcano is conducted by simulating hypothetical collapse scenarios assuming the future collapse of Komagatake. The hypothetical collapse scenarios are carefully created using the present topography data. Assuming the future collapse cases, this study created three hypothetical collapse scenarios using the same method as applied in the construction of pre-computed database for sector collapse of Anak Krakatau in the previous chapter. Furthermore, three virtual observation stations were placed to the vicinity of volcano to identify the characteristics of tsunami from the sector collapse of Komagatake (Fig. 5.14).

5.3.1 Hypothetical Collapse Scenario 1

The first hypothetical collapse has a total collapse of 0.87 km^3 with the main collapse plane located to the northeast part of Komagatake volcano (Fig. 5.12). Using the hypothetical collapse scenario, the simulation of landslide and tsunami was then conducted based on the same manner with the preliminary modeling of the 1640 Komagatake event by sequence of VolcFlow and Boussinesq models. The landslide thickness from 3 minutes simulation is shown in Fig. 5.13. At the first 3-min simulation, it is shown that the collapse materials were widely distributed towards the north, northeast, and eastern part of Komagatake volcano (Fig. 5.13d). Then, the snapshot of tsunami propagation simulation at 5, 10, 20, and 100 min from the initial collapse using hypothetical collapse scenario 1 are shown in Fig. 5.14. Assessment on the tsunami hazard

was conducted by extracting the maximum tsunami height at four locations (Yakumo, Oshamanbe, Date, and Muroran) indicated by red triangles in Fig. 5.14. As result, the hypothetical collapse scenario 1 with main collapse plane located at the northeast part of Komagatake volcano produced significant tsunami at the area across volcano especially Muroran and Date area with maximum tsunami height of 15.1 m and 10.1 m, respectively (Fig. 5.14d). The characteristics of tsunami generated by hypothetical collapse scenario 1 were further assessed using the extracted waveforms at three virtual observation stations (Fig. 5.15). By comparing the extracted waveforms, virtual observation stations 2 located to the northeast of volcano observed the highest tsunami elevation compared to the other two stations. The first hypothetical collapse scenario has a main collapse plane in the northeast part of volcano and resulting in a highest observed tsunami amplitude at station located also to the northeast of volcano. The highest recorded waveforms at observation stations correspond to the main collapse plane and collapse direction. A single collapse scenario might be not enough to identify the characteristics of tsunami resulting from the sector collapse of Komagatake. Therefore, another collapse scenarios with different volumes and main collapse locations are needed to give more detailed information about tsunami characteristics.

5.3.2 Hypothetical Collapse Scenario 2

The second hypothetical collapse was created using different collapse geometry with the main collapse plane located at the north part of volcano (Fig. 5.16). Considering the variety of landslides, another scenario with total collapse volume of 0.63 km^3 is employed to the numerical simulation as initial source. Numerical simulation was conducted using the same manner as previous simulation in scenario 1. The landslide thickness from 3-min simulation is shown in Fig. 5.17. From 3 minutes landslide

simulation, the hypothetical collapse scenario 2 resulted in a relatively wide collapse deposit area (Fig. 5.17d). The snapshot of tsunami propagation simulation at 5, 10, 20, and 100 min from the initial collapse using hypothetical collapse 2 is indicated in Fig. 5.18. The impact of tsunami to the coastal area of Hokkaido was conducted by examining the maximum tsunami height at four places. Similar with previous collapse scenario, the numerical simulation of landslide and tsunami from the hypothetical collapse 2 resulted in the significant height at the area around Muroran and Date with maximum tsunami height of 13.1 m and 9.1 m, respectively (Fig. 5.18d). Furthermore, the extracted waveforms at three virtual observation stations were used to identify the tsunami characteristic from the hypothetical collapse scenario 2. As comparison from extracted waveforms at three virtual stations, it shows that the collapse plane in the north part of volcano resulting in significant tsunami height recorded at virtual observation 1 and 2 located at the northwest and northeast of volcano with highest tsunami amplitude recorded at virtual observation 2 (Fig. 5.19).

5.3.3 Hypothetical Collapse Scenario 3

The last hypothetical scenario involved a scenario with total collapse volume of 0.72 km^3 with main collapse plane located at the northwest area of Komagatake (Fig. 5.20). Numerical simulation was conducted in the same manner with the previous two scenarios using combination of VolcFlow and Boussinesq models. In this last hypothetical scenarios, landslide thickness shows that the collapse is widely distributed towards northwest, north, and northeast side of Komagatake volcano, which is similar characteristic with the previous two collapse scenarios (Fig. 5.21). From this scenario, large collapse deposits were mainly accumulated in northwest to the north of volcano. The snapshots of tsunami propagation are shown in Fig. 5.22. The hypothetical collapse

scenario 3 with main collapse located at the northwest area of volcano resulted in the significant tsunami height in Date and Muroran areas (Fig. 5.22d), which indicates similar tsunami distribution pattern with previous two collapse scenarios. The waveforms identification at three virtual observation stations shows that the highest tsunami amplitude appears in virtual observation 1 (Fig. 5.23). The hypothetical collapse scenario 3 has a main collapse plane to the northeast part of volcano and resulting in a highest observed tsunami amplitude at virtual station 1 located to the northeast of volcano. This result indicates that the recorded waveforms at virtual observation stations can give primary information about the main collapse plane and collapse direction. The result from the waveforms analysis here highlights that important information related to the initial collapse and generated tsunami waves from the sector collapse can be identified from the waveforms at observation stations. This can be one of the advantages from the existence of observation stations in the vicinity of volcano towards the development of tsunami warning.

5.4 Discussion

Study on the tsunami generation by sector collapse of Komagatake was conducted by preliminary modeling of the 1640 Komagatake tsunami event and numerically computed three hypothetical collapse scenarios assuming the future collapse of Komagatake. The simulation of the 1640 Komagatake was assessed by the available tsunami data including tsunami deposit and tsunami height measurement along the coast of Hokkaido. Higher collapse volumes of 1.8 and 2.4 km^3 explained well the tsunami deposits and tsunami height from the field survey. The survey of Yoshimoto et al. (2003) explained that total debris volume that flowed to the sea is estimated to be 0.92 to 1.20 km^3, while the amount of collapse deposit in the land is about 0.50 km^3. Considering total

collapse deposit inland and sea area, the collapse volumes estimation of 1.8-2.4 km^3 suggested in this study is consistent with the total collapse volume from the surveyed data. This study suggested that the initial collapse volume of 1.8-2.4 km^3 should be appropriate for simulating the 1640 Komagatake tsunami event.

Further analysis on the characteristics of tsunami resulting from the sector collapse of Komagatake and its impact to the coastal area were investigated by simulating three hypothetical collapse scenarios. The hypothetical collapse scenarios with different initial collapse and volumes were employed to the numerical models assuming the future collapse of Komagatake. Based on the simulations using three hypothetical scenarios, the landslides resulted in similar tsunami height distribution pattern along Uchiura Bay. All three hypothetical scenarios resulted in larger tsunami heights around Date and Muroran, while smaller tsunami heights were found around Yakumo and Oshamanbe area (Fig. 5.24). The topography and bathymetry profile along Uchiura Bay are possibly responsible for those similar tsunami distribution patterns. Through this analysis we know that the tsunami distribution pattern along Uchiura Bay was likely similar regardless of the landslide direction. This suggests that the tsunami heights along Uchiura Bay should be well predicted using the amplitudes of three virtual stations which are influenced by collapse volume. However, there are still minor variations of tsunami height distribution along Uchiura Bay. Those variations can also be predicted by analyzing approximately 5-10 minutes waveforms observed at virtual observation stations. The variations in tsunami height can be identified by looking at amplitude differences from the observed waveforms at virtual stations. Based on our numerical simulations, tsunami arrival time from the sector collapse of Komagatake are varied from 16-26 minutes after the initial collapse at location along Uchiura Bay. Therefore, using the information from 5-10 minutes

waveforms at observation station, we still can obtain warning time of 10-15 minutes for coastal area across the volcano especially in Uchiura Bay. By conducting numerical experiments using three hypothetical scenarios, this study showed the existence of observation stations should be beneficial for tsunami warning and forecasting purposes. Tsunami warning and forecasting for sector collapse case of Komagatake have not fully constructed in this study. The result in this study mainly provides insight for the importance of observation stations to identify the collapse sources and early tsunami detection. Careful consideration should be given to the construction of tsunami warning for sector collapse of Komagatake.

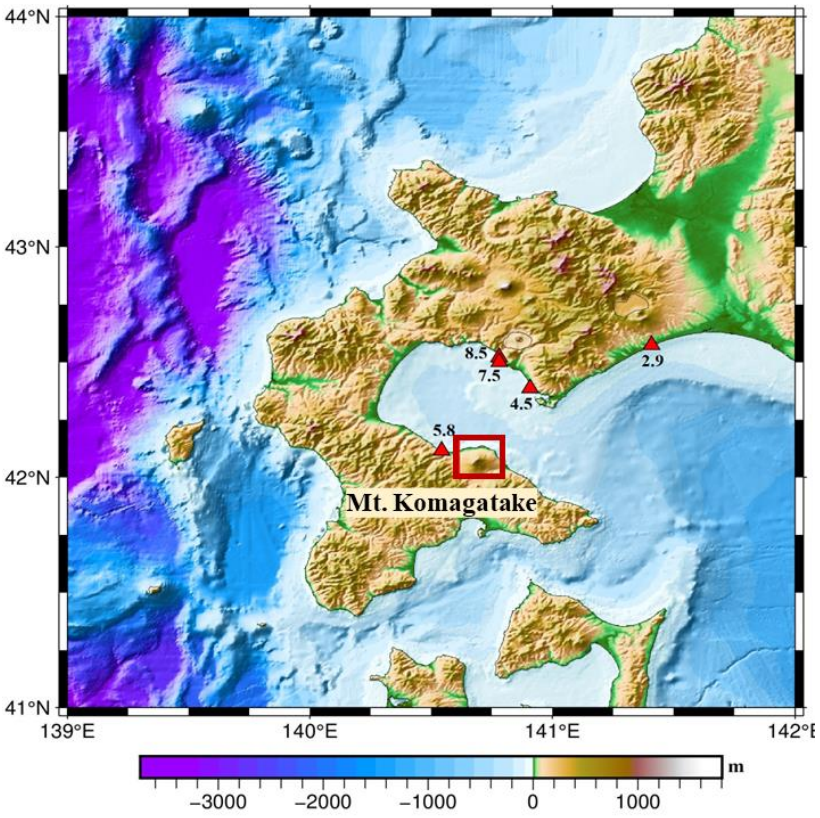

Figure 5.1 Komagatake volcano location indicates by red rectangle.

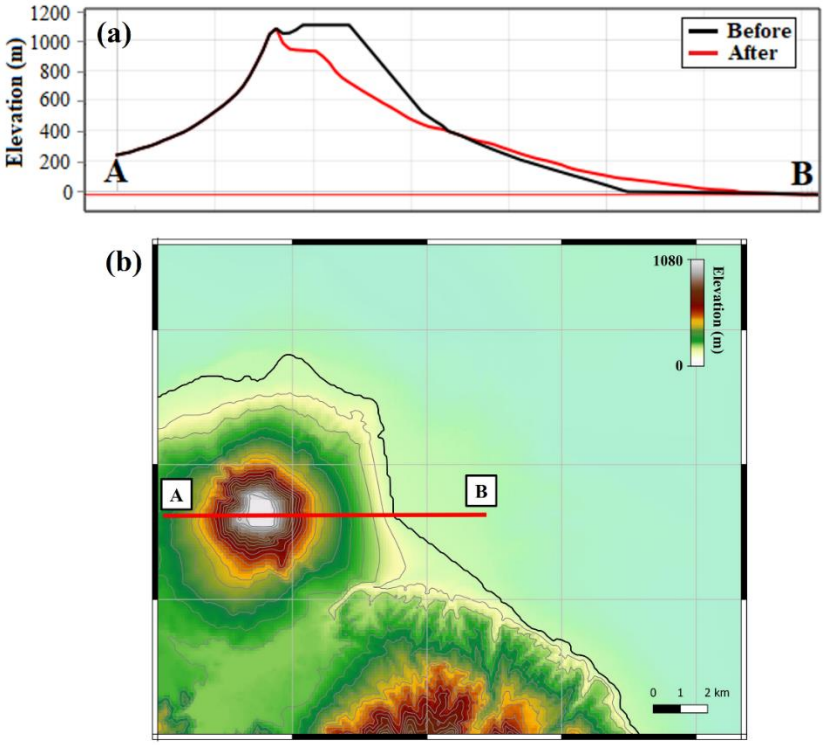

Figure 5.2 Elevation profile of Komagatake from before and after the collapse in 1640.

(a) Elevation profile from the cross-section A-B indicated in (b).

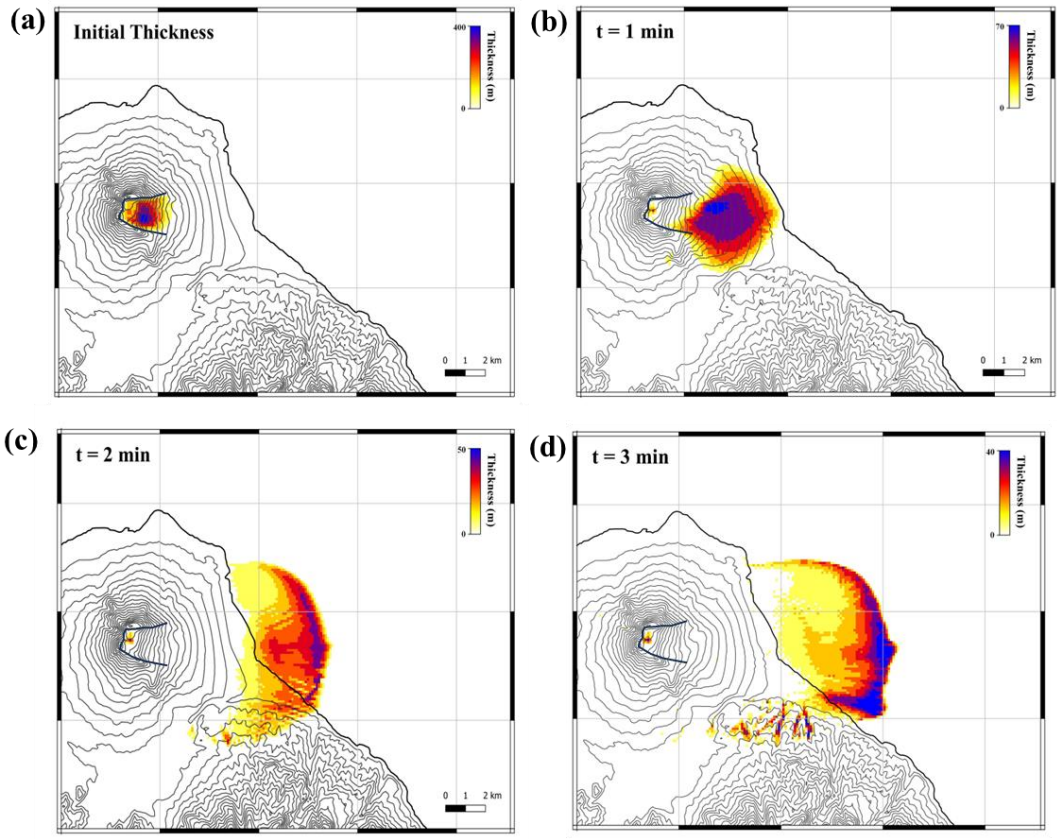

Figure 5.3 Collapse thickness of the 1640 Komagatake event in 3-min simulation using initial collapse of 1.2 km^3.

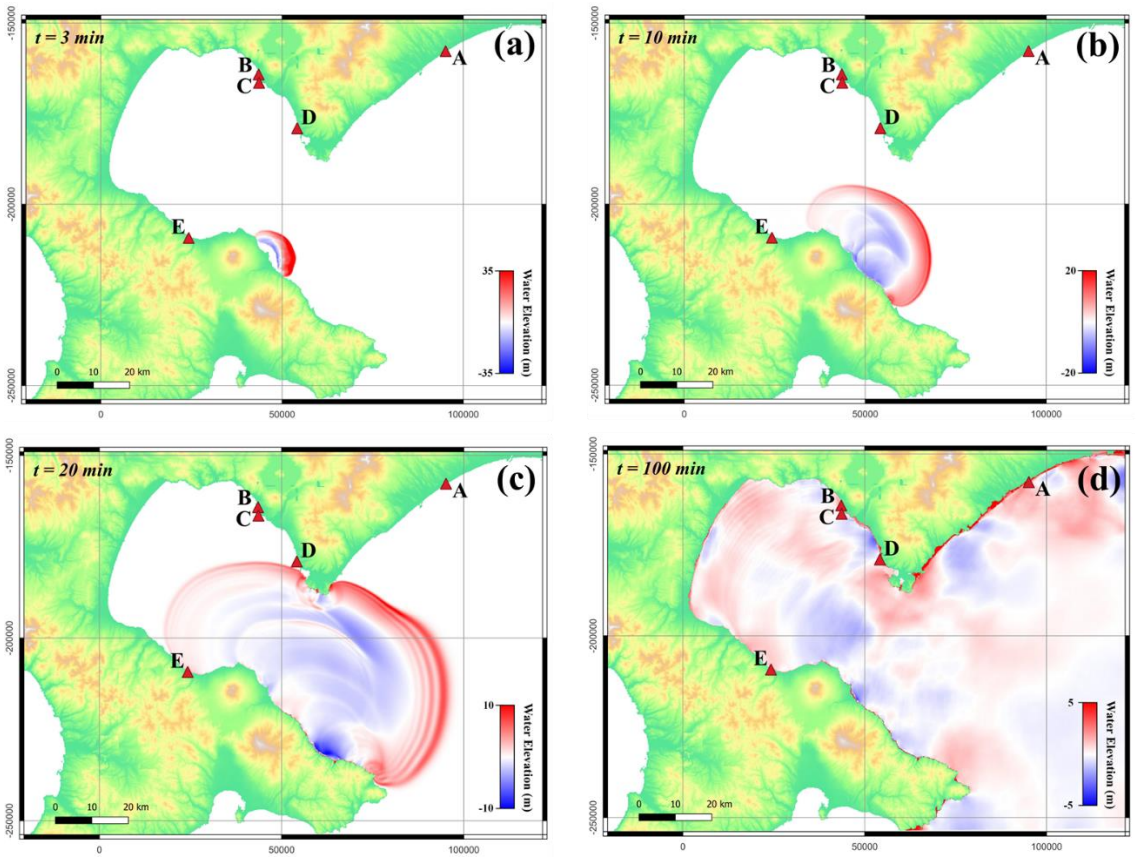

Figure 5.4 Snapshots of tsunami propagation simulation from the 1640 Komagatake tsunami using initial collapse volume of 1.2 km^3. Tsunami measurement points indicate by red triangles at A (Shadai), B (Zenkoji), C (Arutori), D (Kogane), E (Washinoki).

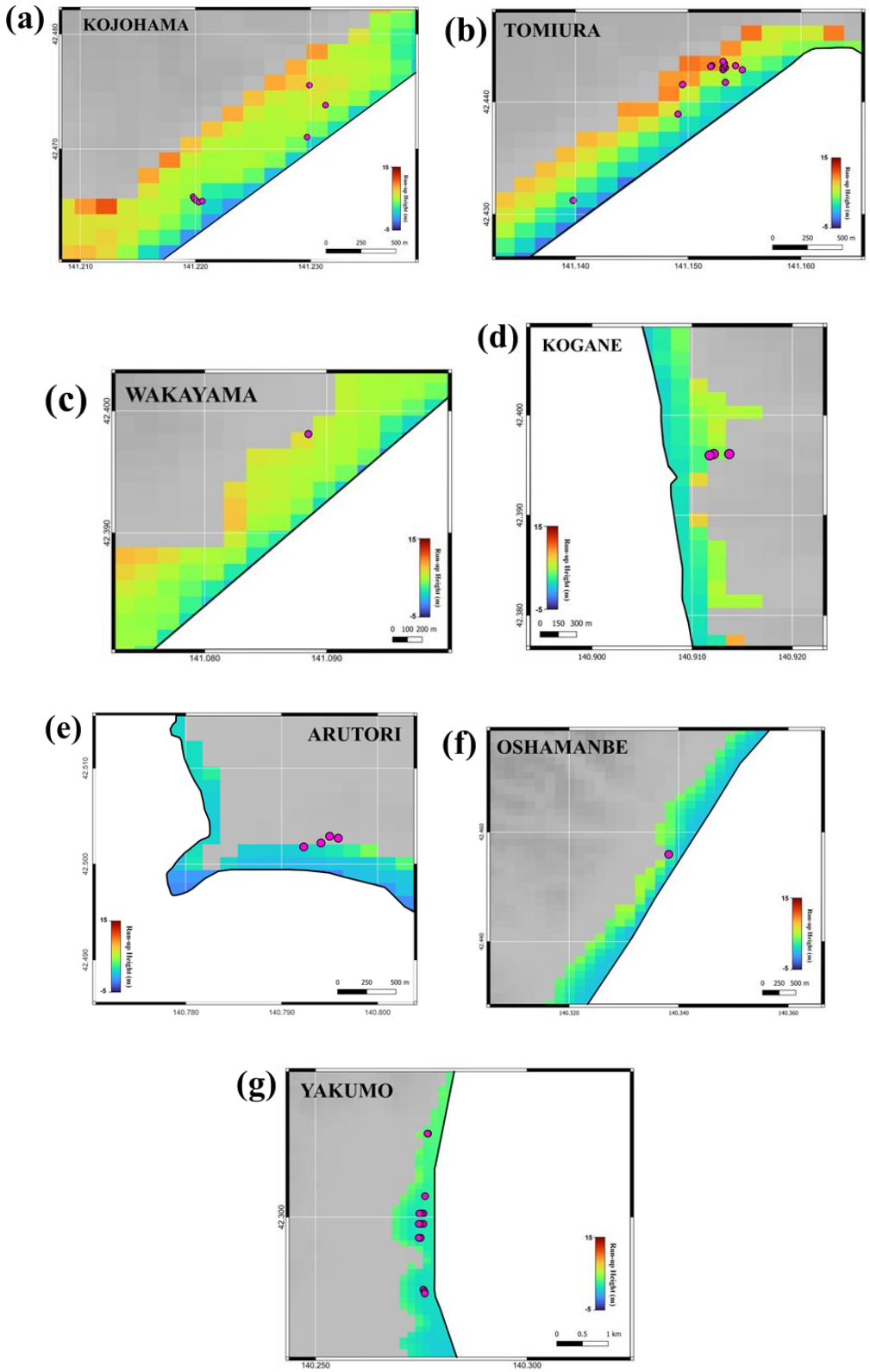

Figure 5.5 Tsunami inundation simulation at seven locations and considerable tsunami deposits from the 1640 Komagatake tsunami indicated by magenta circles.

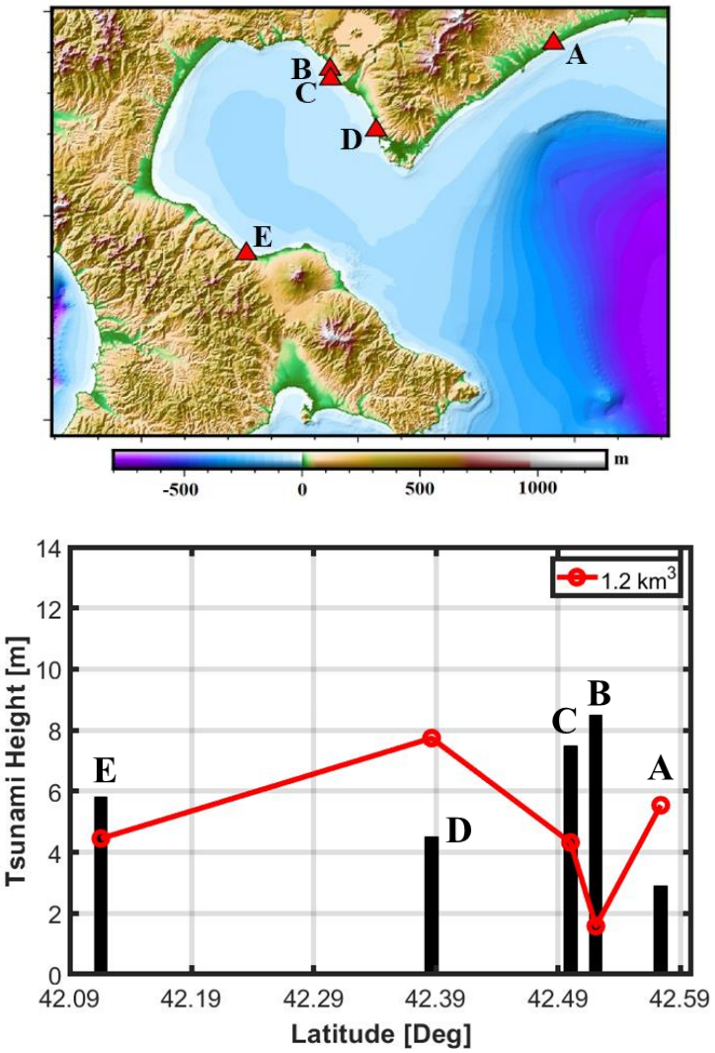

Figure 5.6 Comparison between measured (black bar) and simulated (red line) run-up heights at five locations of A (Shadai), B (Zenko-ji), C (Arutori), D (Kogane), and E (Washinoki).

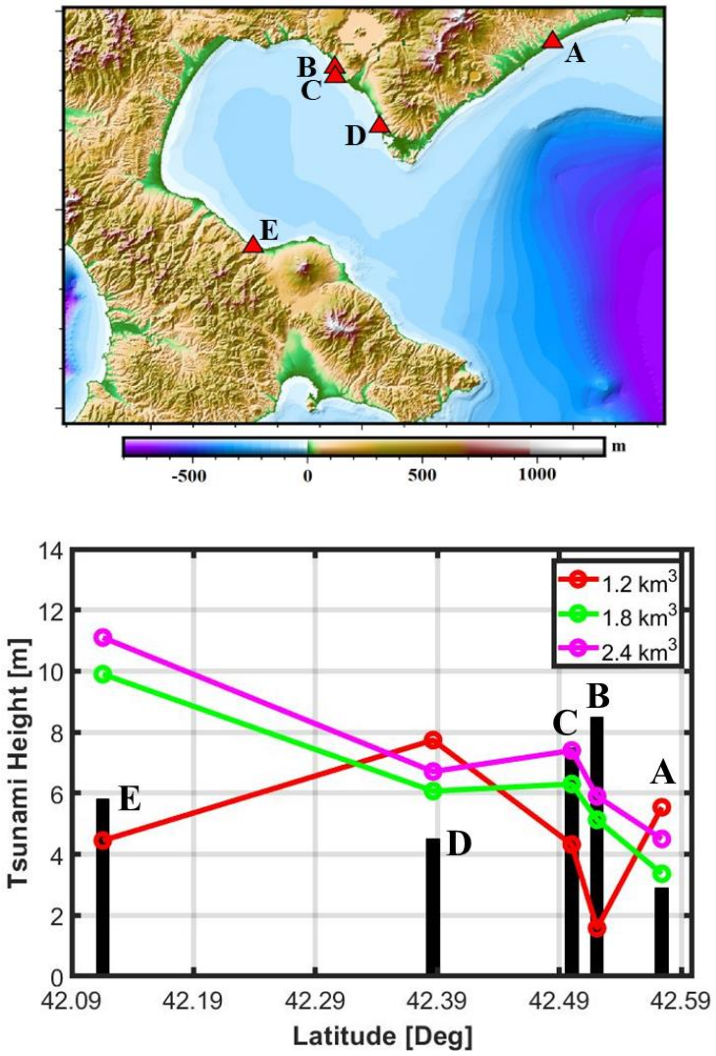

Figure 5.7 Comparison between measured (black bar) and simulated run-up height at five locations with collapse volume variations of 1.2 km^3 (red line), 1.8 km^3 (green line), 2.4 km^3 (magenta line).

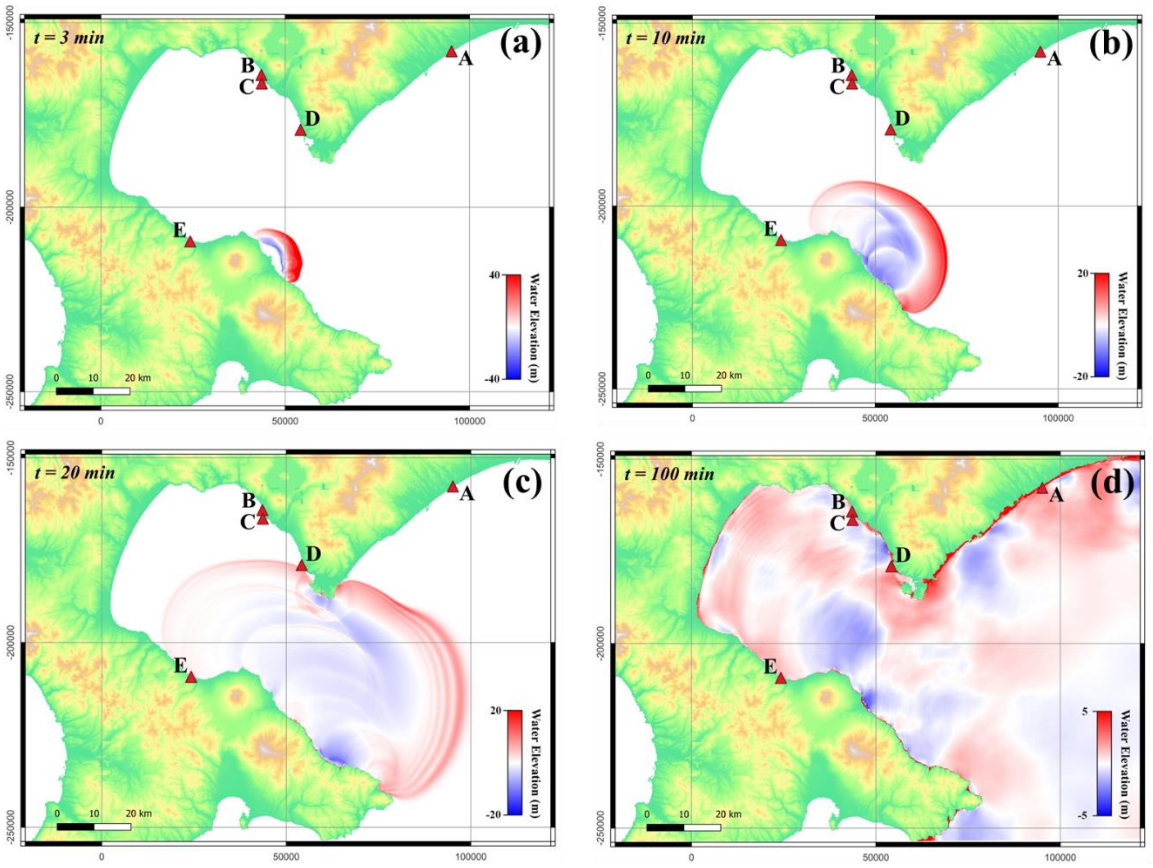

Figure 5.8 Snapshots of tsunami propagation simulation from the 1640 Komagatake tsunami using increased initial collapse volume of ***1.8 km^3***.

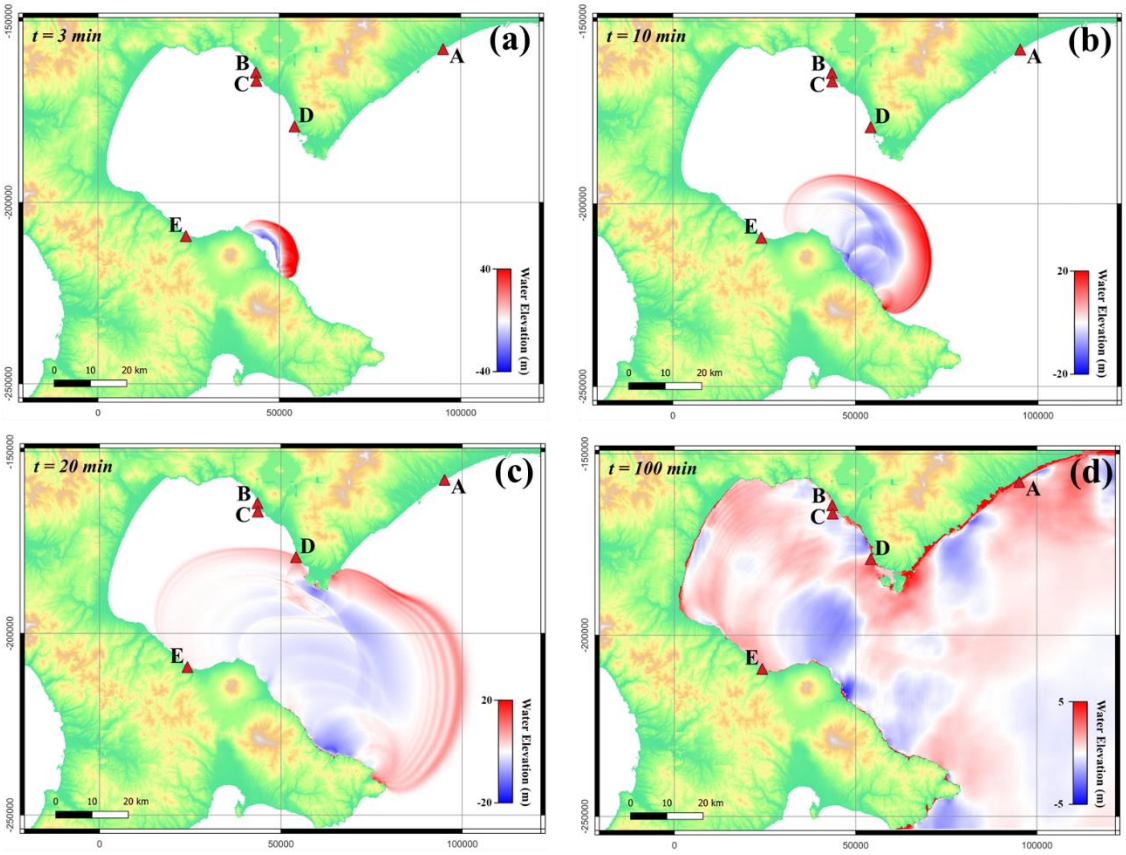

Figure 5.9 Snapshots of tsunami propagation simulation from the 1640 Komagatake tsunami using increased initial collapse volume of ***2.4 km^3***.

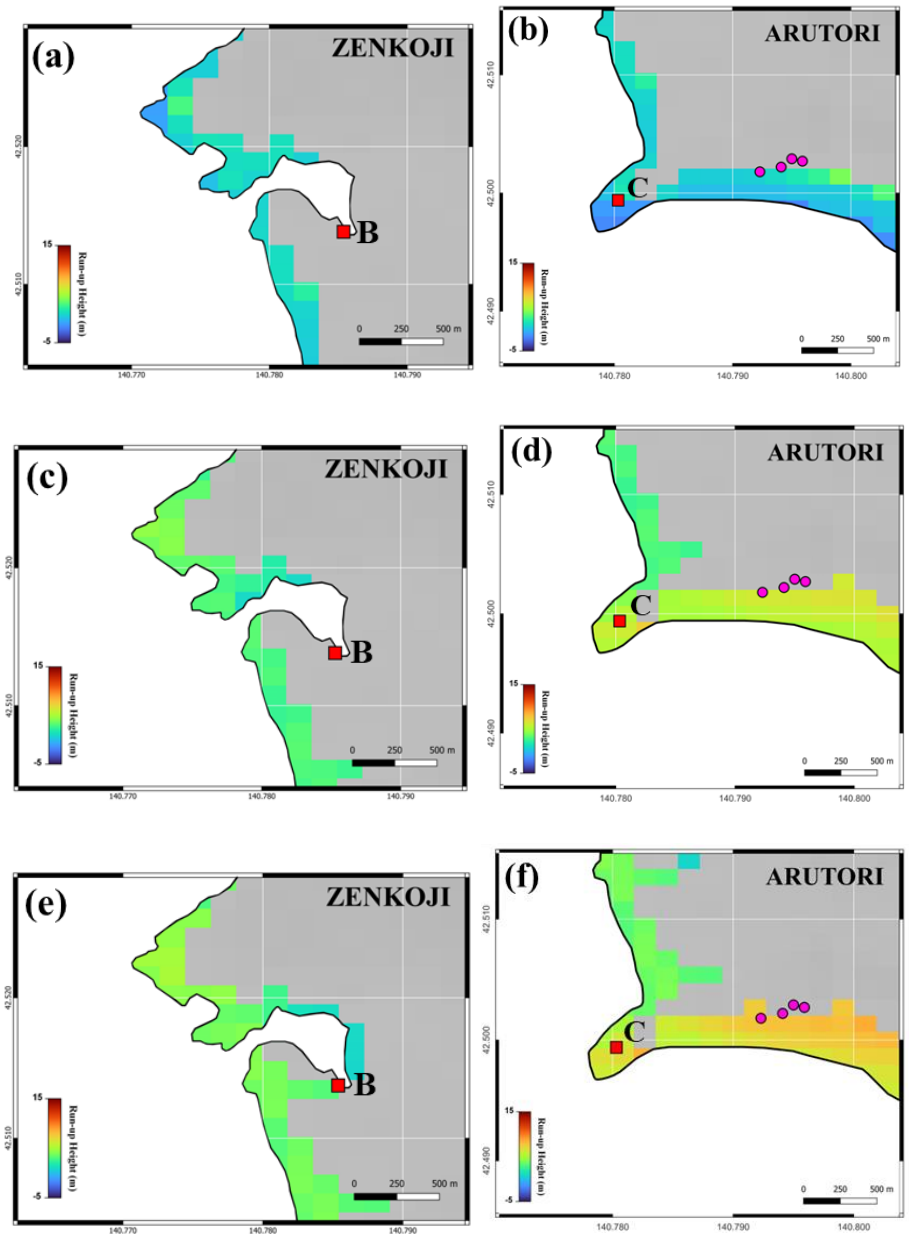

Figure 5.10 Inundation simulation at Zenkoji (left) and Arutori (right) using different collapse volumes of 1.2 km^3 (a-b), 1.8 km^3 (c-d), and 2.4 km^3 (e-f).

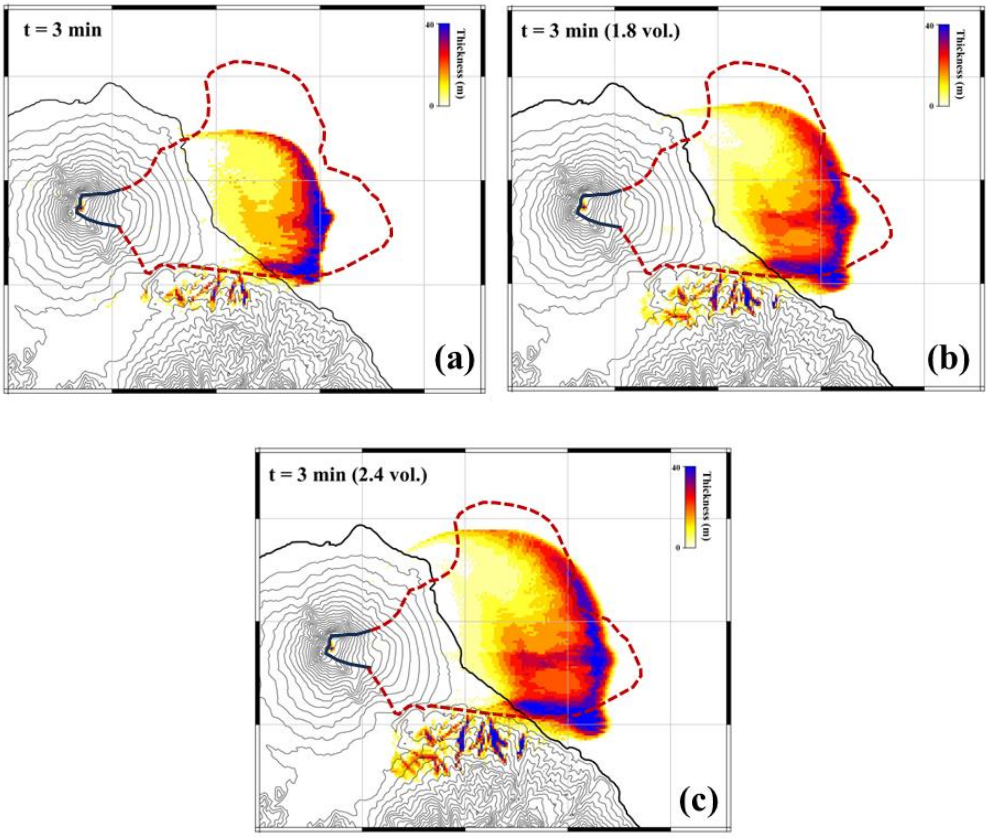

Figure 5.11 Collapse thickness deposit of 1.2 km^3 (a), 1.8 km^3 (b), and 2.4 km^3 (c) collapse volumes from 3 minutes landslide simulation. Red-dashed line indicates the depositional area from the study of Yoshimoto et al. (2003).

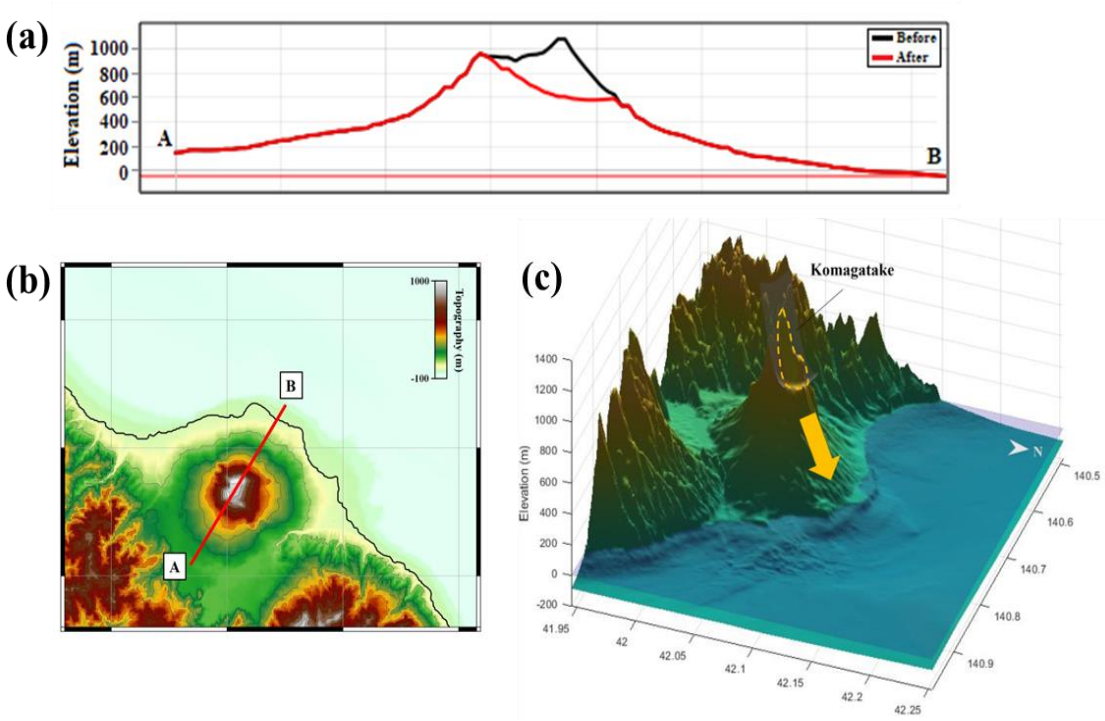

Figure 5.12 Collapse plane of the hypothetical collapse scenario 1 with total collapse volume of 0.87 km^3. **(a)** Elevation profile from the cross-section A-B indicated in (b). **(c)** Main collapse plane at the northeast of Komagatake volcano.

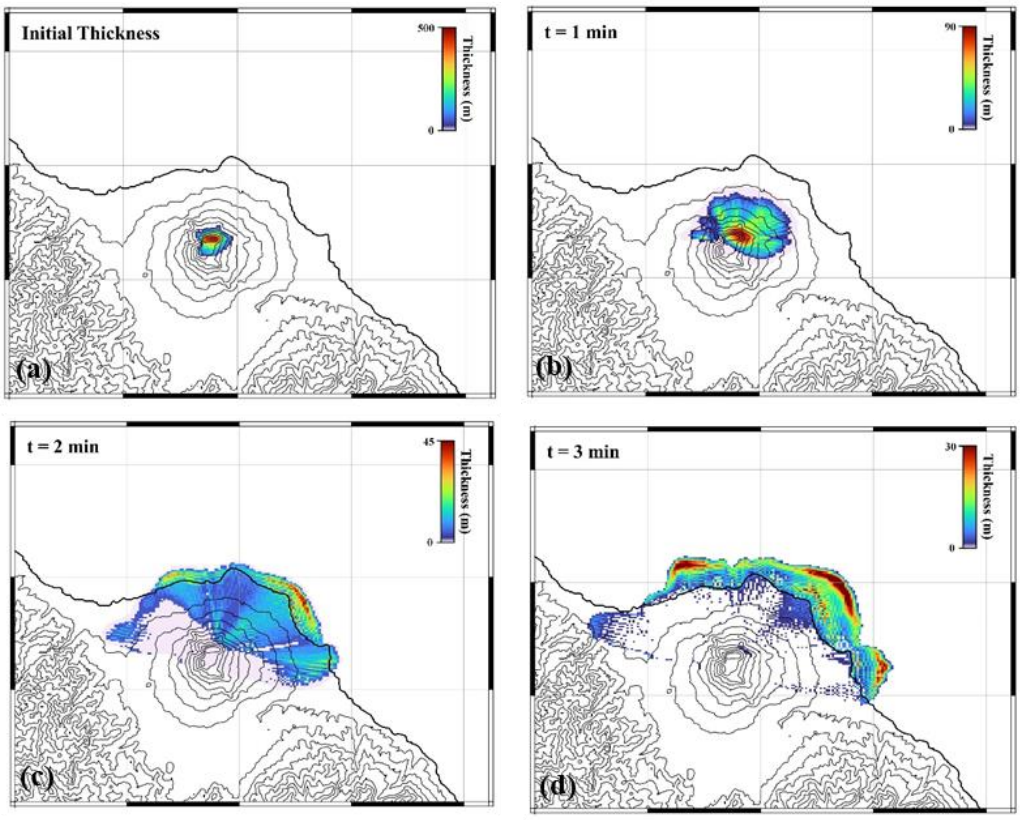

Figure 5.13 Landslide thickness for 3-min simulation from hypothetical collapse scenario 1 with total collapse volume of 0.87 km^3.

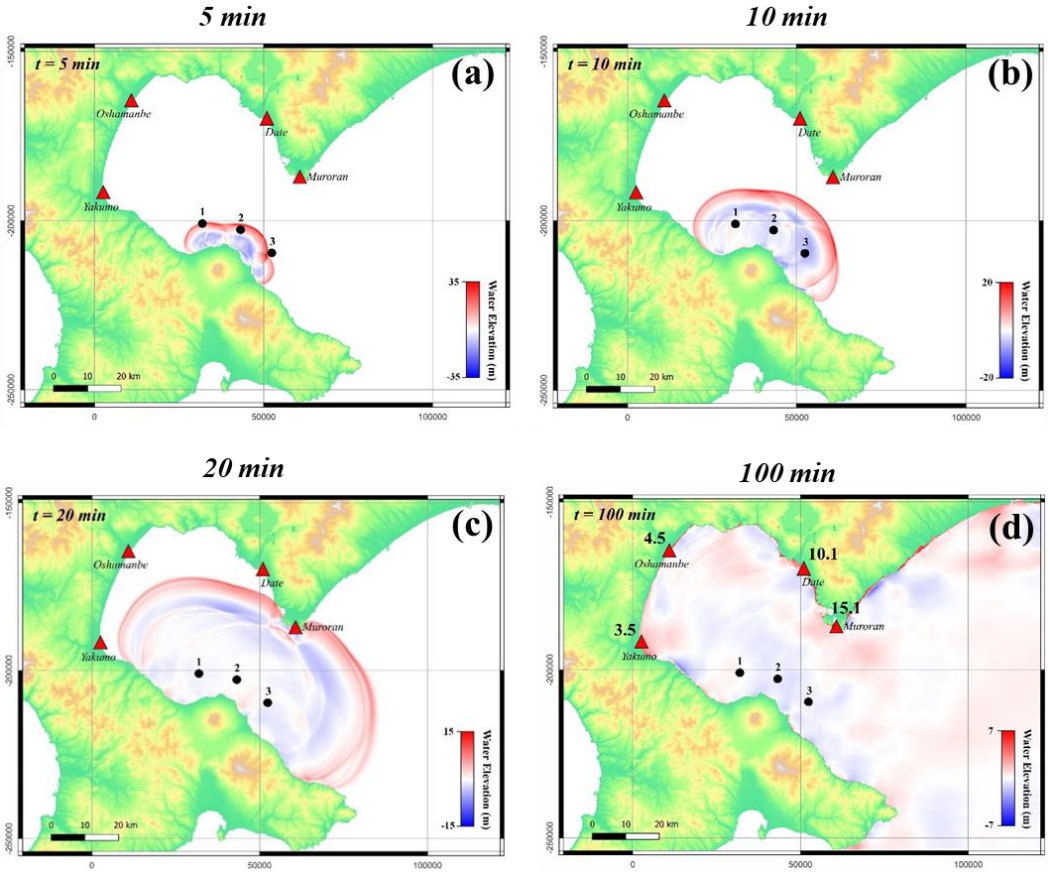

Figure 5.14 Snapshots of tsunami propagation simulation from hypothetical collapse scenario 1 at 5 min (a), 10 min (b), 20 min (c), and 100 min (d). The black circle indicates the three virtual observation points. The red triangles and label in the fig (d) indicate the maximum tsunami height at those locations.

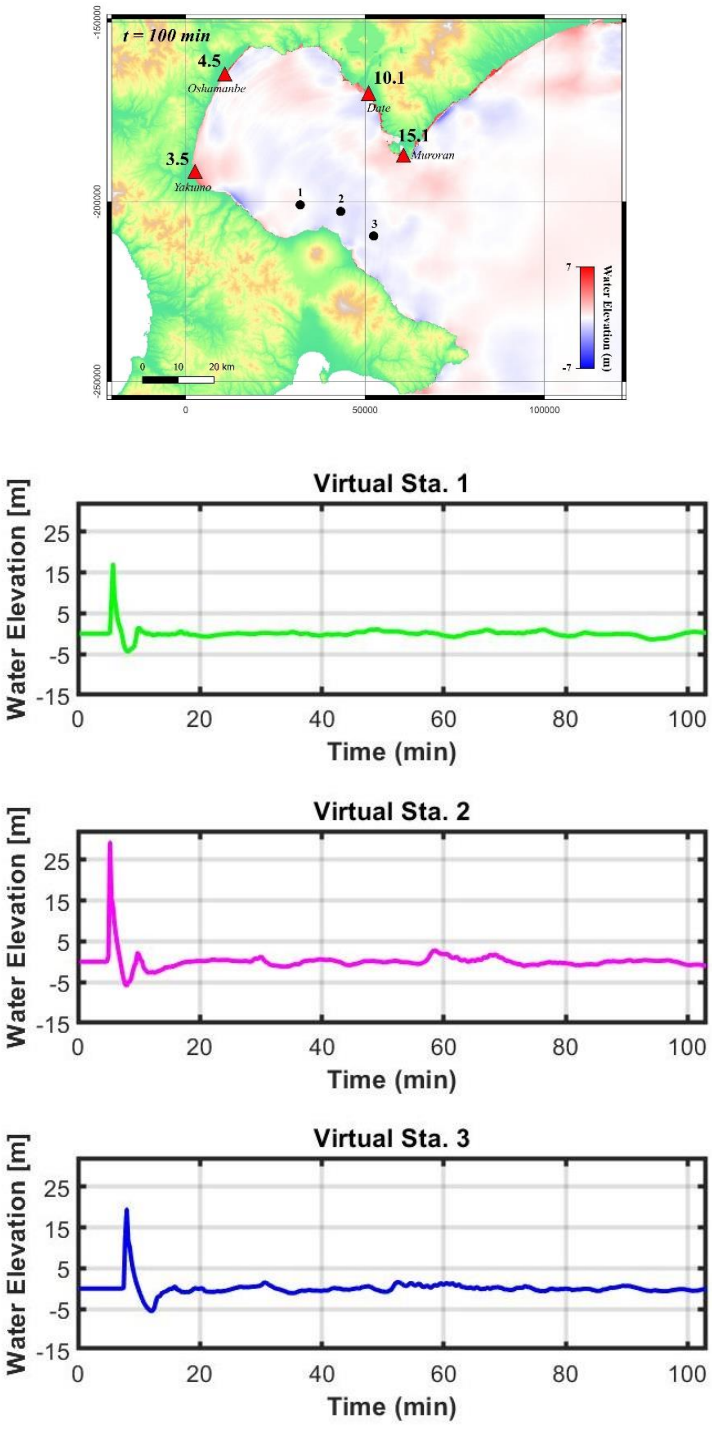

Figure 5.15 Extracted tsunami waveforms at three virtual observation stations resulting from the hypothetical collapse scenario 1.

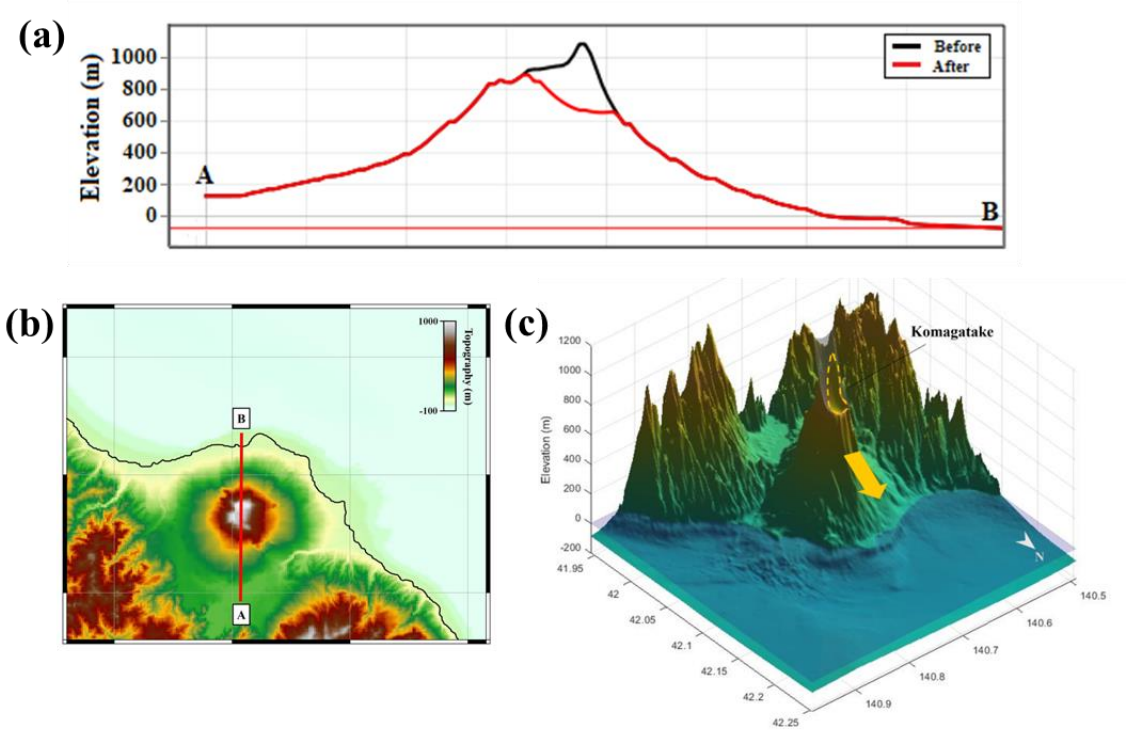

Figure 5.16 Collapse plane of the hypothetical collapse scenario 2 with total collapse volume of 0.63 km^3. **(a)** Elevation profile from the cross-section A-B indicated in (b). **(c)** Main collapse plane at the north part of Komagatake volcano.

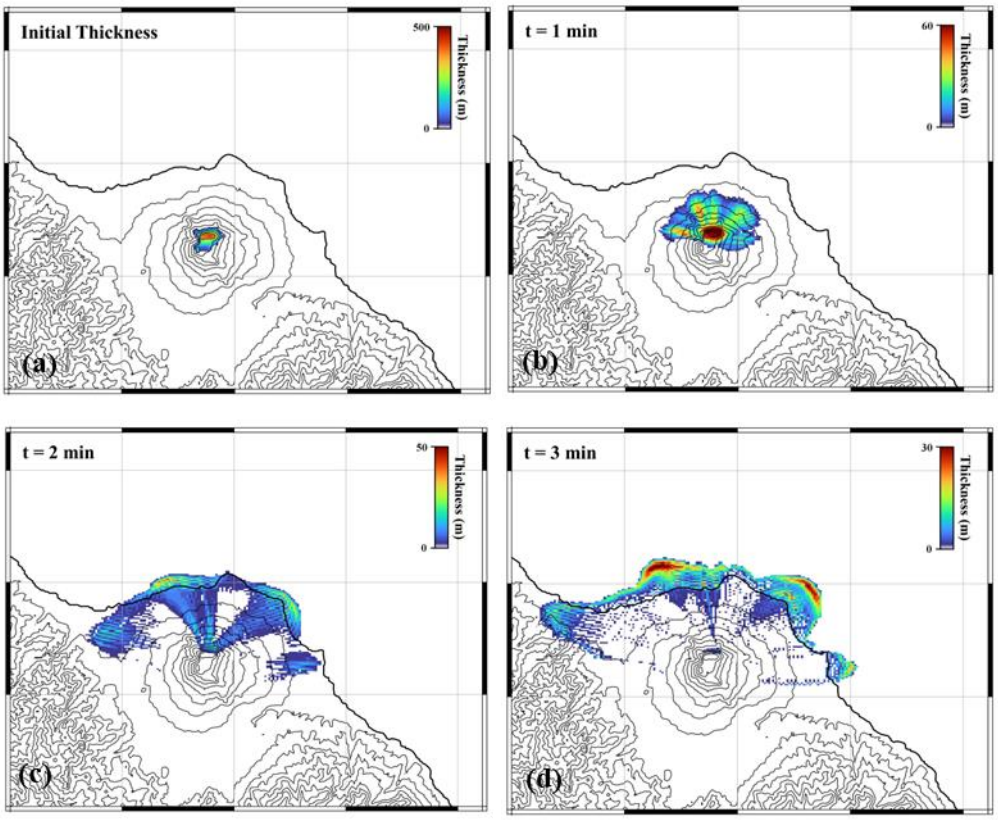

Figure 5.17 Landslide thickness for 3-min simulation from hypothetical collapse scenario 2 with total collapse volume of 0.63 km^3.

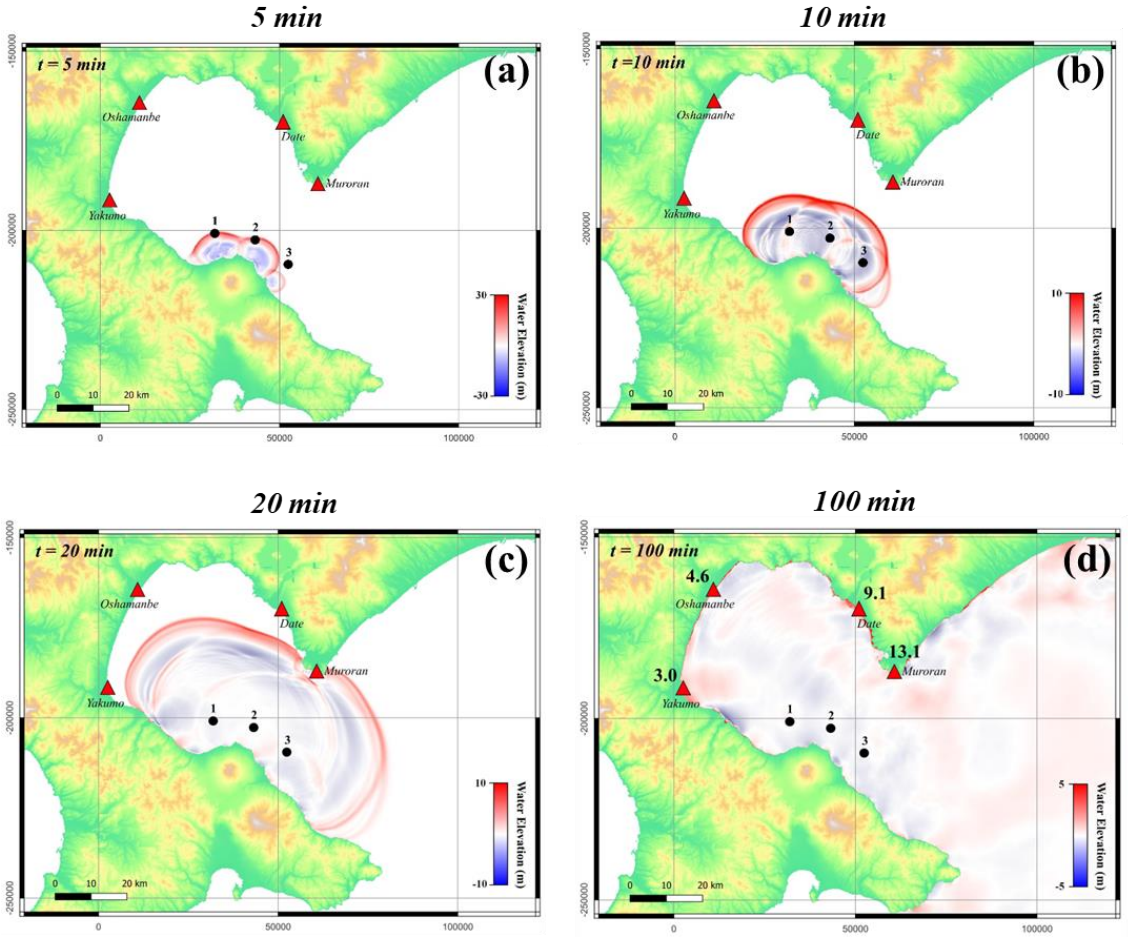

Figure 5.18 Snapshots of tsunami propagation simulation from hypothetical collapse scenario 2 at 5 min (a), 10 min (b), 20 min (c), and 100 min (d). The black circle indicates the three virtual observation points. The red triangles and label in the fig (d) indicate the maximum tsunami height at those locations.

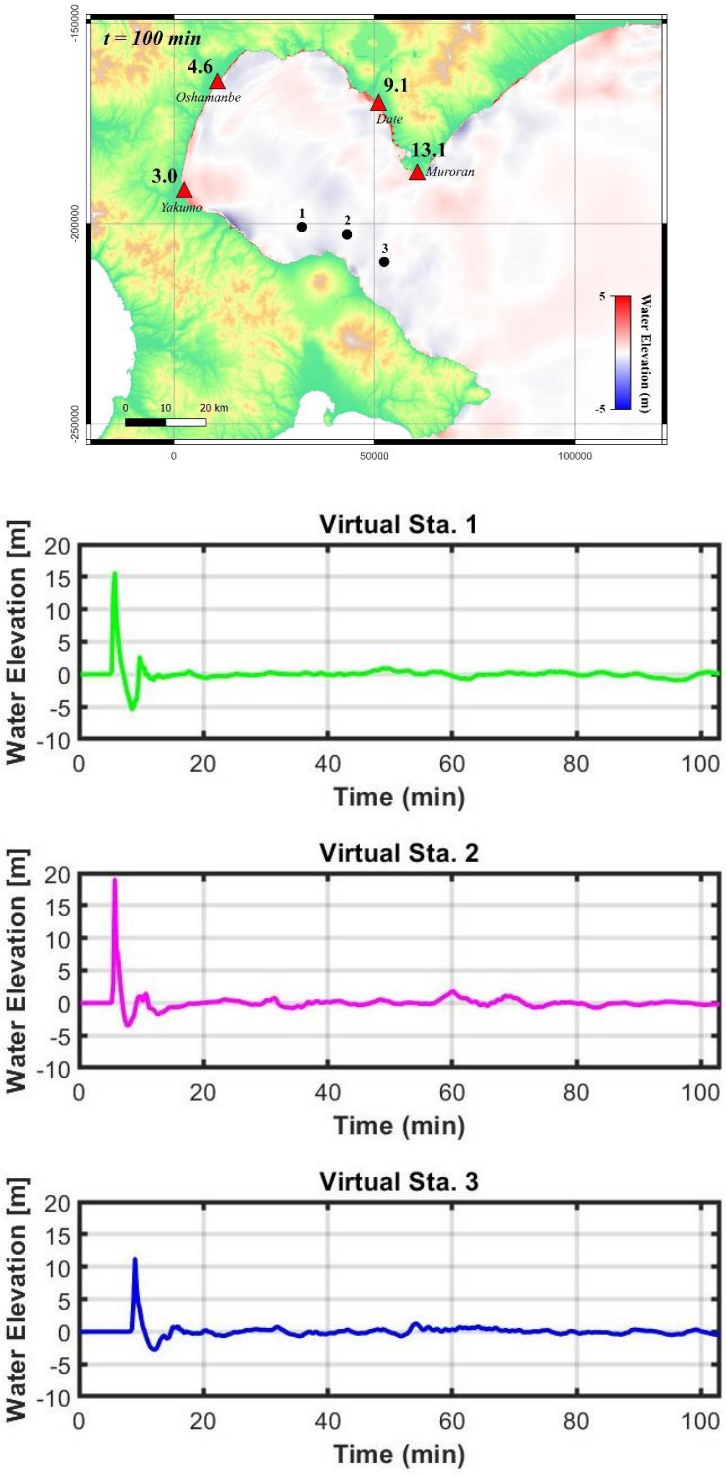

Figure 5.19 Extracted tsunami waveforms at three virtual observation stations resulting from the hypothetical collapse scenario 2.

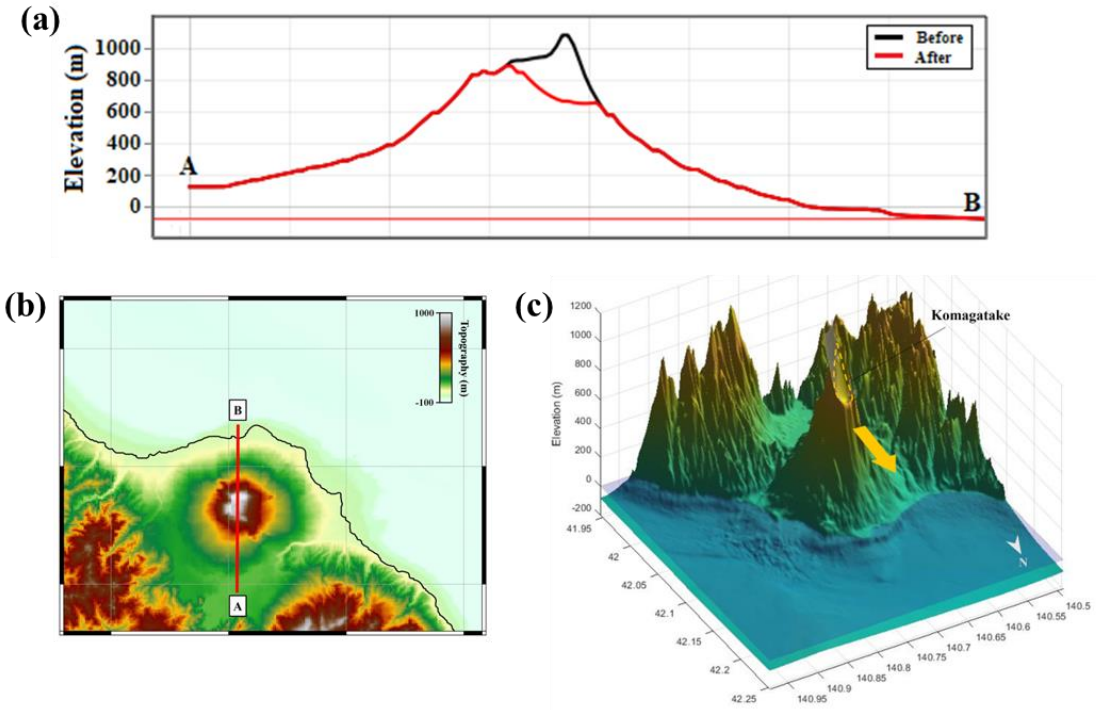

Figure 5.20 Collapse plane of the hypothetical collapse scenario 3 with total collapse volume of 0.72 km^3. **(a)** Elevation profile from the cross-section A-B indicated in (b). **(c)** Main collapse plane at the northwest part of Komagatake volcano.

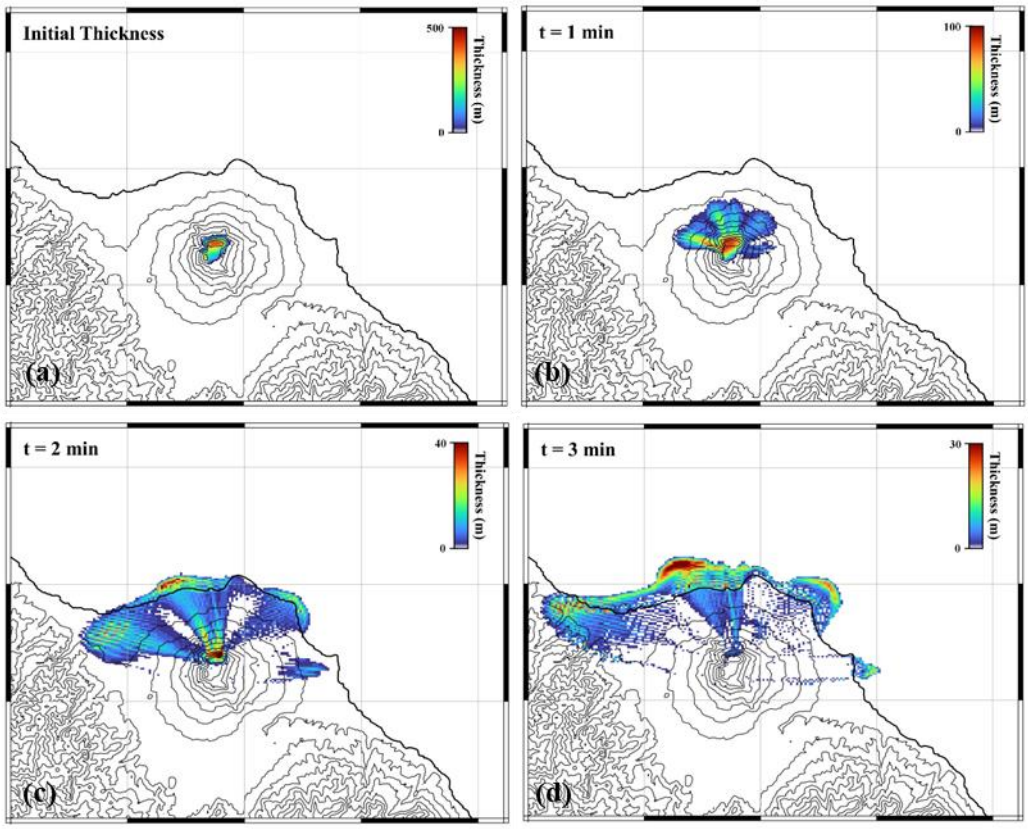

Figure 5.21 Landslide thickness for 3-min simulation from hypothetical collapse scenario 3 with total collapse volume of 0.73 km^3.

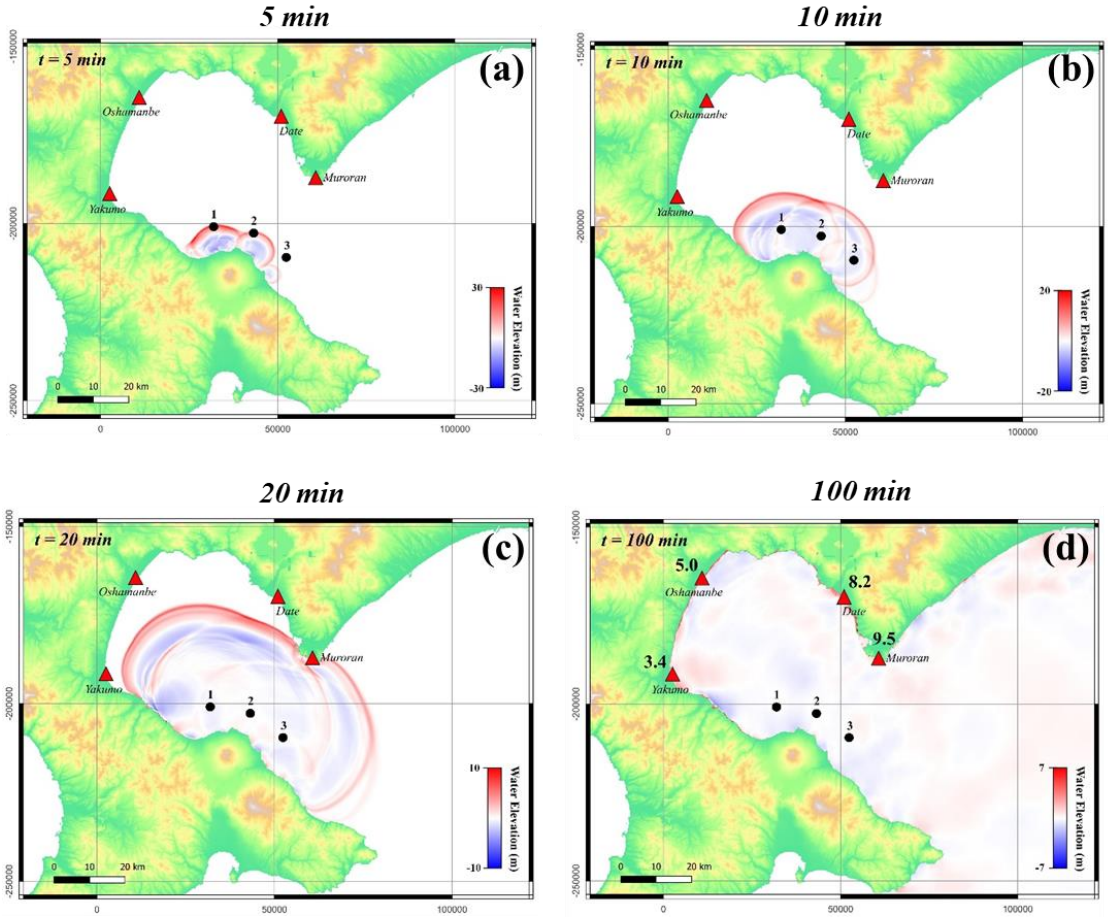

Figure 5.22 Snapshots of tsunami propagation simulation from hypothetical collapse scenario 3 at 5 min (a), 10 min (b), 20 min (c), and 100 min (d). The black circle indicates the three virtual observation points. The red triangles and label in the fig (d) indicate the maximum tsunami height at those locations.

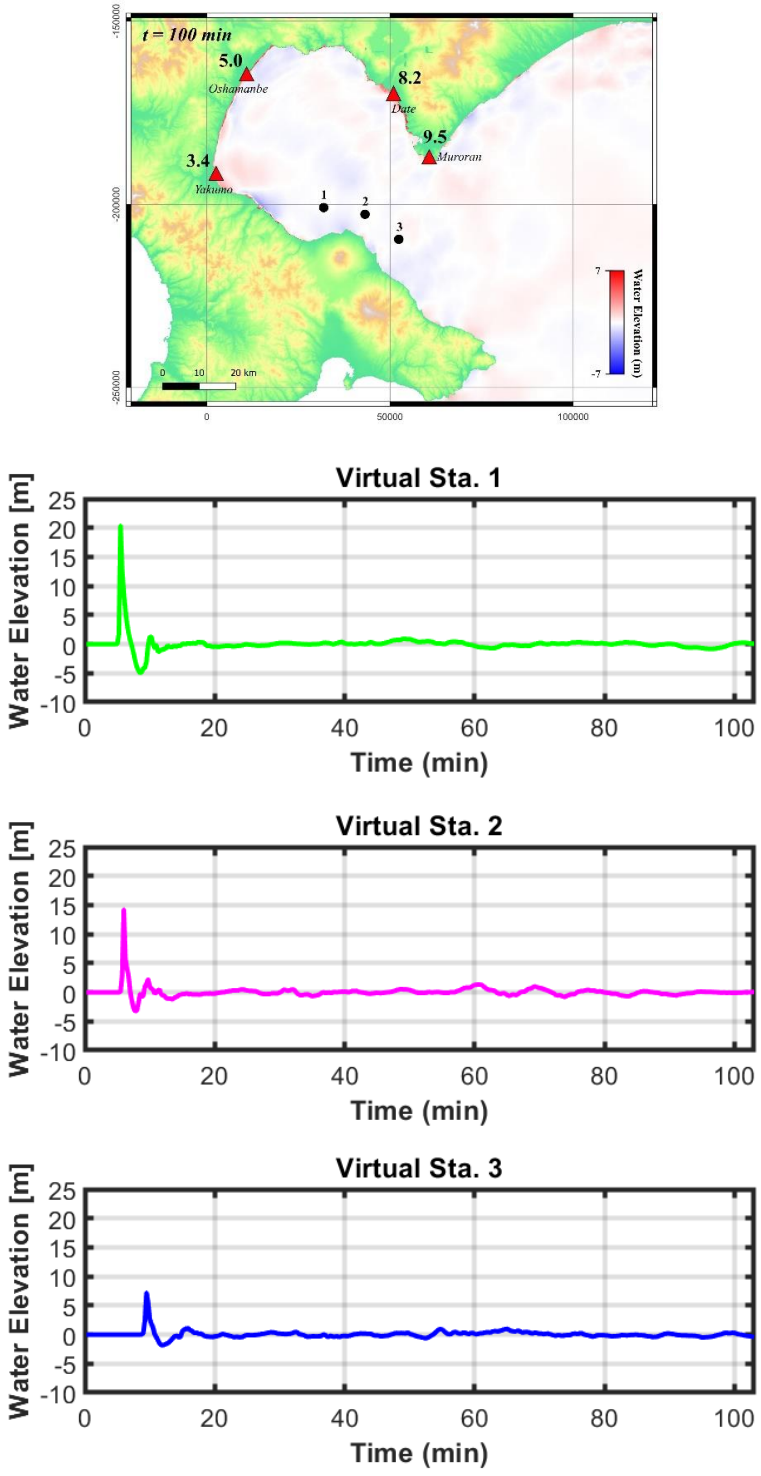

Figure 5.23 Extracted tsunami waveforms at three virtual observation stations resulting from the hypothetical collapse scenario 3.

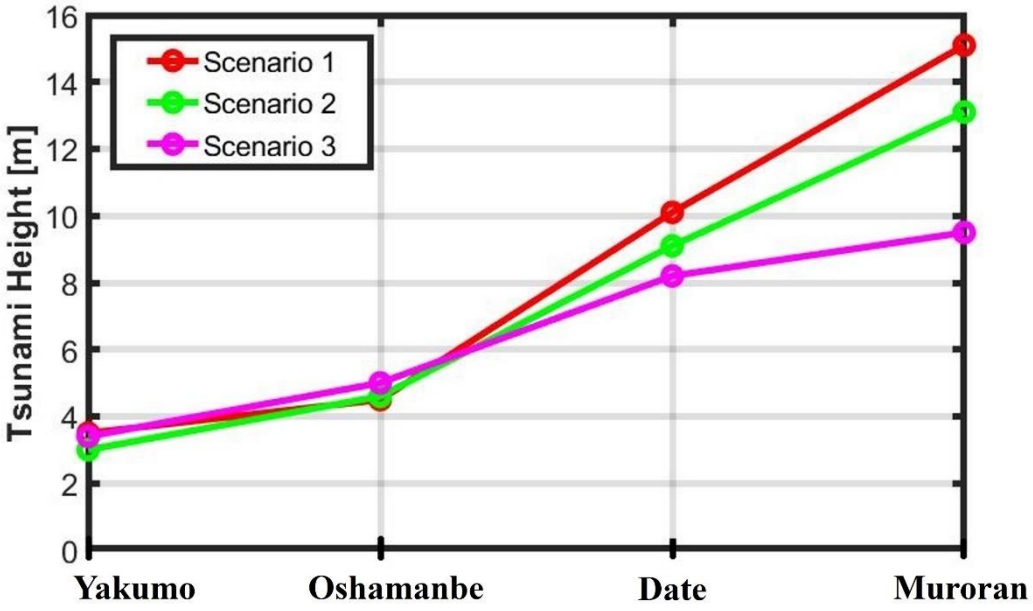

Figure 5.24 Comparison of tsunami height at four locations (Yakumo, Oshamanbe, Date, Muroran) from three different hypothetical scenario 1, 2, and 3.

General Conclusion and Future Directions

Study towards the development of tsunami warning system associated with volcanic sector collapse was conducted through numerical simulation of landslide and tsunami from Anak Krakatau and Komagatake volcano. In the case of Anak Krakatau, a real-time forecasting method was proposed for volcanic sector collapse tsunami of Anak Krakatau in Indonesia. The tsunami generation and propagation models in this study were carefully tested by performing a numerical simulation of the 2018 Anak Krakatau tsunami and were validated with observed waveforms at four tide gauge stations. For future disaster mitigation strategies, we propose a real-time tsunami forecasting method based on the pre-computed database for the Anak Krakatau volcanic tsunamis in Indonesia. Numerical experiments for the three test cases showed that our method could efficiently produce appropriate tsunami forecasts in the vicinity of the Sunda Strait. Moreover, by implementing our method, it allows us to estimate real-time tsunamis generated by volcanic activity of Anak Krakatau without considering the information on source mechanisms.

Further study relating to the development of tsunami warning was conducted by simulating the sector collapse and tsunami of Komagatake volcano located in Hokkaido, Japan. Preliminary modeling of the 1640 Komagatake tsunami was performed and validated with the available tsunami measurement data including tsunami deposits and tsunami height. The findings of this study suggested that an initial collapse volume of 1.8-2.4 km^3 is appropriate for simulating the 1640 Komagatake tsunami event. Further study on the tsunami characteristics indicated that the essential information on tsunami generation can be identified from the recorded waveforms at observation stations. Given

those results, tsunami warning can be done by utilizing available information obtained from observation stations. Moreover, rapid tsunami detection at observation stations allows us to have warning time for targeted coastal areas. Various technique with utilization of observation stations have been available for tsunami forecasting including pre-computed database, tsunami data assimilation, etc. Tsunami warning with pre-computed database concept should be work for sector collapse of Komagatake. This method can provide rapid tsunami forecasting along the coast by finding the best scenario based on the obtained information from observation stations. Using another method of tsunami data assimilation can be another options for sector collapse case of Komagatake. However, applying data assimilation method requires more numbers of observation stations in the vicinity of Komagatake. Finding the most suitable forecasting technique for sector collapse case of Komagatake should be prioritized for further improvement of the study of Komagatake.

Performing study for two different volcanic sector collapse cases, both study on the volcanic sector collapse of Anak Krakatau and Komagatake volcano shows that the existence of observation station in the vicinity of volcano is essential towards the implementation of tsunami early warning. Considering the findings, a well-constructed tsunami forecasting method based on the utilization of observation stations should be feasible for future tsunami warning systems even for volcanic tsunami cases.

Acknowledgement

I would like to express my deepest gratitude to my academic supervisor, Prof. Yuichiro Tanioka, for his guidance, discussion, and continuous support during the study. I will not be able to finish this study without his support. I would also like to thank Dr. Yusuke Yamanaka for many valuable discussions and suggestions throughout the study. I sincerely send my gratitude to all ISV Seismological Seminar members for the advice, encouragement, and insightful comments for this study. Also, I would like to thank all teachers in the Institute of Seismology and Volcanology for their support during my study. I thank all my colleagues in the Institute of Seismology and Volcanology, I received so much kindness and help from ISV members. I would also send my gratitude to my beloved parents and family for their caring, prayers, and infinite support through thick and thin. Lastly, I would like to thank Ministry of Education, Culture, Sports, Science, and Technology (MEXT) of Japan and DX Doctoral Fellowship of Hokkaido University, for the financial support during the study.

References

Aoi, S., Asano, Y., Kunugi, T., Kimura, T., Uehira, K., Takahashi, N., Ueda, H., Shiomi, K., Matsumoto, T., & Fujiwara, H. (2020). MOWLAS: NIED observation network for earthquake, tsunami and volcano. *Earth, Planets and Space, 72*(1). https://doi.org/10.1186/s40623-020-01250-x.

Bernard, E., & Titov, V. (2015). Evolution of tsunami warning systems and products. *Philosophical Transactions of the Royal Society A: Mathematical, Physical and Engineering Sciences*, *373*(2053). https://doi.org/10.1098/rsta.2014.0371.

Camus, G., Gourgaud, A., & Vincent, P. M. (1987). Petrologic evolution of Krakatau (Indonesia): Implications for a future activity. *Journal of Volcanology and Geothermal Research*, 33(4), 299–316. https://doi.org/10.1016/0377-0273(87)90020-5.

Calabrò, L., Harris, A. J. L., & Thouret, J. C. (2020). Media views of the Stromboli 2002-2003 eruption and evacuation: A content analysis to understand framing of risk communication during a volcanic crisis. *Journal of Applied Volcanology*, *9*(1), 1–23. https://doi.org/10.1186/s13617-020-00094-0.

Day, S. J. (2015). Volcanic Tsunamis. In *The Encyclopedia of Volcanoes* (Second Edition). Elsevier Inc. https://doi.org/10.1016/B978-0-12-385938-9.00058-4.

Deplus, C., Bonvalot, S., Dahrin, D., Diament, M., Harjono, H., & Dubois, J. (1995). Inner structure of the Krakatau volcanic complex (Indonesia) from gravity and bathymetry data. *Journal of Volcanology and Geothermal Research*, *64*(1–2), 23–52. https://doi.org/10.1016/0377-0273(94)00038-I.

Di Risio, M., De Girolamo, P., Bellotti, G., Panizzo, A., Aristodemo, F., Molfetta, M. G., & Petrillo, A. F. (2009). Landslide-generated tsunamis runup at the coast of a conical island: New physical model experiments. *Journal of Geophysical Research: Oceans*, *114*(1). https://doi.org/10.1029/2008JC004858.

Fritz, H. M., Hager, W. H., & Minor, H. E. (2003). Landslide generated impulse waves. 2. Hydrodynamic impact craters. *Experiments in Fluids*, *35*(6), 520–532. https://doi.org/10.1007/s00348-003-0660-7.

Fritz, H.M., Hager, W.H., Minor, H.E., (2004). Near field characteristics of landslide generated impulse waves. J. Waterw. Port, Coast. Ocean Eng. 130, 287–302.

Fritz, H. M., Borrero, J. C., Synolakis, C. E., & Yoo, J. (2006). 2004 Indian Ocean tsunami flow velocity measurements from survivor videos. *Geophysical Research Letters*, *33*(24), 3–7. https://doi.org/10.1029/2006GL026784.

Furukawa, R., Nanayama, F., & Yoshimoto, M. (2008). Volcanic debris-avalanche as a cause of a historic tsunami: The AD 1640 eruption of the Hokkaido-Komagatake volcano, Northern Japan. *Solutions to Coastal Disasters Congress 2008: Tsunamis - Proceedings of the Solutions to Coastal Disasters Congress 2008: Tsunamis*, *313*(December 2014), 235–247. https://doi.org/10.1061/40978(313)22.

Gallotti, G., Passaro, S., Armigliato, A., Zaniboni, F., Pagnoni, G., Wang, L., Sacchi, M., Tinti, S., Ligi, M., & Ventura, G. (2020). Potential mass movements on the Palinuro volcanic chain (southern Tyrrhenian Sea, Italy) and consequent tsunami generation. *Journal of Volcanology and Geothermal Research*, *404*, 107025. https://doi.org/10.1016/j.jvolgeores.2020.107025.

Giachetti, T., Paris, R., Kelfoun, K., & Pérez-Torrado, F. J. (2011). Numerical modelling of the tsunami triggered by the Gumar debris avalanche, Tenerife (Canary Islands): Comparison with field-based data. *Marine Geology*, *284*(1–4), 189–202. https://doi.org/10.1016/j.margeo.2011.03.018.

Giachetti, T., Paris, R., Kelfoun, K., & Ontowirjo, B. (2012). Tsunami hazard related to a flank collapse of Anak Krakatau Volcano, Sunda Strait, Indonesia. *Geological Society Special Publication*, *361*(1), 79–90. https://doi.org/10.1144/SP361.7.

Glimsdal, S., Pedersen, G. K., Harbitz, C. B., & Løvholt, F. (2013). Dispersion of tsunamis: Does it really matter? *Natural Hazards and Earth System Sciences, 13*, 1507–1526. https://doi.org/10.5194/nhess-13-1507-2013.

Grilli, S. T., Shelby, M., Kimmoun, O., Dupont, G., Nicolsky, D., Ma, G., et al. (2017). Modeling coastal tsunami hazard from submarine mass failures: Effect of slide rheology, experimental validation, and case studies off the US East Coast. *Natural Hazards*, 86(1), 353–391. https://doi.org/10.1007/s11069-016-2692-3.

Grilli, S. T., Tappin, D. R., Carey, S., Watt, S. F. L., Ward, S. N., Grilli, A. R., Engwell, S. L., Zhang, C., Kirby, J. T., Schambach, L., & Muin, M. (2019). Modelling of the tsunami from the December 22, 2018, lateral collapse of Anak Krakatau volcano in the Sunda Straits, Indonesia. *Scientific Reports*, *9*(1), 1–15. https://doi.org/10.1038/s41598-019-48327-6.

Gusman, A. R., & Tanioka, Y. (2014). W Phase Inversion and Tsunami Inundation Modeling for Tsunami Early Warning: Case Study for the 2011 Tohoku Event. *Pure and Applied Geophysics*, *171*(7), 1409–1422. https://doi.org/10.1007/s00024-013-0680-z.

Gusman, A. R. Tanioka, Y. MacInnes, B.T. and Tsushima, H. (2014). A methodology for near-field tsunami inundation forecasting: Application to the 2011 Tohoku tsunami. *AGU: Journal of Geophysical Research, Solid Earth, 120,* 1195–1209. https://doi.org/10.1002/2014JB011376.

Hanka, W., Saul, J., Weber, B., Becker, J., & Harjadi, P. (2010). Real-time earthquake monitoring for tsunami warning in the Indian Ocean and beyond. *Natural Hazards and Earth System Science*, *10*(12), 2611–2622. https://doi.org/10.5194/nhess-10-2611-2010.

Harbitz, C. B., Løvholt, F., Pedersen, G., & Masson, D. G. (2006). Mechanisms of tsunami generation by submarine landslides: A short review. *Norsk Geologisk Tidsskrift*, *86*(3), 255–264.

Heidarzadeh, M., Putra, P. S., Nugroho, S. H., & Rashid, D. B. Z. (2020). Field survey of tsunami heights and runups following the 22 December 2018 Anak Krakatau Volcano tsunami, Indonesia. *Pure and Applied Geophysics*, *177*(10), 4577–4595. https://doi.org/10.1007/s00024-020-02587-w.

Heidarzadeh, M., Ishibe, T., Sandanbata, O., Muhari, A., & Wijanarto, A. B. (2020). Numerical modeling of the subaerial landslide source of the 22 December 2018 Anak Krakatoa volcanic tsunami, Indonesia. *Ocean Engineering*, *195*(September 2019), 106733. https://doi.org/10.1016/j.oceaneng.2019.106733.

Heinrich, P., Piatanesi, A., (2000). Near-field modeling of the July 17, 1998 tsunami in Papua New Guinea. Geophys. Res. Lett. 27 (19), 3037–3040.

Heinrich, P., Boudon, G., Komorowski, J. C., Sparks, R. S. J., Herd, R., & Voight, B. (2001b). Numerical simulation of the December 1997 Debris Avalanche in Montserrat, Lesser Antilles. Geophysical Research Letters, 28(13), 2529–2532.

Hochfeld, I., Hort, M., Schwalbe, E., & Dürig, T. (2022). Eruption dynamics of Anak Krakatau volcano (Indonesia) estimated using photogrammetric methods. *Bulletin of Volcanology*, *84*(8), 1–18. https://doi.org/10.1007/s00445-022-01579-z.

Hossen, M. J., Mulia, I. E., Mencin, D., & Sheehan, A. F. (2021). Data Assimilation for Tsunami Forecast With Ship-Borne GNSS Data in the Cascadia Subduction Zone. *Earth and Space Science*, *8*(3), 1–12. https://doi.org/10.1029/2020EA001390.

Hunt, J. E., Tappin, D. R., Watt, S. F. L., Susilohadi, S., Novellino, A., Ebmeier, S. K., Cassidy, M., Engwell, S. L., Grilli, S. T., Hanif, M., Priyanto, W. S., Clare, M. A., Abdurrachman, M., & Udrekh, U. (2021). Submarine landslide megablocks show half of Anak Krakatau island failed on December 22nd, 2018. *Nature Communications*, *12*(1). https://doi.org/10.1038/s41467-021-22610-5.

Husrin, S., Annunziato, A., Prasetya, G S., Hidayat, R. 2022. IDSL for Tsunami Early Warning System in Indonesia. *IOP Conf. Ser.: Earth Environ. Sci*. 1117 012028. https://doi.org/10.1088/1755-1315/1117/1/012028.

Japan Meteorological Agency. (2012). Report on the 2011 off the Pacific coast of Tohoku earthquake, Chapter 2: Tsunami, Technical Report of the Japan Meteorological Agency 133, https://www.jma.go.jp/jma/kishou/books/gizyutu/133/CHAPTER2.pdf (in Japanese with an English abstract).

Jimenez, C., Carbonel, C., & Rojas, J. (2018). Numerical Procedure to Forecast the Tsunami Parameters from a Database of Pre-Simulated Seismic Unit Sources. *Pure and Applied Geophysics*, *175*(4), 1473–1483. https://doi.org/10.1007/s00024-017-1660-5.

Kanoglu U., Synolakis C.E. 2015 Tsunami dynamics, forecasting, and mitigation. Chapter 2 hazards and disasters series: Coastal and marine hazards, risks, and disasters, Elsevier, pp. 15-57, 10.1016/B978-0-12-396483-0.00002-9.

Katsui, Y. and Yamamoto, M., 1981. The 1741--1742 activity of Oshima-Oshima volcano, north Japan. J. Fac. Sci., Hokkaido Univ., Ser. 4, 19:527-536.

Kawamata K, Takaoka K, Ban K, Imamura F, Yamaki S, Kobayashi E (2005) Model of tsunami gen- eration by collapse of volcanic eruption: the 1741 Oshima–Oshima tsunami. In: Satake K (ed) Tsunamis: case studies and recent developments. Springer, New York, pp 79–96. https ://doi. org/10.1007/1-4020-3331-1_5.

Keating, B. H., & McGuire, W. J. (2000). Island edifice failures and associated tsunami hazards. *Pure and Applied Geophysics*, *157*(6–8), 899–955. https://doi.org/10.1007/s000240050011.

Kelfoun, K., & Druitt, T. H. (2005). Numerical modeling of the emplacement of Socompa rock avalanche, Chile. *Journal of Geophysical Research: Solid Earth*, *110*(12), 1–13. https://doi.org/10.1029/2005JB003758.

Kelfoun, K., Giachetti, T., & Labazuy, P. (2010). Landslide-generated tsunamis at Réunion Island. *Journal of Geophysical Research: Earth Surface*, *115*(4). https://doi.org/10.1029/2009JF001381.

Kirby, J.T., Shi, F., Nicolsky, D., Misra, S., (2016). The 27 April 1975 Kitimat, British Columbia, submarine landslide tsunami: a comparison ofmodelling approaches. Landslides 13, 1421–1434. https://doi.org/10.1007/s10346-016-0682-x.

LeVeque RJ, George DL, Berger MJ (2011) Tsunami modelling with adaptively refined finite volume meth- ods. Acta Numer 20:211–289. https://doi.org/10.1017/S0962492911000043.

Løvholt, F., G. Pedersen, and G. Gisler (2008), Oceanic propagation of a potential tsunami from the La Palma Island J. Geophys. Res., 113, C09026, doi:10.1029/2007JC004603.

Løvholt, F., Pedersen, G., Harbitz, C. B., Glimsdal, S., & Kim, J. (2015). On the characteristics of landslide tsunamis. Philosophical Transactions ofthe Royal Society a: Mathematical, Physical and Engineering Sciences, 373(2053), 20140376. https://doi.org/ 10.1098/rsta.2014.0376.

Løvholt, F., Glimsdal, S., & Harbitz, C. B. (2020). On the landslide tsunami uncertainty and hazard. *Landslides*, *17*(10), 2301–2315. https://doi.org/10.1007/s10346-020-01429-z.

Ma, G., Shi, F., & Kirby, J. T. (2012). Shock-capturing non-hydrostatic model for fully dispersive surface wave processes. *Ocean Modelling*, *43–44*, 22–35. https://doi.org/10.1016/j.ocemod.2011.12.002.

Ma G, Kirby JT, Hsu T-J, Shi F (2015) A two layer granular landslide model for tsunami wave generation: theory and computation. Ocean Model 93:40–55. https ://doi.org/10.1016/j.ocemo d.2015.07.012.

Maeda, T., Obara, K., Shinohara, M., Kanazawa, T., & Uehira, K. (2015). Successive estimation of a tsunami wavefield without earthquake source data: A data assimilation approach toward real-time tsunami forecasting. *Geophysical Research Letters*, *42*(19), 7923–7932. https://doi.org/10.1002/2015GL065588.

Makinoshima, F., Oishi, Y., Yamazaki, T., Furumura, T., & Imamura, F. (2021). Early forecasting of tsunami inundation from tsunami and geodetic observation data with convolutional neural networks. *Nature Communications*, *12*(1), 1–10. https://doi.org/10.1038/s41467-021-22348-0.

McGuire, W.J., 1996. Volcano Instability: A Review of Contemporary Themes. vol. 110. Geological Society, London, Special Publications, pp. 1–23 1 January 1996. https:// doi.org/10.1144/GSL.SP.1996.110.01.01.

Mochizuki, M., Kanazawa, T., Uehira, K., Shimbo, T., Shiomi, K., Kunugi, T., et al. (2016). S-net project: Construction of large scale seafloor observatory network for tsunamis and earthquakes in Japan, AGU Fall Meeting, NH43B-1840. http://adsabs.harvard.edu/abs/ 2016AGUFMNH43B1840M.

Mori N, Satake K, Cox D, Goda K, Catalan P.A, Ho TC, Imamura F, Tomiczek T, Lynett P, Miyashita T, Muhari A, Titov V and Wilson R . (2022). Giant tsunami monitoring, early warning and hazard assessment. Nat Rev Earth Environ 3, 557–572. https://doi.org/10.1038/s43017-022-00327-3.

Mori N and Takahashi T. (2012). The 2011 Tohoku earthquake tsunami joint survey group, 2012, Nationwide post event survey and analysis of the 2011 Tohoku earthquake tsunami. Coastal Eng J 54(1):1250001. https://doi.org/10.1142/S05 78563412500015.

Muhari, A., Heidarzadeh, M., Susmoro, H., Nugroho, H. D., Kriswati, E., Supartoyo, Wijanarto, A. B., Imamura, F., & Arikawa, T. (2019). The December 2018 Anak Krakatau Volcano Tsunami as Inferred from Post-Tsunami Field Surveys and Spectral Analysis. *Pure and Applied Geophysics*, *176*(12), 5219-5233. https://doi.org/10.1007/s00024-019-02358-2.

Mulia, I. E., Gusman, A. R., & Satake, K. (2017). Optimal Design for Placements of Tsunami Observing Systems to Accurately Characterize the Inducing Earthquake. *Geophysical Research Letters*, *44*(24), 12,106-12,115. https://doi.org/10. 1002/2017GL075791.

Mulia, I. E., Watada, S., Ho, T. C., Satake, K., Wang, Y., & Aditiya, A. (2020). Simulation of the 2018 Tsunami due to the flank failure of Anak Krakatau Volcano and implication for future observing systems. *Geophysical Research Letters*, *47*(14). https://doi.org/10.1029/2020GL087334.

Mulia, I. E., Ueda, N., Miyoshi, T., Gusman, A. R., & Satake, K. (2022). Machine learning-based tsunami inundation prediction derived from offshore observations. *Nature Communications*, *13*(1), 5489. https://doi.org/10.1038/s41467-022-33253-5.

Nakanishi, R., & Okamura, S. (2019). Tsunami deposits from the 1640 Hokkaido Komagatake eruption, north Japan: constraints on inundation heights and numerical simulation of volcanic debris avalanche-derived tsunami. *The Journal of the Geological Society of Japan*, *125*(12), 835–851. https://doi.org/10.5575/geosoc.2019.0032

Nishimura, Y. and Miyaji, N. (1998). On height distribution of tsunami caused by the 1640 eruption of Hokkaido-Komagatake, Northern Japan. Bull. Volcano. Soc. Japan, 43, 239–242.

Nishimura, Y., Miyaji, N., & Suzuki, M. (1999). Behavior of historic tsunamis of volcanic origin as revealed by onshore tsunami deposits. *Physics and Chemistry of the Earth, Part A: Solid Earth and Geodesy*, *24*(11–12), 985–988. https://doi.org/10.1016/S1464-1895(99)00146-5.

Nomanbhoy, N., & Satake, K. (1995). Generation mechanism of tsunamis from the 1883 Krakatau eruption. Geophysical Research Letters, 22(4), 509–512. https://doi.org/10.1029/ 94GL03219.

Paris, R., Giachetti, T., Chevalier, J., Guillou, H., & Frank, N. (2011). Tsunami deposits in Santiago Island (Cape Verde archipelago) as possible evidence of a massive flank failure of Fogos volcano. *Sedimentary Geology*, *239*(3–4), 129–145. https://doi.org/10.1016/j.sedgeo.2011.06.006.

Paris, R. (2015). Source mechanisms of volcanic tsunamis. *Philosophical Transactions of the Royal Society A: Mathematical, Physical and Engineering Sciences*, *373*(2053), 1–15. https://doi.org/10.1098/rsta.2014.0380.

Paris, A., Okal, E. A., Guérin, C., Heinrich, P., Schindelé, F., & Hébert, H. (2019). Numerical modeling of the June 17, 2017, landslide and tsunami events in Karrat Fjord, West Greenland. *Pure and Applied Geophysics*, *176*(7), 3035–3057. https://doi.org/10.1007/s00024-019-02123-5.

Paris, A., Heinrich, P., Paris, R., & Abadie, S. (2020). The December 22, 2018, Anak Krakatau, Indonesia, landslide and tsunami: Preliminary modeling results. *Pure and Applied Geophysics*, *177*(2), 571–590. https://doi.org/10.1007/s00024-019-02394-y.

Paris, A., Heinrich, P., & Abadie, S. (2021). Landslide tsunamis: Comparison between depth-averaged and Navier–Stokes models. *Coastal Engineering*, *170* (September), 104022. https://doi.org/10.1016/j.coastaleng.2021.104022.

Rabinovich, A. B., Titov, V. V., Moore, C. W., & Eblé, M. C. (2017). The 2004 Sumatra Tsunami in the Southeastern Pacific Ocean: New global insight from observations and modeling. *Journal of Geophysical Research: Oceans*, 122, 7992–8019, https://doi.org/10.1002/2017JC013078.

Reid, J. A., & Mooney, W. D. (2023). Tsunami Occurrence 1900–2020: A Global Review, with Examples from Indonesia. *Pure and Applied Geophysics*, *180*(5), 1549–1571. https://doi.org/10.1007/s00024-022-03057-1.

Ren, Z., Wang, Y., Wang, P., Hou, J., Gao, Y., & Zhao, L. (2020). Numerical study of the triggering mechanism of the 2018 Anak Krakatau tsunami: eruption or collapsed landslide? *Natural Hazards*, *102*(1), 1–13. https://doi.org/10.1007/s11069-020-03907-y.

Robbe-Saule, M., Morize, C., Bertho, Y., Sauret, A., Hildenbrand, A., & Gondret, P. (2021). From laboratory experiments to geophysical tsunamis generated by

subaerial landslides. *Scientific Reports*, *11*(1), 1–9. https://doi.org/10.1038/s41598-021-96369-6.

Salmanidou, D. M., Guillas, S., Georgiopoulou, A., & Dias, F. (2017). Statistical emulation of landslide-induced tsunamis at the Rockall Bank, NE Atlantic. *Proceedings of the Royal Society A: Mathematical, Physical and Engineering Sciences*, *473*(2200). https://doi.org/10.1098/rspa.2017.0026.

Savage, S. B., & Hutter, K. (1989). The motion of a finite mass of granular material down a rough incline. *Journal of Fluid Mechanics*, *199*(2697), 177–215. https://doi.org/10.1017/S0022112089000340.

Shi, F., Kirby, J. T., Harris, J. C., Geiman, J. D. & Grilli, S. T. (2012). A high-order adaptive time-stepping TVD solver for Boussinesq modeling of breaking waves and coastal inundation. *Ocean Modelling*, 43-44, 36–51, https://doi.org/10.1016/j.ocemod.2011.12.004.

Siebert, L. (1984). Large volcanic debris avalanches: Characteristics of source areas, deposits, and associated eruptions. *Journal of Volcanology and Geothermal Research*, *22*(3–4), 163–197. https://doi.org/10.1016/0377-0273(84)90002-7

Simkin, T., & R. S. Fiske (1983), Krakatau 1883 Eruption and its Effects, 464 pp., Smithson. Inst., Washington, D. C.

Sudrajat, A. (1982). The morphological development of Anak Krakatau volcano, Sunda Strait. *Geology of Indonesia*, 9,1–11.

Stehn, C. E. The geology and volcanism of the Krakatau group. In Guidebook for the 4th Pacific Science Congress, pp. 1–55 (University of Michigan, Ann Arbor, MI, USA, 1929).

Takahashi, N., Imai, K., Ishibashi, M., Sueki, K., Obayashi, R., Tanabe, T., Tamazawa, F., Baba, T., & Kaneda, Y. (2017). Real-time tsunami prediction system using

DONET. *Journal of Disaster Research*, *12*(4), 766–774. https://doi.org/10.20965/jdr.2017.p0766.

Tanioka, Y., Gusman, A. R., Ioki, K., & Nakamura, Y. (2014). Real-time tsunami inundation forecast for a recurrence of 17th century great Hokkaido earthquake in Japan. *Journal of Disaster Research*, *9*(3), 358–364. https://doi.org/10.20965/jdr.2014.p0358.

Tanioka, Y. (2020). Improvement of near-field tsunami forecasting method using ocean-bottom pressure sensor network (S-net). *Earth, Planets and Space*, *72*, 132. https://doi.org/10.1186/s40623-020-01268-1.

Tanioka, Y., Yamanaka, Y., & Nakagaki, T. (2022). Characteristics of the deep sea tsunami excited offshore Japan due to the air wave from the 2022 Tonga eruption. *Earth, Planets and Space*, *74*(1). https://doi.org/10.1186/s40623-022-01614-5.

Tappin, D. R., Grilli, S. T., Harris, J. C., Geller, R. J., Masterlark, T., Kirby, J. T., Shi, F., Ma, G., Thingbaijam, K. K. S., & Mai, P. M. (2014). Did a submarine landslide contribute to the 2011 Tohoku tsunami? *Marine Geology*, *357*, 344–361. https://doi.org/10.1016/j.margeo.2014.09.043.

Tsuruoka, A., H. Suzuki, M. Marutani, and A. Nakadate. (2015). Tide and Tsunami Observation System in JMA, Sokkou-jihou, 82, S105-S123, https://www.jma.go.jp/jma /kishou/books/sokkou-kaiyou/82/vol82s105.pdf (in Japanese).

Tsushima, H., Hirata, K., Hayashi, Y., Tanioka, Y., Kimura, K., Sakai, S., Shinohara, M., Kanazawa, T., Hino, R., & Maeda, K. (2011). Near-field tsunami forecasting using offshore tsunami data from the 2011 off the Pacific coast of Tohoku Earthquake. *Earth, Planets and Space*, *63*(7), 821–826. https://doi.org/10.5047/eps.2011.06.052.

Tsushima, H., Hino, R., Tanioka, Y., Imamura, F., & Fujimoto, H. (2012). Tsunami waveform inversion incorporating permanent seafloor deformation and its

application to tsunami forecasting. *Journal of Geophysical Research: Solid Earth*, *117*(3), 1–20. https://doi.org/10.1029/2011JB008877.

Tsushima, H., & Ohta, Y. (2014). Review on near-field tsunami forecasting from offshore tsunami data and onshore GNSS data for tsunami early warning. *Journal of Disaster Research*, *9*(3), 339–357. https://doi.org/10.20965/jdr.2014.p0339.

Hiroaki Tsushima, Ryota Hino, Yusaku Ohta, Takeshi Iinuma, and S. M. (2014). tFISH/RAPiD: Rapid improvement of near-field tsunami forecasting based on offshore tsunami data by incorporating onshore GNSS data. *Geophysical Research Letters*, *April*, 6298–6305. https://doi.org/10.1002/2014GL059863.

Ulvrova, M., Paris, R., Nomikou, P., Kelfoun, K., Leibrandt, S., Tappin, D. R., & McCoy, F. W. (2016). Source of the tsunami generated by the 1650 AD eruption of Kolumbo submarine volcano (Aegean Sea, Greece). *Journal of Volcanology and Geothermal Research*, *321*, 125–139. https://doi.org/10.1016/j.jvolgeores.2016.04.034.

UNESCO/IOC. 2024. Monitoring and Warning for Tsunamis Generated by Volcanoes. UNESCO, IOC Technical Series No. 183. https://oceanexpert.org/document/32765.

Voight, B. (1981). The 1980 eruptions of Mount St. Helens, Washington. Time scale for the first moments of the May 18 eruption. US Geological Survey Professional Paper, 1250, 69–86.

Walter, T. R., Haghshenas Haghighi, M., Schneider, F. M., Coppola, D., Motagh, M., Saul, J., Babeyko, A., Dahm, T., Troll, V. R., Tilmann, F., Heimann, S., Valade, S., Triyono, R., Khomarudin, R., Kartadinata, N., Laiolo, M., Massimetti, F., & Gaebler, P. (2019). Complex hazard cascade culminating in the Anak Krakatau sector collapse. *Nature Communications*, *10*(1). https://doi.org/10.1038/s41467-019-12284-5.

Wang, Y., Imai, K., Mulia, I. E., Ariyoshi, K., Takahashi, N., Sasaki, K., Kaneko, H., Abe, H., & Sato, Y. (2023). Data Assimilation Using High-Frequency Radar for Tsunami Early Warning: A Case Study of the 2022 Tonga Volcanic Tsunami. Journal of Geophysical Research: Solid Earth, 128(2), 1–12. https://doi.org/10.1029/2022JB025153.

Ward, S. N., & Day, S. (2001). Cumbre Vieja volcano-potential collapse and tsunami at La Palma, Canary Islands. *Geophysical Research Letters*, *28*(17), 3397–3400. https://doi.org/10.1029/2001GL013110.

Ward, S. N., & Day, S. (2003). Lateral collapse and the tsunami of 1888. Geophysical Journal International, 154, 891–902.

Watts, P. and Borrero, J. (2009). Probability distributions of landslide volumes. *Nonlinear Processes in Geophysics*, *16*(2), 179–188. https://doi.org/10.5194/npg-16-179-2009.

Williams, R., Rowley, P., & Garthwaite, M. C. (2019). Reconstructing the Anak Krakatau flank collapse that caused the December 2018 Indonesian tsunami. *Geology*, *47*(10), 973–976. https://doi.org/10.1130/G46517.1.

Xiao, L., Ward, S. N., & Wang, J. (2015). Tsunami Squares Approach to Landslide-Generated Waves: Application to Gongjiafang Landslide, Three Gorges Reservoir, China. *Pure and Applied Geophysics*, *172*(12), 3639–3654. https://doi.org/10.1007/s00024-015-1045-6

Yamamoto, N., Aoi, S., Hirata, K., Suzuki, W., Kunugi, T., & Nakamura, H. (2016). Multi-index method using offshore ocean-bottom pressure data for real-time tsunami forecast 4. Seismology. *Earth, Planets and Space*, *68*(1). https://doi.org/10.1186/s40623-016-0500-7.

Yamanaka, Y., & Tanioka, Y. (2017). Estimating the topography before volcanic sector collapses using tsunami survey data and numerical simulations. *Pure and Applied Geophysics*, *174*(8), 3275–3291. https://doi.org/10.1007/s00024-017-1589-8.

Ye, L., Kanamori, H., Rivera, L., Lay, T., Zhou, Y., Sianipar, D., & Satake, K. (2020). The 22 December 2018 tsunami from flank collapse of Anak Krakatau volcano during eruption. *Science Advances*, *6*(3), 1–10. https://doi.org/10.1126/sciadv.aaz1377.

Yoshimoto, M., Furukawa, R., Nanayama, F., Nishimura, Y., Nishina, K., Uchida, Y., Takarada, S., Takahashi, R., & Kinoshita, H. (2003). Subaqueous distribution and volume estimation of the debris-avalanche deposit from the 1640 eruption of Hokkaido-Komagatake volcano, southwest Hokkaido, Japan. *The Journal of the Geological Society of Japan*, *109*(10), 595–606. https://doi.org/10.5575/geosoc.109.595 (in Japanese with an English abstract).

Zengaffinen, T., Løvholt, F., Pedersen, G. K., & Muhari, A. (2020). Modelling 2018 Anak Krakatoa flank collapse and tsunami: Effect of landslide failure mechanism and dynamics on tsunami generation. *Pure and Applied Geophysics*, *177*(6), 2493–2516. https://doi.org/10.1007/s00024-020-02489-x.